Study of $Z' \to e^(+)e^(-)$ in full simulation with regard to discrimination between models beyond the standard model, ATLAS@CERN

Martina Schäfer

LPSC 04.59

Diploma Thesis

Study of $Z' \to e^+e^-$ in full simulation with regard to discrimination between models beyond the Standard Model, ATLAS @ CERN

Studien des Kanals $Z' \to e^+e^-$ mit vollständiger Simulation zur Unterscheidung verschiedener Modelle jenseits des Standard-Modells

Examiner: PROF.DR.TH.MÜLLER
Co-Examiner: DR.FABIENNE LEDROIT-GUILLON

LPSC GRENOBLE

Faculty of Physics of the
UNIVERSITY OF KARLSRUHE

September 2004

Versicherung

Ich versichere, diese Arbeit selbständing unter Angabe aller wesentlicher Hilfsmittel und Referenzen angefertigt zu haben.

Martina Schäfer

Abstract

Although experimental results so far agree with predictions of the Standard Model, it is widely felt to be incomplete. Many prospective theories beyond the Standard Model predict extra neutral gauge bosons, denoted by Z', which might be light enough to be accessible at the LHC.
Observables sensitive to properties of these extra gauge bosons might be used to discriminate between the different theories beyond the Standard Model.
In the present work several of these observables (total decay width, leptonic cross-section and forward-backward asymmetries) are studied at generation level and with a full simulation in the ATLAS detector. The $Z' \to e^+e^-$ decay channel was chosen and two values for the mass of the Z': 1.5 TeV and 4 TeV.
Background is studied as well and it is confirmed that a Z' boson could easily be discovered at the chosen masses.
It is shown that even in full simulation the studied observables can be determined with a good precision. In a next step a discrimination strategy has to be developed given the presented methods to extract the variables and their precision.

Acknowledgments ♣ *Merci* ♣ Dankeschön

Mes remerciements vont tout d'abord à **Fabienne Ledroit**, *qui a encadré mon travail. Elle a été une guide précieuse. Je la remercie aussi pour sa grande disponibilité, la liberté et la confiance qu'elle m'a accordée et pour sa gentillese et compréhension. C'était un plaisir de travailler avec elle.*
Je suis également reconnaissante à tout le groupe ATLAS *au* LPSC *pour l'accueil dans leur group, des discussions et conseils qui m'ont été profitables, notamment* **Faïrouz Ohlsson-Malek** *et* **Arnaud Lucotte**.
Je remercie aussi tous les membres du laboratoire que j'ai croisés pendant mon travail, notamment **Michael Klasen** *de la groupe théorique,* **Sabine Crépé** *de* DØ *et bien sûr le service informatique.*

I would specially thank **Georges Azuelos** and **Samir Ferrag** the coordinators of the ATLAS exotics group for helpful discussions and critical suggestions. I appreciated their disponibility, guidance and the efficient and fast e-mail contact. Thanks also go to **Giacomo Polesello**, the ATLAS physics coordinator.

I thank **Anne-Sylvie Nicollerat** for helpful discussions and explanations concerning her publication at the beginning of my work.
Je remercie également **Olivier Gaumer** *thésard à Annecy au* LAPP *pour sa disponibilité en début de mon travail.*
Je suis reconnaissante à **Marc Besançon** *du* GDR-SUSY *pour ses conseils lors de mes premiers pas dans les extra-dimensions.*

I also owe much gratitude to **Armin Nairz** and **Nectarios Benekos** from CERN for their help and support for the full simulation, without their help it would never have been possible to make available all the data in this short time.

Thanks also go to **Stathes Paganis** from CERN for his help on the calibration. Quickly and always accessible he handled me his work on calibration to apply it on my studies.

Insbesondere möchte ich mich auch ganz herzlich bei **Prof. Müller** aus Karlsruhe bedanken, der meine Diplomarbeit betreute und auch Mitglied der *jury* meiner *DEIR soutenance* in Grenoble war. Ich bedanke mich ganz besonders für sein Entgegenkommen alles Anstehende auch trotz der großen geographischen Entfernung möglichst einfach zu regeln. Natürlich auch ein Dankeschön an Herrn **Engelhardt**, Ansprechpartner des deutsch-französischen Austauschprogrammes. Ohne seinen persönlichen Einsatz wäre mein Aufenthalt in Grenoble nie möglich gewesen.

This diploma thesis was performed in the ATLAS group at the LPSC (*Laboratoire de physique subatomique et de cosmologie*) in Grenoble (France).
The LPSC is a mixed laboratory (CNRS/IN2P3-UJF-INPG) of fundamental research in subatomic physics splited in 3 big experimental and theoretical axes: nuclear and hadronic matter, particle physics and astroparticles.
The ATLAS group has been a member of the ATLAS collaboration since November 1991. The major activities have been concentrated on participating in the elaboration and in the construction of the liquid argon calorimeter of ATLAS until 2003.
From 1991 to 2003, the group has been committed to:

- ⋆ the construction of the barrel electromagnetic presampler
- ⋆ the production and the test of the filtering preamplifiers of the electromagnetic calorimeter
- ⋆ the design of digital optical links
- ⋆ the radiation test of electronic and mechanical components

The group is presently committed to:

- ⋆ the design and the delivery of part of the liquid argon cryogenics
- ⋆ the development of the final software of the liquid argon calorimeter
- ⋆ CP violation and rare B decay modes, connected with performances studies of the electromagnetic calorimeter
- ⋆ study and analysis of new phenomena and exotics physics
- ⋆ Data-Challenges National coordination and participation
- ⋆ European Data Grid National coordination and participation

Contents

List of Figures

List of Tables

1. Deutsche Zusammenfassung (German summary)

Studien des Kanals $Z' \to e^+e^-$ mit vollständiger Simulation zur Unterscheidung verschiedener Modelle jenseits des Standard-Modells

1.1. Einleitung

Auch wenn die aktuellen Resultate der Teilchenphysik gut mit den Vorhersagen des Standard-Modells übereinstimmen, geht man heute davon aus, dass das Standard-Modell nur die Niederenergie-Näherung eines umfassenderen Modelles ist. So wird z.B. die Gravitation vom Standard-Modell nicht beschrieben, schwache und starke Wechselwirkung lassen sich nicht ohne weitere Annahmen vereinen, die Massen der Quarks und Leptonen gehen als freie Parameter in das Modell mit ein,...
Viele Theorien jenseits des Standard-Modells sehen zusätzliche neutrale Eichbosonen vor, die mit Z' bezeichnet werden. Sie könnten leicht genug sein, um an aktuellen oder zukünftigen Beschleunigern entdeckt zu werden. Die Entdeckung eines solchen Teilchens wäre ein direkter Test des Standard-Modells und unseres Verständnisses der Physik auf viel höheren Energieskalen als heute bekannt sind.
Die Suche nach diesen Z' Teilchen ist ein wichtiger Aspekt des heutigen Programmes der experimentellen Hochenergie- und Beschleunigerphysik. Aktuelle Resultate zeigen, dass die Z' Bosonen eine hohe Masse besitzen. Ein Z' Boson könnte am TEVATRON im Run II entdeckt werden, wenn es leichter als 1 TeV ist. Detaillierte experimentelle und theoretische Studien zeigen, dass das Entdeckungspotential des LHC's bis zu einer Masse von mindestens 5 TeV reicht. Nach einer möglichen Entdeckung eines solchen Bosons müßten seine Kopplungskonstanten untersucht werden, um den korrekten theoretischen Rahmen zu definieren.

In der vorliegenden Arbeit werden die Resultate einer direkten Suche nach einem Z' Boson im Di-Elektronenkanal vorgestellt: Ziel ist es, Methoden und Werkzeuge zu entwickeln, um Variablen, die zur Unterscheidung dienen können, zu rekonstruieren und zu analysieren. Die analysierten Daten sind in Monte Carlo Generatoren simulierte Proton-Proton Kollisionen ($pp \to Z' \to e^+e^-$), die sich bei einer Schwerpunktsenergie von 14 TeV ereignen.
Die Zusammenfassung ist gleich strukturiert wie das Hauptdokument, damit Details schnell zu finden sind.

1.2. Z' Modelle

Es gibt eine Vielzahl von Erweiterungen des Standard-Modells, die zusätzliche Eichbosonen vorhersagen. Aus diesen Modellen werden im Rahmen dieser Arbeit die folgenden betrachtet und hier kurz zusammengefasst:

- ⋆ Das sequentielle Standard-Modell Z'_{SSM}:
  In diesem Fall unterscheidet sich das Z' Boson von einem gewöhnlichen Z Boson ausschließlich durch seine höhere Masse. Insbesondere sind die Kopplungskonstanten unverändert.

- ⋆ Rechts-Links Symmetrische Modelle Z'_{LR}:
  Zur Eichgruppe des Standard-Modells wird eine weitere $SU(2)$ Gruppe hinzugefügt. Dadurch wird eine schwache rechte geladene Wechselwirkung eingeführt. Diese Modelle zeichnen sich durch das Verhältnis von rechten zu linken Kopplungskonstanten aus. In der vorliegenden Arbeit wird dieses Verhältnis auf 1 gesetzt, dh. gleich starke rechte und linke Wechselwirkungen.

- ⋆ E_6 Modelle:
  Diese Modelle rühren von einer Symmetriebrechung der Eichgruppe E_6 her. In ihnen können zwei zusätzliche neutrale Eichbosonen auftreten. Es wird von der Annahme ausgegangen, dass nur das

leichtere der beiden am LHC produziert werden kann. Dieses ist durch die folgende Linearkombination definiert:

$$Z' = \cos\beta Z'_{\psi} - \sin\beta Z'_{\chi}.$$

Der Winkel β ist ein freier Parameter in diesen Modellen. Für die Analyse werden die populären Modelle Z'_{χ} ($\beta = -\frac{\pi}{2}$), Z'_{ψ} ($\beta = 0$) und Z'_{η} ($\beta = \arctan(-\sqrt{\frac{5}{3}}) - \frac{\pi}{2}$) ausgewählt.

⋆ Z' nach Kaluza-Klein Z'_{KK}:
Aus den vielen Modellen mit zusätzlichen Dimensionen wird eines ausgewählt. In diesem speziellen Fall wird davon ausgegangen, dass große - nur von der Gravitation zugängliche - zusätzliche Dimensionen existieren und außerdem eine weitere kleine kompakte Dimension, die auch von den Eichbosonen erreicht werden kann. Das Hauptmerkmal der Propagation der Eichbosonen in diese weitere Dimension ist das Auftreten eines "Turmes von Kaluza-Klein Anregungen" im Massenspektrum. Die erste Anregung dieser Resonanz könnte am LHC sichtbar sein.

1.3. Der LHC-Beschleuniger und der ATLAS-Detektor

In diesem Kapitel werden der LHC-Beschleuniger und der ATLAS-Detektor vorgestellt. Der LHC *(Large Hadron Collider)* gehört zur nächsten Generation von Hadronkollidern und ist derzeit am CERN, dem europäischen Labor für Teilchenphysik *(Centre Européen pour la Recherche Nucléaire)*, in Konstruktion. Er ist der Nachfolger des *Large Electron Positron Collider* (LEP) und wird in dessen 27 km langen Tunnel errichtet. Die ersten Kollisionen werden für 2007 erwartet.
Die beiden Protonstrahlen werden an vier Punkten entlang des Ringes zusammengeführt. An diesen Kreuzungspunkten werden die Experimente des LHC errichtet: ATLAS und CMS, die als Mehrzweck-Detektoren einen weiten Bereich der möglichen Physik abdecken sollen, LHCb, das speziell für die Untersuchungen im Bereich der B-Physik ausgelegt wurde, und schließlich ALICE, das neue Erkenntnisse der Physik schwerer Ionen liefern soll.
Den LHC zeichnet seine hohe Schwerpunktsenergie von 14 TeV sowie seine Luminosität von $10^{33} - 10^{34}\, cm^{-2}s^{-1}$ aus. ATLAS besteht aus mehreren konzentrischen Schichten: dem inneren Detektor, den Kalorimetern und dem Myonenspektrometer.
Das Forschungsprogramm beinhaltet sowohl Studien des Standard-Modells als auch die Suche nach Signaturen von neuer Physik (zum Beispiel die Existenz von neuen Teilchen wie einem Z' Boson). ATLAS ist konzipiert um das gesamte Potential des LHC's zu nutzen. Dabei liegt das Hauptaugenmerk auf dem Nachweis des Higgs Bosons, welches auf Grund fehlender Schwerpunktsenergie bisher noch in keinem anderen Experiment nachgewiesen werden konnte.

1.4. Eigenschaften der Produktion und des Zerfalls der Z' Bosonen an Hadronkollidern

Dieses Kapitel ist eine Präambel zur Untersuchung der Variablen, die zur Unterscheidung der Modelle dienen. Der analysierte Prozess sowie sein Kontext werden vorgestellt.

Der hauptsächliche Produktionsprozess ist der Prozess $q\bar{q} \to Z'$.
Der wichtigste Kanal zur Entdeckung und Untersuchung von zusätzlichen neutralen Eichbosonen ist der leptonische Zerfall $pp \to l^+l^-X$. Hadronische Zerfälle sind schwer von dem QCD Hintergrund zu unterscheiden, andere Zerfälle sind selten oder gar unsichtbar. Aus den leptonischen Kanälen wird der Kanal e^+e^- gewählt, da die Detektorauflösung von ATLAS für die Elektronen besser als für Myonen ist und Taus schwer zu rekonstruieren sind.
Die Ausschlußgrenzen der Entdeckung eines Z' Bosons können in 2 Kategorien geteilt werden: direkte und indirekte Grenzwerte. Dabei entsprechen die direkten Grenzwerte einer Nicht-Entdeckung der Z' Resonanz, während die indirekten Grenzwerte aus Messungen verschiedener Observablen hervorgehen, die von der Existenz eines Z' Bosons verändert werden könnten. Die aktuellen, in diesem Kapitel detaillierten Werte, liegen zwischen 400-1500 GeV - abhängig vom Modell. Diese Werte sind natürlich nochmals kleiner, wenn das Z' Boson schwach oder gar nicht an die Fermionen koppelt.

Falls am LHC ein Z' nachgewiesen werden sollte, würde man sich für dessen Parameter interessieren. Neben seiner Masse, seiner Zerfallsbreite und seinem Wirkungsquerschnitt wären besonders seine

Vorwärts-Rückwärts-Asymmetrien von grossem Interesse. Diese Variablen sind abhänging von den Kopplungskonstanten zwischen den Bosonen und den Fermionen und somit vom zu Grunde liegenden theoretischen Modell. Sie können also dazu genutzt werden um zwischen den verschiedenen Modellen jenseits des Standard-Modells, die weitere Eichbosonen vorhersagen, zu unterscheiden.

1.5. Analyse auf Generator-Niveau

In diesem Kapitel wird in einem ersten Schritt die Analyse direkt nach der Erzeugung der Ereignisse durchgeführt. Dies hat zum Ziel die Phänomenologie verstehen zu lernen und die Analysemethoden zu entwickeln und zu validieren, ohne Hadronisations- oder Detektorefffekte mit einzubeziehen.
Die Ereignisse sind mit PYTHIA im Rahmen von ATHENA erzeugt worden. ATHENA ist das Software-Paket mit dem in Zukunft alle Simulationen, die Rekonstruktion der Ereignisse und die Analyse im ATLAS-Projekt betrieben werden wird. Die Z' Bosonen werden mit einer Masse von 1.5 TeV und 4 TeV erzeugt. Der erste Wert wurde so gewählt, da er einer nach heutigem Kenntnisstand möglichen Masse eines Z' entspricht. Außerdem bietet er interessante Möglichkeiten für die erste Zeit der Inbetriebnahme des LHC und ATLAS. Als zweiter Wert wurde eine größere, aber noch erreichbare Masse gewählt. Das Z'_{KK} ist als externer, vom Benutzer definierter Prozess in PYTHIA integriert worden. Für die anderen Modelle kann der von PYTHIA vorgegebene Z' Prozess benutzt und angepasst werden.
Für alle Modelle sind 60 000 Ereignisse für beide Massenwerte erzeugt, jeweils ohne Gluon- und Photon-Abstrahlung im Anfangs- und Endzustand. Die Z' Bosonen sind immer mit dem vom Drell-Yan Prozess stammenden irreduziblen Hintergrund und der kompletten Interferenz Struktur produziert.
Eine Untersuchung des Effektes der Interferenz zeigt, dass die Interferenz den Massenpeak verformt. In allen Modellen findet man eine destruktive Interferenz im Bereich von Massen etwas niedriger als der Massenpeak.
Die Zerfallsbreite ist durch eine relativistische Breit-Wigner Funktion und mehrere Exponentialfunktionen parametrisiert, wobei die Exponentialfunktionen die Partonluminosität, die Deformation des Peaks und natürlich den Drell-Yan Hintergrund mit einbeziehen. Bei einer Masse von 1.5 TeV liegen die Zerfallsbreiten je nach Modell im Bereich von 10-50 GeV. Die Resultate des Fits an die Verteilung der rekonstruierten Masse sind zufriedenstellend: Im Vergleich zu den vorher theoretisch berechneten Werten wird die Zerfallsbreite ein klein wenig (1-6%) überschätzt. Dieser Effekt wächst mit der Masse und sinkt mit der Zerfallsbreite.
Der leptonische Wirkungsquerschnitt wird durch Abzählen der Ereignisse im Bereich des Massenpeaks bestimmt. Je nach Modell liegen die Wirkungsquerschnitte im Bereich von 20-80 fb (bei $M = 1.5$ TeV) und werden mit einer Genauigkeit von 0.1-0.5 fb bestimmt. Eine gute Übereinstimmung mit den Vorhersagen von PYTHIA wird erzielt.
Die Vorwärts-Rückwärts-Asymmetrien haben unterschiedliches Verhalten der Z'-Zerfälle in Vorwärts- und Rückwärtsrichtung als Ursache. Sie werden mit verschiedenen Methoden (Abzählen, ein- und zweidimensionaler fit, mit und ohne Schnitte, ...) untersucht, um mit der Schwierigkeit zurecht zu kommen, in einer pp Kollision die Begriffe *vorwärts* und *rückwärts* korrekt zu bestimmen. Die Asymmetrien werden in Abhängigkeit der rekonstruierten invarianten Masse und der Rapidität des Leptonenpaares untersucht. Die Resultate wurden erfolgreich mit anderen Publikationen verglichen. Sie variieren nur wenig mit der Masse des Z'-Bosons.

1.6. Abschätzung des Untergrundes

Als Untergrund zum Z'-Signal werden alle Ereignisse mit einer e^+e^- Signatur betrachtet. Des Weiteren werden Ereignisse mit der Signatur $e^{\pm}\gamma$ einbezogen, da Photonen fälschlicherweise als Elektronen identifiziert werden können.
Es stellt sich heraus, dass der Kanal $Z' \to e^+e^-$ extrem sauber ist. Im Vergleich zum Drell-Yan Untergrund sind alle anderen Untergrundprozesse vernachlässigbar. In diesem Kapitel werden Histogramme der rekonstruierten Masse der verschiedenen Untergrunde präsentiert und verglichen. Bei $M = 1.5$ TeV erhält man eine "Signifikanz" ($\frac{S}{\sqrt{B}}$) von 100-200 für die verschiedenen Modelle.

1.7. Vollständige Simulation

In diesem Kapitel werden die Resultate einer Analyse in vollständiger Simulation vorgestellt, die viel realistischer sind als die der Analyse auf Generator-Niveau.
Wie im vorhergehenden Schritt werden die Ereignisse mit PYTHIA erzeugt. $100\,fb^{-1}$ sind für das SSM erzeugt, für die anderen Modelle jeweils die gleiche Zahl von Ereignissen (etwa 10 000) in der Peak Region. Für eine Masse von 4 TeV sind nur Ereignisse für das SSM und das KK Modell generiert worden, allerdings mit weniger Statistik als in den anderen Fällen.
Um die Analyse in der vollständigen Simulation durchzuführen, wurden in der vorliegenden Arbeit Methoden und Kriterien zur Identifikation, Isolation und Kalibration entwickelt. Die Kriterien, die in diesem Kapitel detailliert werden, wurden zu erst anhand von 'single electron', 'single photon' und 'di-jet' Simulationen bei verschiedenen Energien entwickelt und dann mithilfe der simulierten Ereignisse bei $M = 1.5\,\text{TeV}$ angepasst; während bei den Ereignissen mit $M = 4\,\text{TeV}$ lediglich eine schnelle Validierung durchgeführt wurde, die bis auf die Detektorakzeptanz in Abhängigkeit der Rapidität des Z'-Bosons sehr zufriedenstellend ist.
Die Zerfallsbreite ist nun parametrisiert durch eine (numerische) Faltung aus der Funktion, die für die natürliche Zerfallsbreite genutzt wird, und einer Funktion für die Detektorauflsung. Verschiedene vorläufige Funktionen für die Detektorauflösung werden vorgeschlagen, da noch keine allgemeine, standardisierte Elektronenidentifikation und -kalibration in ATHENA verfügbar ist.
Wie im ersten Schritt wird die Zerfallsbreite ein wenig (bis zu 20% bei einer Masse von 4 TeV) überschätzt.
Der Wirkungsquerschnitt wird wie vorher durch Abzählen unter Berücksichtigung der Detektorakkzeptanz und Detektorauflösung bestimmt.
Was die Vorwärts-Rückwärts-Asymmetrien angeht, können verschiedene der entwickelten Methoden validiert werden, andere müssen verworfen werden, z.B. wegen einer zu geringen Detektorakzeptanz. Die Methode des zweidimensionalen fits erweist sich als sehr mächtig. Asymmetrien nahe Null weisen jedoch einige Probleme auf.
Im großen und ganzen zeigt die Analyse eine Bestätigung der entwickelten Methoden hinsichtlich der beiden Massenwerte und auch hinsichtlich eines Szenarios mit einer realen Datenmenge.

1.8. ... zur Unterscheidung verschiedener Modelle und Ausblick

In der vorliegenden Arbeit werden die wichtigsten zur Unterscheidung der unterschiedlichen Erweiterungen des Standard-Modells vorgeschlagenen Variablen (Zerfallsbreite, Wirkungsquerschnitt und Vorwärts-Rückwärts-Asymmetrien) an Hand von simulierten Z' Daten, die eine vollständige Detektorrekonstruktion durchlaufen haben, untersucht. Resultate einer ersten Analyse liegen nun vor - einschliesslich der zu erwartenden Fehler. Für die Zerfallsbreite bedarf es sowohl eines besseren Verständnisses der Drell-Yan Prozesse bei diesen hohen Schwerpunktsenergien als dies bisher der Fall ist als auch der Luminosität der Partonen. Was die Asymmetrien anbelangt, können ebenso verschiedene Verbesserungsvorschläge umgesetzt werden. Andere Variablen, wie z.B. die Verteilung der Rapidität der Z' Bosonen, müssen noch hinzugefügt werden.
Außerdem liegen nun insbesondere funktionsfähige und gut geteste Methoden vor, um diese Variablen zu extrahieren. Diese können schnell und einfach auf andere Modelle oder neuere Simulationen angewandt werden.

Der nächste Schritt dürfte der Übergang zu einer neuen vollständigen Simulation sein, die realistischer sein wird und Pile-Up-Effekte mit einschließt. Ein Augenmerk muss an dieser Stelle auch auf das elektronische Rauschen gelegt werden, welches bisher noch nicht untersucht wurde. Außerdem müssen die Detektorakzeptanz und der Einfluß des Untergrunds noch genauer betrachtet werden.
Des weiteren kann nun eine Strategie zur Unterscheidung zwischen den verschiedenen Modellen entwickelt werden, da nun Methoden bekannt sind, um die Variablen zu extrahieren und außerdem auch ihre Unsicherheiten bekannt sind. Natürlich kann eine einzelne Variable nie ausreichen. Methoden, die mehrere (oder alle) Variablen integrieren, müssen gefunden werden. Verschieden Methoden wurden schon in theoretischen Artikeln vorgeschlagen, aber nie auf die Ergebnisse einer *experimentellen* Analyse angewandt.

2. Résumé français (French summary)

Etude du canal $Z' \to e^+e^-$ en simulation complète en vue de la discrimination entre des modèles au-delà du Modèle Standard

2.1. Introduction

Même si les résultats expérimentaux actuels de la physique des particules sont en bon accord avec les prédictions du Modèle Standard, on pense aujourd'hui qu'il n'est valable qu'à basse énergie. Par exemple, la gravitation n'est pas intégrée, l'interaction forte et l'interaction faible ne sont pas unifiées, les masses des quarks et leptons sont des paramètres libres,...
Plusieurs théories au-delà du Modèle Standard proposent des bosons de jauge neutres supplémentaires, appelés Z'. Ils pourraient être assez légers pour être découverts aux collisionneurs actuels et futurs. La découverte d'une telle particule serait un test direct du Modèle Standard et de notre compréhension de la physique à des échelles de masse beaucoup plus élevées.
La recherche de ces particules Z' est un aspect important du programme de physique des collisionneurs à haute énergie. Les recherches actuelles montrent que les bosons Z' sont plutôt lourds. Un boson Z' pourrait être découvert au TEVATRON au Run II s'il est plus léger qu'1 TeV. Des analyses expérimentales et théoriques détaillées ont montré que le potentiel de découverte du LHC est au moins de 5 TeV. Après la découverte d'un tel boson, ses couplages doivent être étudiés pour identifier le cadre théorique correct.

Dans ce travail, les résultats obtenus dans la construction d'outils performants pour la reconstruction des variables pour la discrimination entre les modèles dans une recherche directe d'un Z' sont présentés. Pour les données, il s'agit des simulations Monte Carlo des collisions pp avec une énergie dans le centre de masse de 14 TeV et la décroissance di-électronique ($pp \to Z' \to e^+e^-$) dans le détecteur ATLAS au LHC du CERN.
Ce résumé est organisé avec la même structure que le document principal de sorte à facilement trouver le chapitre correspondant pour avoir plus de détails.

2.2. Modèles de Z'

Parmi les différents modèles qui proposent des bosons de jauge supplémentaires, les modèles suivants ont été choisis et décrits dans ce chapitre après une courte présentation du Modèle Standard:

- ⋆ Le Modèle Standard Séquentiel Z'_{SSM}:
  Dans ce cas, le boson Z' se distingue du boson Z habituel uniquement par sa masse plus élevée. Notamment les couplages avec les fermions ne sont pas changés.

- ⋆ Modèles droite-gauche Z'_{LR}:
  Au groupe de jauge du Modèle Standard le groupe $SU(2)_R$ est ajouté, c'est à dire des interactions faibles droites chargées sont introduites. Ces modèles sont caractérisés par le rapport des couplages droit et gauche. Dans ce travail ce rapport est considéré égal à 1, c'est à dire l'interaction droite est aussi forte que l'interaction gauche.

- ⋆ Modèles E_6:
  Ces modèles ont comme origine une brisure de symétrie du groupe de jauge E_6. Deux bosons de jauge neutres supplémentaires peuvent apparaître. On suppose qu'uniquement le boson le plus léger peut être produit au LHC, il est defini par la combinaison linéaire suivante

  $$Z' = \cos\beta Z'_\psi - \sin\beta Z'_\chi.$$

  L'angle β est un paramètre libre de ces modèles, les cas populaires Z'_χ ($\beta = -\frac{\pi}{2}$), Z'_ψ ($\beta = 0$) et Z'_η ($\beta = \arctan(-\sqrt{\frac{5}{3}}) - \frac{\pi}{2}$) sont choisis.

⋆ Z' de Kaluza-Klein Z'_{KK}:
Un modèle spécifique des divers modèles avec des dimensions supplémentaires est choisi. Dans ce cas on suppose des dimensions supplémentaires grandes qui sont accessibles uniquement pour la gravitation. En plus, une dimension supplémentaire petite compactifiée est supposée qui est accessible à la gravitation et aux bosons de jauge. La signature principale du fait que les bosons de jauge peuvent se propager dans la dimension supplémentaire est l'apparition d'une tour de résonances Kaluza-Klein. La première résonance pourrait être accessible au LHC.

2.3. L'accélérateur LHC et le détecteur ATLAS

Dans ce chapitre, le LHC et le détecteur ATLAS sont présentés. Le LHC (Large Hadron Collider) est la génération prochaine des collisionneurs hadron-hadron qui est en construction au CERN, le laboratoire européen de physique des particules (Centre Européen pour la Recherche Nucléaire). Il suivra le Large Electron Positron Collider LEP et utilisera son tunnel de 27 km. Les premières collisions sont attendues pour 2007. Il y aura 4 points de collision des faisceaux et 4 expériences: ATLAS et CMS, des expériences pour la physique pp en général, LHCb pour la physique du B et ALICE pour les ions lourds.
Le LHC est remarquable par son énergie dans le centre de masse de 14 TeV et sa luminosité de l'ordre de $10^{33} - 10^{34}\, cm^{-2}s^{-1}$. ATLAS comporte plusieurs couches concentriques: le détecteur interne, les calorimètres et le détecteur à muons.
Le programme de recherche inclut des études du Modèle Standard et la recherche de la physique nouvelle, par exemple de nouvelles particules. Le détecteur ATLAS est conçu pour exploiter le potentiel total du LHC; néanmoins, la recherche du boson de Higgs a une grande importance pour ATLAS.

2.4. Propriétés de la production et des décroissances des bosons Z' aux collisionneurs hadroniques

Ce chapitre est un préalable à l'étude des variables discriminantes; la réaction étudiée y est précisée, ainsi que le contexte de sa recherche.

Le processus de production principal est le processus $q\bar{q} \to Z'$.
Le canal le plus important pour l'observation d'un Z' est la décroissance leptonique $pp \to l^+l^-X$. Les décroissances hadroniques sont difficiles à détecter parmi le bruit de fond QCD. D'autres décroissances sont trop rares ou invisibles. Parmi les canaux leptoniques le canal e^+e^- a été choisi car la résolution du détecteur ATLAS pour les électrons est meilleure comme je le montre dans ce chapitre.
Les limites de découverte d'un Z' peuvent être divisées en deux catégories: les limites directes, c'est à dire la non observation d'une résonance Z', et les limites indirectes, c'est à dire la collection de plusieurs effets où l'existence d'un Z' peut affecter une autre observable physique. Les limites actuelles détaillées dans ce chapitre sont de l'ordre de 400-1500 GeV selon les modèles. Evidemment, si un Z' avait des couplages faibles ou nuls aux fermions, ces limites seraient beaucoup plus faibles.

Si un Z' est observé au LHC, on pourra mesurer sa masse, sa largeur de décroissance, sa section efficace et ses asymétries avant-arrière. Ces variables sont sensibles aux couplages du boson aux fermions et donc au cadre théorique, elles sont donc supposées discriminer entre les modèles au-delà du Modèle Standard qui proposent des bosons de jauge supplémentaires.

2.5. Analyse au niveau de la géneration

Dans ce chapitre, une analyse au niveau de la génération est faite comme première étape pour bien comprendre la phénoménologie et pour développer et valider les méthodes d'analyse sans aucun effet d'hadronisation ou du détecteur.
Les événements sont générés avec PYTHIA dans le cadre d'ATHENA, le programme futur unique de toute simulation, reconstruction et analyse d'ATLAS. Les bosons Z' sont générés avec une masse de 1.5 TeV et 4 TeV. La première valeur est choisie car elle est réaliste par rapport aux limites actuelles de découverte et parce qu'elle offre des possiblités intéressantes pour la période de mise en service. Pour la deuxième valeur, une valeur plus elevée mais encore accessible est choisie. Le Z'_{KK} est inclus comme 'processus externe défini par l'utilisateur' ; pour les autres modèles, le processus Z' de PYTHIA est utilisé en changeant les

couplages.
Pour tous les modèles, 60 000 événements ont été générés pour les deux valeurs de masse sans radiation de l'état final et initial. Le Z' est toujours produit avec le bruit de fond irréductible provenant des processus de Drell-Yan ($q\bar{q} \to Z^\star, \gamma^\star \to e^+e^-$) et la structure d'interférence complète.
L'étude de cet effet d'interférence montre que l'interférence déforme le pic de masse, et pour tous les modèles on trouve une interférence destructive à *gauche* du pic.
La largeur de décroissance est modélisée par une fonction de Breit-Wigner relativiste et des exponentielles pour tenir compte de la luminosité des partons, de la déformation du pic par l'interférence et du Drell-Yan.
Les résultats d'un ajustement à la distribution de la masse invariante sont satisfaisants ; par rapport aux valeurs théoriques calculées préalablement (10-50 GeV selon les modèles à $M = 1.5$ TeV), on trouve une légère surestimation de 1-6% (pour une masse de 1.5 TeV). Cet effet augmente avec la masse et décroit avec la largeur.
La section efficace leptonique (20-80 fb selon les modèles à $M = 1.5$ TeV) est determinée par comptage des événements dans la région du pic avec une précision de 0.1-0.5 fb. Un bon accord avec les prédictions de PYTHIA est obtenu.
Les asymétries avant-arrière ont comme origine le fait que les proprietés de décroissance d'un Z' ne sont pas identiques dans les directions avant et arrière. Elle sont étudiées avec plusieurs méthodes (comptage, ajustements à une dimension, ajustement à deux dimensions, avec des coupures,...) pour faire face à la difficulté de définir proprement les termes *avant* et *arrière* dans une collision pp en fonction de la masse et de la rapidité de la paire de leptons reconstruits. Les résultats sont comparés avec succès avec d'autres publications. Les asymétries ne varient pas beaucoup avec la masse du boson Z'.

2.6. Bruit de fond physique

Comme bruit de fond physique, tous les signaux avec une signature e^+e^- sont considérés, de même que les signaux avec une signature $e^\pm\gamma$ car les photons peuvent être mal identifiés comme électrons.
Le canal $Z' \to e^+e^-$ se montre extrêmement propre, tous les bruits de fond sont négligeables par rapport au Drell-Yan. Des histogrammes pour la masse leptonique reconstruite sont montrés dans ce chapitre pour les différents bruits. A $M = 1.5$ TeV, on obtient une "significance" de l'ordre de 100-200 pour les différents modèles.

2.7. Simulation complète

Ce chapitre montre les résultats dans une simulation complète, beaucoup plus réalistes que dans l'analyse au niveau de la génération.
Comme dans l'étape précédente, les événements sont générés avec PYTHIA. 100 fb^{-1} ont été générés pour le SSM, et pour les autres modèles le même nombre d'événements dans le pic (environ 10 000). A 4 TeV, uniquement le SSM et le KK ont pu être étudiés avec peu de statistique.
Pour faire l'analyse dans la simulation complète, des méthodes pour l'identification, l'isolation et la calibration ont dû être developpées dans mon travail. Ces critères sont détaillés dans le chapitre principal et ont d'abord été validés sur des lots de données de 'single electrons', 'single photons' et 'dijets' à plusieurs énergies avant de passer au Z' de $M = 1.5$ TeV. Une validation rapide à $M = 4$ TeV a montré que les méthodes fonctionnent encore assez bien à cette valeur de masse élevée.
La courbe de résonance est paramétrée par une convolution (numérique) de la fonction utilisée auparavant pour la largeur naturelle et une fonction pour la résolution du détecteur. Plusieurs fonctions temporaires sont proposées pour cette résolution en attendant une identification et une calibration standard des électrons dans ATHENA. Comme au niveau de la génération, la largeur est surestimée (jusqu'à 20% dans le cas $M = 4$ TeV).
La section efficace est determinée comme auparavant par comptage en tenant compte de l'acceptance et de la résolution du détecteur.
Concernant les asymétries avant-arrière, certaines des méthodes dévéloppées au niveau de la génération ont pu être validées, d'autres ont dû être rejetées, par exemple à cause d'une acceptance du détecteur trop faible. La méthode avec l'ajustement en 2D se montre très puissante. Les asymétries proche de zéro posent le plus de difficultés.
Globalement l'analyse montre une validation des méthodes dévéloppées par rapport au changement d'énergie de 1.5 TeV à 4 TeV et par rapport à un scénario réaliste de statistique.

2.8. ... vers la discrimination et perspectives

Avec ce travail, une première analyse préliminaire des variables discriminantes principales (la largeur, la section efficace et les asymétries) est faite en simulation complète, les erreurs statistiques incluses. Pour la largeur de décroissance, il faut mieux étudier le Drell-Yan à haute énergie, de même que la luminosité des partons. Sur les asymétries, il y a également plusieurs propositions d'amélioration dans mon travail. D'autres variables, comme par exemple la distribution en rapidité des bosons Z', doivent encore être étudiées.
Des outils bien testés sont maintenant disponibles pour l'analyse des variables principales - qui pourront facilement et rapidement être appliqués à d'autres modèles ou simulations.

Dans une prochaine étape, il faudra passer d'une part à une nouvelle simulation complète qui sera plus réaliste, où l'empilement sera inclus. Le bruit de fond électronique est à étudier en même temps. A ce moment l'acceptance et l'effet du bruit de fond physique seront aussi étudiés plus en détail.
D'autre part, une stratégie de discrimination peut être élaborée connaissant les méthodes pour extraire ces variables avec leurs incertitudes. Evidemment, une seule variable ne peut pas suffire, il faut trouver des méthodes pour combiner plusieurs variables. Plusieurs méthodes ont déjà été proposées et étudiées dans des articles théoriques mais jamais appliquées aux résultats d'une analyse *expérimentale*.

3. Introduction

Elementary-particle physics is the study of the basic nature of matter, of force, of time and of space. The simplest constituents of matter, which are called elementary particles, are searched for and the basic forces that operate between them are studied. Today, we look for a unified theory that describes all interactions. It is already possible to describe all forces besides gravity in a common theory.
The belief in fundamental particles dates back to 5^{th} century BC, when it was proposed that everything on earth was composed of small invisible entities - atoms. Throughout human history, mankind has tried to explain the world as made up of some basic kinds of matter. The classical Greek believed in four elements: earth, air, fire and water. In subsequent centuries, alchemists and philosophers added aether, mercury, sulfur, salt, and so on. After Mendeleev published the periodic table of elements in 1872, the basic types of matter where thought to be about 100 different chemical elements. Later, matter was proven to consist of protons, neutrons and electrons.
In 1678 Isaac Newton established the first mathematical notation of a fundamental force: his gravitation theory which was replaced in 1915 by Albert Einstein's General Theory of Relativity. About 200 years later, in 1865, James Clerk Maxwell unified the electric and magnetic force to the electromagnetic force. He predicted electromagnetic waves, that were discovered in 1886 by Heinrich Hertz in Karlsruhe. This was the first unification of two elementary forces.

1897	The electron was discovered by Thomson, implying an inner structure of the atoms.
1905	Einstein's theory of relativity brought a new understandings of time and space.
1911	Rutherford's atom model: a positively-charged nucleus and electrons orbiting around it.
1913	Bohr devised the first successful quantitative model for atomic structure.
1928	Dirac introduced relativistic quantum mechanics and predicted antimatter.
1932	Anderson discovered the positron, the long-awaited antiparticle of the electron.
1934	Fermi proclaimed the existence of the weak force.
1937	The muon was discovered. Its behavior is identical to electron's but it is 200 times heavier.
1948	Quantum electrodynamics (QED) was developed by Feynman, Schwinger and Tomonaga.
1955	The neutrino was discovered.
1961	$SU(3)$ was proposed by Gell-Mann and Ne'eman.
1964	Gell-Mann and Zweig came up with Quark Model. Up, down and strange quarks were named.
1965	Quarks carried a new type of charge: color (red, green and blue).
1967	Weinberg, Glashow and Salam developed unified electroweak theory.
1970s	In early 1970s, Quantum Chromodynamics (QCD) was developed to describe the strong interactions.
1974	The discovery of J/Ψ particle proved the existence of a fourth quark: the charm quark.
1975	A "super-heavy" electron, the tau, was discovered.
1977	The bottom quark was discovered at FERMILAB.
1977	Evidence for the Υ resonance.
1983	Gauge bosons (Z,W) are discovered at CERN.
1994/5	The top quark was discovered by CDF and D$\emptyset$ at FERMILAB.
1998	The SUPER-KAMIOKANDE collaboration found evidence of neutrino oscillation.
2000	FERMILAB reported the first direct observation of tau neutrinos.

Table 3.1.: *A Chronology of Particle Physics*

In 1898 Ernest Rutherford discovered the radioactive beta-decay, this was the first hint for another fundamental interaction. Enrico Fermi established in 1934 a theory of the weak force.
Experiments were under way to probe the sub-structures of these particles and the forces between them. During decades of experiments, physicists not only discovered numbers of new particles, but also successfully classified them. For example, the positron is a "positively-charged" electron and belongs to the

antiparticle family predicted by Relativistic Quantum Mechanics. Muons and neutrinos are electron-like structureless particles, called leptons.
Hadrons, such as π^0, K^+, Λ, etc., which are produced by the strong force (the one that holds the nucleus together) and decay by the weak force (the one that accounts for radioactive decay), were discovered. It became clear that the proton, the neutron and the other hadrons are composite systems made up of much smaller particles called quarks. Leptons and quarks are thought to be elementary.
In 1967, Sheldon Glashow, Abdus Salam and Steven Weinberg succeeded to unify the electromagnetic and the weak force to the so-called electroweak force with their famous Glashow-Salam-Weinberg model. In 1973, Harald Fritzsch and Murray Gell-Mann established the Quantum Chromodynamic, which describes the strong interaction.
Four basic interactions (i.e. the strong, weak, electromagnetic and gravitational forces) were established. A unified theory of the weak and electromagnetic forces now exists. Quantum Chromodynamics (QCD) successfully described the strong interactions. Except for the gravitational force, the strong, weak and electromagnetic interactions are now well described by similar mathematical theories called gauge theories. The collections of these theories is called the Standard Model (SM).
A annotated chronology of particle physics is given in Table 3.1 [1].

To achieve these remarkable results and discoveries, better detectors had to be designed and more and more powerful accelerators had to be built.
During the first half of this century, achievements in Europe dominated progress in the physics, from the discovery of the electron to the atomic nucleus and its constituents, from special relativity to quantum mechanics. By the early 50s, the Americans had understood that further progress needed more sophisticated instruments, and that investment in basic science could drive economic and technological development. While scientists in Europe still relied on simple equipment based on radioactivity and cosmic rays, powerful accelerators were being built in the US. Table-top experiments were being overtaken by projects involving large teams of scientists and engineers.
A few far-sighted physicists, such as Paul, Rabi, Amaldi, Auger and de Rougemont, perceived that cooperation was the only way forward for front-line research in Europe. Despite fine intellectual traditions and prestigious universities, no European country could manage alone. The creation of a European Laboratory was recommended at a UNESCO meeting in Florence in 1950, and less than three years later a Convention was signed by 12 countries of the Conseil Européen pour la Recherche Nucléaire. CERN was born, the prototype of a chain of European institutions in space, astronomy and molecular biology, and Europe was poised to regain its illustrious place on the scientific map.
CERN exists primarily to provide European physicists with accelerators that meet research demands at the limits of human knowledge. In the quest for higher interaction energies, the Laboratory has played a leading role in developing colliding beam machines. Notable "firsts" were the Intersecting Storage Rings (ISR) proton-proton collider commissioned in 1971, and the proton-antiproton collider at the Super Proton Synchrotron (SPS), which was commissioned in 1981 and produced the massive W and Z particles two years later, confirming the unified theory of electromagnetic and weak forces. The main impetus lately was from the Large Electron-Positron Collider (LEP), where measurement have been testing our best description of sub-atomic Nature, the Standard Model, to a fraction of 1% up to one part in a thousand. By 1996, the LEP energy was doubled to 90 GeV per beam in LEP II, opening up an important new discovery domain. More high precision results have been established in abundance throughout the rest of the last decade, which have substantially improved our understanding.
LEP data are so accurate that they are sensitive to phenomena that occur at energies beyond those of the machine itself; rather like delicate measurement of earthquake tremors far from an epicenter. This gives us a "preview" of exciting discoveries that may be made at higher energies, and allow us to calculate the parameters of a machine that can make these discoveries. All evidence indicates that new physics, and answers to some of the most profound questions of our time, lie at energies around 1 TeV. To look for this new physics, the next research instrument in Europe's particle physics armory is the LHC (Large Hadron Collider). In keeping CERN's cost-effective strategy of building on previous investments, it is designed to share the 27-kilometer LEP tunnel, and be fed by existing particle sources and pre-accelerators. A challenging machine, the LHC will use the most advanced superconducting magnet and accelerator technologies ever employed. LHC experiments are, of course, being designed to look for theoretically predicted phenomena. However, they must also be prepared, as far as is possible, for surprises. This will require great ingenuity on the part of the physicists and engineers.
The LHC will be a remarkably versatile accelerator. It can collide proton beams with energies around

7-on-7 TeV at unprecedented luminosities, providing the experiments with high interaction rates. It can also collide beams of heavy ions such as lead with a total collision energy in excess of 1250 TeV, about thirty times higher than at the Relativistic Heavy Ion Collider (RHIC) constructed at the Brookhaven Laboratory in the US. The research, technical and educational potential of the LHC and its experiments is enormous.
The main goals of the LHC (and ATLAS) program is to discover and study the Higgs particle and to discover and study new particles (for example extra gauge bosons) that lead to unified theories beyond the SM.

Motivation and organization of this diploma thesis

Although experimental results so far agree with predictions of the Standard Model, it is widely felt to be incomplete. For example, gravitation is left outside the framework; strong and weak interactions are not unified; it does not tell us what determines the basic properties of quarks and leptons, such as their masses. Moreover, there is the serious problem known as the "hierarchy" problem[1]; for these reasons, physicists have been motivated to search for physics beyond the Standard Model.
Many prospective theories beyond the Standard Model predict an extra neutral gauge boson[2], denoted by Z', which might be light enough to be accessible at current and/or future colliders. The discovery of such a particle would provide a direct test of the Standard Model and an important probe of underlying physics at much higher mass scales.

The search for these Z' particles is an important aspect of the experimental physics program of high-energy colliders. Present results show that a new Z' boson would be rather heavy (in the TeV range). It could still be discovered at TEVATRON. Detailed theoretical and experimental analysis [3] have shown that the discovery potential of the LHC experiments is very high (at least about 5 TeV). After the discovery of a Z' boson, some diagnosis of its couplings needs to be done in order to identify the correct theoretical frame.

In this work, I present a study of Z' production through pp collisions at a center-of-mass energy of $\sqrt{s}$=14 TeV. As decay process the di-electron channel was chosen: $pp \to Z' \to e^+e^-$. The data are Monte-Carlo simulations for the ATLAS detector at LHC. The objective is to study the observables that are expected to discriminate between models beyond the Standard Model in full simulation and to estimate the precision on their measurement. The longterm aim is to elaborate a full discrimination strategy.

The present document is organized as follows:
In the next chapter, the theoretical framework in which the analysis will be performed is described. In chapter 5 the LHC accelerator and ATLAS detector are presented. In chapter 6 the relevant observables that can be measured at ATLAS, namely the dilepton cross-section, the total decay width and forward-backward asymmetries are described, together with the context of the Z' search. The analysis of these observables is presented on the one hand at generation level in chapter 7 and on the other hand in full simulation in chapter 9. The physical background to the signal is studied in chapter 8. In chapter 10 an outlook on discrimination is given.

[1] Disparity between the electroweak and the 4-dimensional Planck scales.
[2] Force-carrying neutral particle for the weak interaction.

4. Z' Models and phenomenology

4.1. Review: The Standard Model...

The Standard Model (SM) of elementary particle physics describes the fundamental components of matter and their interactions. It describes successfully three of the basic four forces of nature: the electromagnetic, the weak, and the strong force. The gravitational force is not incorporated into the SM. It is described by General Relativity and neglected on the microscopic scales.

4.1.1. Elementary particles and forces

According to the knowledge of today, matter is made up of fermions, e.g. particles with half-integral spin, which must obey Fermi Dirac statistics[1]. They are divided in leptons and quarks and are grouped into 3 generations. There are 3 flavors of leptons (e, μ and τ and the associated neutrinos ν) and six flavors of quarks: up (u), down (d), charm (c), strange (s), top (t) and bottom (b). Unlike the leptons, the quarks possess fractional electric charge. In addition quarks also possess an internal degree of freedom called color, which can take three possible values: red, blue and green.
Corresponding particles in the 3 generations agree in all gauge quantum numbers, they differ only in mass. Experimentally, the masses of the neutrinos are constrained to be small, the SM assumes that they are massless. Table 4.1 shows the properties of leptons and quarks [4].
Free quarks are not observed, they are confined to hadrons: baryons and mesons. Baryons are fermions consisting essentially of three quarks (for example the proton: $p = (uud)$), mesons are bosons and consist essentially of one quark and one antiquark (for example the π meson: $\pi^+ = (u\bar{d})$).

Generation	Leptons (spin 1/2)			Quarks (spin 1/2)		
	Flavors	Charge ($\|e\|$)	Mass (GeV/c^2)	Flavors	Charge ($\|e\|$)	Mass[2](GeV/c^2)
1	ν_e	0	$< 3 \times 10^{-9}$	u	+2/3	1.5-4.5 $\times 10^{-3}$
	e	-1	5.11 $\times 10^{-4}$	d	-1/3	5-8.5 $\times 10^{-3}$
2	ν_μ	0	$< 1.9 \times 10^{-4}$	c	+2/3	1.0-1.4
	μ	-1	0.106	s	-1/3	0.080-0.155
3	ν_τ	0	< 0.019	t	+2/3	174-178
	τ	-1	1.78	b	-1/3	4.0-4.5

Table 4.1.: *Fermions in the Standard Model [4]*

The other fundamental particles are the force-carrying particles (gauge bosons). Gauge bosons have spin 1 and obey Bose-Einstein statistics[3].
For each particle, there also exists an antiparticle[4] with the same mass and spin, but with opposite values for all quantum numbers.
The charged leptons interact only via the electromagnetic and weak forces, while the neutrinos interact only via the weak force. Quarks interact via the strong force as well as the electromagnetic and weak forces. In strong interactions, color plays a role similar to the role of the electric charge in electromagnetic interactions.
The gauge bosons are the mediators of the forces between different particles. The SM treats each interaction as a field and interprets the excitations in the field as particles. An interaction between two particles is viewed as a process in which these two particles exchange a virtual gauge boson. The properties of the forces and their force-carriers are summarized in table 4.2 [5].

[1] Fermi-Dirac statistics require that no two particles within a given system be in the same state, e.g. have the same energy and quantum numbers.
[2] Due to quark confinement, free quarks are not to be found in nature; hence, their masses cannot be determined precisely. The measurements depend on the energy probes used and the hadronic systems studied.
[3] Bosons can be brought together without restriction, i.e. they can occupy the same state.
[4] some particles are their own antiparticle

Type of force	Gravity	Electromagnetic	Weak	Strong
Gauge bosons	Graviton	Photon (γ)	$W^{\pm}$,Z	gluon (g)
Mass (GeV/c^2)	0	0	$W^{\pm}$: 80.432 ± 0.039 [4] Z: 91.1876 ± 0.0021 [4]	0
acts on (matter only)	all particles	electrically charged particles	leptons, quarks	quarks
relative strength	10^{-38}	1/137	10^{-5}	1
range	∞	∞	10^{-18} m	$\leq 10^{-15}$ m

Table 4.2.: *The four basic forces and their force-carrying particles [5]*

The electromagnetic force is an interaction between particles having electric charge. It has an infinite range and is responsible for the attraction between electrons and the atomic nuclei. It is mediated by the photon, and is described by Quantum Electrodynamics (QED). Any two charged particles interact by coupling to the photon.
The weak interaction has a very short range and exists between any of the leptons and quarks. It is responsible for reactions like radioactive β decays. It is mediated by the $W^{\pm}$ and Z bosons. In the SM, electromagnetic an weak interaction have been unified in the Glashow-Salam-Weinberg model, known as Electroweak theory.
The strong interaction is a short-range force that affects particles carrying color charge. It is responsible for binding quarks together and building nucleons and mesons. It is mediated by gluons and is described by Quantum Chromodynamics (QCD). There are a total of 8 gluons, which couple to particles possessing color charge (these particles are the quarks and the gluons themselves, this auto-coupling is non-abelian).

In the following sections the electroweak gauge theory will be developed in a more precise and above all more mathematical way, starting with the simplest case of a gauge theory: QED.

4.1.2. Electroweak theory [6]

In the electroweak theory left handed electrons and neutrinos are regarded as a doublet (ν_e, e), i.e. as two members of the same family. The associated quantum number is the weak isospin ($\frac{1}{2}$ for the electron and $-\frac{1}{2}$ for the neutrino.) This doublet is described by a two-component field $\mathbf{\Psi} = (\Psi_\nu, \Psi_e)$. A transformation that changes one member of a doublet into the other is introduced, it belongs to the symmetry group $SU(2)$ of unitary unimodular transformations in two dimensions. This symmetry is combined with a simultaneous $U(1)$ symmetry for the hypercharge interaction. This is the $SU(2)_L \times U(1)$ Glashow-Salam-Weinberg theory of electroweak interactions with 4 gauge bosons. The gauge bosons cannot all be massless (excluded by experiments), so the symmetry cannot be exact. The symmetry is broken spontaneously, in a way that retains renormalizability, the result is one massless gauge boson γ (made from a linear combination from the neutral boson from $SU(2)_L$ and the boson from $U(1)$: $\gamma = W^0 \sin\theta_w + B^0 \cos\theta_w$) and three massive gauge bosons W^+, W^- and Z^0 (the orthogonal combination from the γ). The angle θ_w is a parameter of this unified electroweak theory: the electroweak mixing angle.
In fact, the $SU(2)$ gauge transformation operates only on left-handed particles (hence the notation $SU(2)_L$). The distinction between right and left-handed particles was motivated by parity violation in electroweak processes. For example the experiment by Wu [7] showed that electrons produced by β-decay have a preferred helicity. The right-handed states are singlets that do not change under $SU(2)_L$; for antiparticles one has to change left and right handedness. There is no right-handed neutrino state in the SM, since the neutrino is assumed to be massless in the SM.
So one gets the following representation for the first generation:

$$(u_L, d_L), (\nu_{eL}, e_L), \bar{u}_L, \bar{d}_L, \bar{e}_L,$$

$$(\bar{d}_R, \bar{u}_R), (\bar{e}_R, \bar{\nu}_{eR}), u_R, d_R, e_R.$$

Gauge theories: QED

Gauge invariance is a central feature of modern field theories, because it ensures that calculated observables are finite (i.e. the amplitudes in a perturbation expansion are renormalizable). QED was the first

gauge theory and it is the simplest one.
The Lagrangian $\mathcal{L}$ for the massless electromagnetic (photon) field A_μ interacting with a spin-$\frac{1}{2}$ field Ψ of mass m (for example the electron) is[5]

$$\mathcal{L} = -\frac{1}{4}F_{\mu\nu}F^{\mu\nu} + \bar{\Psi}(i\gamma^\mu D_\mu - m)\Psi.$$

Here, $F_{\mu\nu}$ is the electromagnetic field tensor

$$F_{\mu\nu} = \partial_\mu A_\nu - \partial_\nu A_\mu,$$

and D_μ is the covariant derivative

$$D_\mu = \partial_\mu + ieA_\mu Q,$$

where e is the unit of electric charge and Q is the charge operator $Q\Psi = q\Psi$ (i.e. $Q\Psi = -\Psi$ for an electron). γ^μ are the Dirac γ matrices and it is $\gamma^5 = i\gamma^0\gamma^1\gamma^2\gamma^3$.
This Lagrangian is invariant under local gauge transformations $U(x)$

$$\Psi(x) \to U(x)\Psi(x), \qquad A_\mu(x) \to A_\mu(x) + \partial_\mu\alpha(x)$$

with

$$U(x) = exp(-ieQ\alpha(x))$$

and arbitrary $\alpha(x)$. Local gauge invariance requests that there is a gauge field A_μ which interacts with fermions in a prescribed way. Had we started from non-interacting Ψ fields, the Lagrangian would already have been invariant under global transformations (U independent from x) but local gauge invariance would have required the existence of A_μ fields plus the interaction term

$$\mathcal{L}_{int} = -eJ^\mu_{em}A_\mu, \quad \text{where} \qquad J^\mu_{em} = \bar{\Psi}\gamma^\mu Q\Psi,$$

and J^μ_{em} is the electromagnetic current.
In the language of group theory, the gauge transformation above with a scalar phase $\alpha(x)$ belongs to a unitary group $U(1)$ and the full Lagrangian is said to have the symmetry $U(1)_Q$ with the charge operator Q as generator.

$SU(2)$ symmetry

Gauge transformations can also involve internal degrees of freedom. Consider, for example, an internal symmetry group $SU(2)$ such as isospin under which spin-$\frac{1}{2}$ fields $\boldsymbol{\Psi}$ transform as doublets[6]. Their free-field Lagrangian is

$$\mathcal{L}_{\text{free}} = \bar{\boldsymbol{\Psi}}(i\gamma^\mu\partial_\mu - m)\boldsymbol{\Psi},$$

where $\bar{\boldsymbol{\Psi}}$ is a row vector and $\boldsymbol{\Psi}$ is a column vector in isospin space.
In analogy with QED, we now require invariance under the infinitesimal local gauge transformation

$$\boldsymbol{\Psi}(x) \to [1 - ig\boldsymbol{\alpha}(x)\cdot\boldsymbol{T}]\boldsymbol{\Psi}(x),$$

where $\boldsymbol{\alpha(x)}$ is an arbitrary infinitesimal vector in isospin space and $\boldsymbol{T}$= (T_1, T_2, T_3) is the isospin operator whose components T_i are the generators of $SU(2)$ symmetry transformations. The T_i do not commute[7],

$$[T_i, T_j] = i\epsilon_{ijk}T_k,$$

and the gauge group is said to be non-abelian. Operating on isospin doublets, the matrix representation is $T_i = \frac{1}{2}\tau_i$, where τ_i are the Pauli matrices.
The $\boldsymbol{\Psi}$-field part of the Lagrangian can be made gauge invariant by introducing an appropriate covariant derivative D_μ:

$$\mathcal{L} = \bar{\Psi}(i\gamma^\mu D_\mu - m)\Psi, \qquad \text{where} \quad D_\mu = \partial_\mu + ig\boldsymbol{W_\mu}\cdot\boldsymbol{T},$$

[5] Summation on repeated indices is understood.
[6] Now, $\boldsymbol{\Psi}$ designs the doublet electron and neutrino.
[7] ϵ_{ijk} is the total asymmetric tensor, the structure function of this symmetry group

that provides an isospin triplet of Yang-Mills gauge fields $W_{i\mu}$ (i=1,2,3) that transform simultaneously as

$$\boldsymbol{W_\mu}(x) \to \boldsymbol{W_\mu}(x) + \partial_\mu \boldsymbol{\alpha}(x) + g\boldsymbol{\alpha}(x) \times \boldsymbol{W_\mu}(x).$$

This transformation on the gauge field is more complicated than in the QED case, because of the non-abelian property.
It remains to chose a gauge-invariant form for the $\boldsymbol{W}$field part of the Lagrangian. This can be achieved by taking

$$\mathcal{L}_W = -\frac{1}{4} W_{\mu\nu} \cdot W^{\mu\nu},$$

where

$$W_{\mu\nu} = \partial_\mu \boldsymbol{W_\nu} - \partial_\nu \boldsymbol{W_\mu} - g\boldsymbol{W_\mu} \times \boldsymbol{W_\nu}.$$

In addition to the normal kinetic energy terms, this introduces cubic and quadratic self-couplings of the $\boldsymbol{W}$ fields.
An $SU(2)$ gauge model is a candidate for weak interactions theory, since the isospin triplet $\boldsymbol{W}$ could consists of W^+, W^0, W^- bosons to transmit the weak force, with

$$W^\pm_\mu = \frac{1}{\sqrt{2}}(W_{1\mu} \mp iW_{2\mu}), \qquad W^0_\mu = W_{3\mu},$$

where the field operators $W^\pm_\mu$ are defined to annihilate $W^\pm$ bosons. However, this model is unsatisfactory for a variety of reasons. Most importantly, the effective low-energy form of weak interactions implies that the charged bosons must be very massive, and also implies a left-handed structure for charged-current couplings. Moreover, it would be desirable to unify weak and electromagnetic interactions in a single gauge theory.

$SU(2)_L \times U(1)$ Glashow-Salam-Weinberg theory

To generate the left-handed structure of charged-current weak interactions, $SU(2)$ gauge symmetry is applied to the left-handed fermion fields $\boldsymbol{\Psi_L}$ only, where $\boldsymbol{\Psi_{R/L}}$ is defined by

$$\boldsymbol{\Psi_{R/L}} = \frac{1 \pm \gamma^5}{2} \boldsymbol{\Psi}.$$

A fermion mass term $m\bar{\boldsymbol{\Psi}}\boldsymbol{\Psi}$ would not be invariant under $SU(2)$, so we take massless fermions. The conserved quantum number is weak isospin T_L.
In addition to $SU(2)_L$, an independent $U(1)_Y$ gauge symmetry is introduced whose conserved quantum number Y is called weak hypercharge. The $U(1)_Y$ symmetry is essential in order to incorporate the electric charge Q and unify the weak and electromagnetic interactions. The weak hypercharge is given by

$$Q = T_3 + \frac{1}{2}Y.$$

Right-handed fermions transform only under $U(1)_Y$, there are no right-handed neutrinos. The weak quantum numbers are given in table 4.3.

	T	T_3	$\frac{1}{2}Y$	Q
ν_{eL}	1/2	1/2	-1/2	0
e_L	1/2	-1/2	-1/2	-1
u_L	1/2	1/2	1/6	2/3
d_L	1/2	-1/2	1/6	-1/3
e_R	0	0	-1	-1
u_R	0	0	-2/3	2/3
d_R	0	0	-1/3	-1/3

Table 4.3.: *Electroweak quantum numbers*

The massless gauge fields in this model are an isotriplet $\boldsymbol{W_\mu}$ for $SU(2)_L$ and a singlet B_L for $U(1)_Y$. The Lagrangian is

$$\mathcal{L} = -\frac{1}{4} W^{\mu\nu} \cdot W_{\mu\nu} - \frac{1}{4} B^{\mu\nu} B_{\mu\nu} + \bar{\boldsymbol{\Psi}} i\gamma^\mu D_\mu \boldsymbol{\Psi},$$

with separate fermion term for each field $\boldsymbol{\Psi_L}$ and $\boldsymbol{\Psi_R}$. $W_{\mu\nu}$, $B_{\mu\nu}$ are defined as above, the covariant derivative is

$$D_\mu = \partial_\mu + ig\boldsymbol{W_\mu}\cdot\boldsymbol{T} + ig'\frac{1}{2}B_\mu Y.$$

The Lagrangian is invariant under the infinitesimal local gauge transformations for $SU(2)_L$ and $U(1)_Y$ independently.
The isospin operator T can be represented by the Pauli matrices $\boldsymbol{\tau}$, one defines the operators $T^\pm = (T_1 \pm iT_2)/\sqrt{2}$, so $\boldsymbol{W}\cdot\boldsymbol{T} = W^+T^+ + W^-T^- + W_3T_3$.
To unify electromagnetic and weak interactions the electromagnetic term $ieQA$ must be contained in the neutral term $i(gW_{3\mu}T_3 + g'\frac{1}{2}B_\mu Y)$ of D_μ, so W_3 and B must be a linear combination of A and another neutral field called Z.

$$\begin{pmatrix} W_3 \\ B \end{pmatrix} = \begin{pmatrix} \cos\theta_w & \sin\theta_w \\ -\sin\theta_w & \cos\theta_w \end{pmatrix} \begin{pmatrix} Z \\ A \end{pmatrix},$$

where θ_w is the electroweak mixing angle. It follows

$$g = e/\sin\theta_w, \qquad g' = e/\cos\theta_w,$$

and one defines

$$g_Z = \frac{e}{\sin\theta_w\cos\theta_w} \quad \text{and} \quad x_w = \sin^2\theta_w.$$

Finally one gets for $\mathcal{L}'$ (interaction gauge bosons and fermion field $\boldsymbol{\Psi}$):

$$-\mathcal{L}' = eJ^\mu_{em}A_\mu + \frac{g}{\sqrt{2}}(J^{+\mu}_L W^+_\mu + J^{-\mu}_L W^-_\mu) + g_Z J^\mu_Z Z_\mu,$$

where

$$\begin{aligned} J^{\pm\mu}_L &= \sqrt{2}\bar{\boldsymbol{\Psi}}\gamma^\mu T^\pm_L \boldsymbol{\Psi}, \\ J^\mu_Z &= \bar{\boldsymbol{\Psi}}\gamma^\mu[T_{3L} - x_w Q]\boldsymbol{\Psi}, \\ J^\mu_{em} &= \bar{\boldsymbol{\Psi}}\gamma^\mu Q\boldsymbol{\Psi}. \end{aligned}$$

$\boldsymbol{T_L}$ vanishes on $\boldsymbol{\Psi_R}$ and is represented by $\boldsymbol{T_L} = \frac{1}{2}\boldsymbol{\tau}$ on $\boldsymbol{\Psi_L}$.
For a given θ_w all gauge couplings are determined by the electric charge e.

The deficiency of this model is the fact, that the gauge bosons and the fermions are all massless. The problem is to generate mass while preserving renormalizability of the gauge theory. The Higgs mechanism is proposed to break this symmetry and to generate mass in this way. Mass is generated with the help of an isospin doublet of scalar mesons called Higgs scalars, which generate mass as a result of self-interaction. The suggested Higgs boson is not discovered yet and may not be discovered. This topic is outside the scope of the present study and will thus not be presented in more details.

For the present study the part of $\mathcal{L}'$ which describes the interactions between the Z boson and all fermions (sum over i) is the important one:

$$\begin{aligned} \mathcal{L}_Z &= -g_Z J^\mu_Z Z_\mu \\ &= -\frac{g}{\cos\theta_w}\sum_i \bar{\boldsymbol{\Psi}}_{\boldsymbol{i}}\gamma^\mu[T_{3L} - x_w Q]\boldsymbol{\Psi}_{\boldsymbol{i}} Z_\mu \\ &= -\frac{g}{2\cos\theta_w}\sum_i \bar{\boldsymbol{\Psi}}_{\boldsymbol{i}}\gamma^\mu[g^i_V - g^i_A\gamma^5]\boldsymbol{\Psi}_{\boldsymbol{i}} Z_\mu \end{aligned}$$

with

$$g^i_V = t^i_{3L} - 2\cdot q_i x_w, \quad \text{and} \quad g^i_A = t^i_{3L}.$$

The coupling constants g_V and g_A are presented in table 4.4.

e		ν		u		d	
g_V	g_A	g_V	g_A	g_V	g_A	g_V	g_A
$-\frac{1}{2}+2x_w$	$-\frac{1}{2}$	$\frac{1}{2}$	$\frac{1}{2}$	$\frac{1}{2}-\frac{4}{3}x_w$	$\frac{1}{2}$	$-\frac{1}{2}+\frac{2}{3}x_w$	$-\frac{1}{2}$

Table 4.4.: *Couplings of the fermions to the Z gauge boson,* $x_w = \sin^2\theta_w$

4.1.3. ...and beyond

Grand Unified Theories (GUTs) postulate that the $SU(3)$[8], $SU(2)$ and $U(1)$ symmetry groups of the SM have a common origin as subgroups of some larger symmetry group G. At sufficiently large energy scales this symmetry is supposed to be unbroken, all interactions are described by the corresponding local gauge theory and all running couplings coincide. Below some critical energy scale, G is spontaneously broken and the 3 couplings become independent, explaining why they widely differ at the much lower energies where they have been measured.
The Lie groups $SU(5)$, $SO(10)$ and E_6 are among those suggested as candidate GUT symmetries.
GUT[9] models always predict more gauge bosons, since W, Z, γ and g are not enough to secure local gauge invariance within a larger group. In many GUT models the extra gauge bosons might be light enough to be accessible in future colliders.
GUT models also bring problems, in particular the hierarchy problem: how can relatively light mass scales like M_Z arise naturally in a theory where the basic energy scale[10] is so much larger? A possible answer is Supersymmetry (SUSY), which proposes a unified treatment of particles with different spins. SUSY could resolve the hierarchy problem.
Other examples of extensions of the SM are string theory or extra dimensions. In string theory the fundamental objects are one-dimensional strings rather than points in space, a string can have excitations and the zero mass modes can represent fundamental particle states. Extra dimensions are either supposed to be compactified so that we could not yet have accessed them, or they are supposed to be seen only by gravitation. In both cases extra gauge bosons are proposed.

We will first discuss models where new gauge bosons associated to E_6 are observed. In string theory certain compactifications lead naturally to an E_6 gauge group or one of its subgroup. E_6 has 4 neutral gauge bosons, that can be identified with the photon, the usual Z and two new ones. If by some mechanism the last two acquire large masses, the low-energy Lagrangian reduces to the SM. However, it is possible that one (or two) of the extra gauge bosons survive at low energies [8].
We will discuss as well new gauge bosons that occur in extra dimension models: the Kaluza-Klein excitations of the gauge bosons in the case of "small" ($\sim 1\,\mathrm{TeV}$) extra dimensions.
Other models, that predict extra gauge bosons as-well, like the Bess or the Little Higgs model are not studied in this work. The graviton [9] that could have the same signature is not taken into account either.

4.2. Simplest gauge extension of the Standard Model [10]

The simplest gauge extension of the Standard Model results from adding only one extra neutral gauge boson Z'. The electroweak gauge group enlarges by including one extra $U'(1)$ factor: $SU(2)_L \times U(1)_Y \times U'(1)$. We will assume that the new charge Q' operator commutes with the $SU(2)_L$ generators T_i; family universality is also assumed.

4.2.1. General case of $U^1(1) \times U^2(1)$

Ψ_k ($k = 1..n$) are n massless fermions with different $U^a(1), a = 1, 2$ charges Y^a_k. A^b_μ are the massless gauge bosons. The most general Lagrangian reads in this case:

$$\mathcal{L} = -\frac{1}{4}F^b_{\mu\nu}F^{b\mu\nu} + \bar{\Psi}_k i\partial\!\!\!/\Psi_k + \bar{\Psi}_k\gamma^\mu Y^a_k \Psi_k g_{ab} A^b_\mu,$$

with $F^b_{\mu\nu} = \partial_\mu A^b_\nu - \partial_\nu A^b_\mu$. For g_{ab} diagonal, this would be standard QED with two different interactions, but in general g_{ab} is not diagonal, the off-diagonal gauge couplings are even observable.

[8] gauge group of QCD, it is not presented in this review of the Standard Model
[9] The simplest GUT theories are already excluded by measurements on $\sin\theta_w$ or the proton lifetime.
[10] The unification scale is at about $10^{16}\,\mathrm{GeV}$.

In the neutral sector of the SM $U(1)_{T_3} \times U(1)_Y$ g_{ab} is diagonal, because there is a symmetry reason. $U(1)_{T_3}$ is within $SU(2)_L$ and no mixing among the massless gauge bosons from $SU(2)_L$ and $U(1)_Y$ is allowed. From the invariance of the previous Lagrangian under the rotation of the gauge bosons it follows that g_{ab} is triangular (i.e. $g_{ab} = 0, a > b$), 3 physical couplings remain.

4.2.2. General case of $SU(2)_L \times U^1(1) \times U^2(1)$

The interacting neutral current Lagrangian reads in this case for Standard Model fermions:

$$-\mathcal{L}_{NC} = \bar{\Psi}_k \gamma^\mu [T_{3k} g W_{3\mu} + Y_k g'_{11} B'_\mu + Y_k g'_{12} Z'_{2\mu} + Q'_k g'_{21} B'_\mu + Q'_k g'_{22} Z'_{2\mu}] \Psi_k,$$

where T_3 and Y are the standard isospin and hypercharge, Q' is the extra $U'(1)$ charge. As above, g'_{ab} can be made triangular:

$$-\mathcal{L}_{NC} = \bar{\Psi}_k \gamma^\mu [T_{3k} g W_{3\mu} + Y_k g_{11} B_\mu + Y_k g_{12} Z_{2\mu} + Q'_k g_{22} Z_{2\mu}] \Psi_k,$$

where $B'_\mu = \cos' \alpha B_\mu - \sin' \alpha Z_{2\mu}$, $Z'_{2\mu} = \sin' \alpha B_\mu + \cos' \alpha Z_{2\mu}$, where α is the boson rotation angle, where g_{11}, g_{12} and $g_2 \equiv g_{22}$ are measurable couplings and where $g_{21} = 0$.
The photon is defined as a combination of $W_{3\mu}$ and B_μ: $W_{3\mu} = \sin\theta_w A_\mu + \cos\theta_w Z_{1\mu}$, $B_\mu = \cos\theta_w A_\mu - \sin\theta_w Z_{1\mu}$.
In general we then get:

$$-\mathcal{L}_{NC} = e \sum_i q_i \bar{\Psi}_i \gamma^\mu \Psi_i A_\mu + \frac{g}{2\cos\theta_w} \sum_i \bar{\Psi}_i \gamma^\mu (g_V^i - g_A^i) \bar{\Psi}_i Z_{1\mu} + \frac{g}{2\cos\theta_w} \sum_i \bar{\Psi}_i \gamma^\mu (g_{V'}^i - g_{A'}^i) \Psi_i Z_{2\mu},$$

where the couplings are functions of $g_2 \equiv g_{22}$ and $\frac{g_{12}}{g_{22}}$; they are given in table 4.5. The extra charges q' for the left- and right-handed fermions are given in the next section for the studied models.
There are the following relations:

$$\begin{aligned}
g_{11} &= \frac{e}{2\cos\theta_w} \\
e &= \frac{2 g g_{11}}{\sqrt{g^2 + 4 g_{11}^2}} \\
q &= t_3 + \frac{1}{2} Y \\
g_V &= T_3 - 2 q x_w \\
g_A &= T_3 \\
\frac{e}{\cos\theta_w} g'_V &= g_2 [(q'_L + q'_R) + 2 \frac{g_{12}}{g_{22}} (-t_3 + 2q)] \\
\frac{e}{\cos\theta_w} g'_A &= g_2 [(q'_L - q'_R) - 2 \frac{g_{12}}{g_{22}} t_3]
\end{aligned}$$

Hence, the extra neutral interaction is written in the current eigenstate gauge boson basis by adding an extra term for the new gauge boson similar to the Standard Model one. There are 4 independent, measurable parameters: $e, \sin\theta_w, g_2$ and $\frac{g_{12}}{g_{22}}$.

	T_3	$\frac{1}{2}Y$	q	q'	g_V	g_A	$\frac{g}{\cos\theta_w} g'_V$	$\frac{g}{\cos\theta_w} g'_A$
ν_L	$\frac{1}{2}$	$-\frac{1}{2}$	0	q'_{lL}	$\frac{1}{2}$	$\frac{1}{2}$	$g_2[q'_{lL} - \frac{g_{12}}{g_{22}}]$	$g_2[q'_{lL} - \frac{g_{12}}{g_{22}}]$
e_L	$-\frac{1}{2}$	$-\frac{1}{2}$	-1	q'_{lL}	$-\frac{1}{2} + 2x_w$	$-\frac{1}{2}$	$g_2[(q'_{lL} - q'_{eR}) - 3\frac{g_{12}}{g_{22}}]$	$g_2[(q'_{lL} + q'_{eR}) + \frac{g_{12}}{g_{22}}]$
e_R	0	1		q'_{eR}				
u_L	$\frac{1}{2}$	$\frac{1}{6}$	$\frac{2}{3}$	q'_{qL}	$\frac{1}{2} - \frac{4}{3}2x_w$	$\frac{1}{2}$	$g_2[(q'_{qL} - q'_{uR}) + \frac{5g_{12}}{3g_{22}}]$	$g_2[(q'_{qL} + q'_{uR}) - \frac{g_{12}}{g_{22}}]$
u_R	0	$-\frac{2}{3}$		q'_{uR}				
d_L	$-\frac{1}{2}$	$\frac{1}{6}$	$-\frac{1}{3}$	q'_{qL}	$-\frac{1}{2} + \frac{2}{3}2x_w$	$-\frac{1}{2}$	$g_2[(q'_{qL} - q'_{dR}) - \frac{g_{12}}{3g_{22}}]$	$g_2[(q'_{qL} + q'_{dR}) + \frac{g_{12}}{g_{22}}]$
d_R	0	$\frac{1}{3}$		q'_{dR}				

Table 4.5.: *T_3, Y, charges and couplings for ordinary fermions*

4.2.3. Popular models (particular cases)

⋆ A popular model is an effective $SU(2)_L \times U(1)_Y \times U(1)'_Y$ model, which originates from the breaking of the exceptional E_6 group [11], which is general enough to include many interesting possibilities. Indeed, in the breaking of this group down to the SM symmetry, two additional neutral gauge bosons could appear. For simplicity it is assumed that only the lightest Z' can be produced at LHC. It is defined as

$$Z' = \cos\beta Z'_\psi - \sin\beta Z'_\chi.$$

The general extra $U(1)$ depends on a mixing angle β, that fixes the combination of two extra independent $U(1)$'s arbitrarily chosen in E_6. Then the Z'_χ, Z'_ψ and Z'_η models correspond to $\beta = -\frac{\pi}{2}, 0, \arctan(-\sqrt{\frac{5}{3}}) - \frac{\pi}{2}$. In these cases is $g_{12} = 0$ and $g_{22} = g_{11}$. The q' charges are given in table 4.6.

- Z'_ψ model: E_6 breaks down to $SO(10)$ and $U(1)_\psi$
  $E_6 \to SO(10) \times U(1)_\psi$
- Z'_χ model: E_6 breaks down to $SO(10)$ and $SO(10)$ to $SU(5)$ and $U(1)_\chi$
  $E_6 \to SO(10) \times U(1)_\psi \to SU(5) \times U(1)_\chi \times U(1)_\psi$
- Z'_η model: E_6 breaks directly down to a rank 5 group
  $E_6 \to SU(3)_C \times SU(2)_L \times U(1)_Y \times U(1)_\eta = SM \times U(1)_\eta$

⋆ Other popular models are the left-right (LR) models [12], based on $SU(2)_R \times SU(2)_L \times U(1)_{B-L}$, where B and L are the baryon and lepton numbers. They are the simplest extended gauge groups which introduce charged currents interactions for the right-handed fermions. Here $SO(10)$ breaks down to $SU(2)_R \times SU(2)_L \times U(1)_{B-L}$:

$$SO(10) \to SU(3)_C \times SU(2)_L \times SU(2)_R \times U(1)_{B-L}.$$

They are parametrized by the ratio $\kappa = \frac{g_R}{g_L}$ of the gauge couplings from $SU(2)_{L,R}$. It is $q_{LR} = q_\chi$, $g_2 = \frac{e}{\cos\theta_w}\sqrt{\frac{2}{5}}\frac{\beta^2+1}{\beta}$ and $\frac{g_{12}}{g_{22}} = \frac{1}{2\sqrt{10}}\frac{3\beta^2-2}{\beta^2+1}$, with $\beta = \sqrt{\kappa^2 cot^2(\theta_w) - 1}$. We will assume $\kappa = 1$, this corresponds to manifest left-right symmetric gauge interactions.

⋆ For a complete comparison, we will also discuss the case of a sequential boson Z'_{SSM}, which has the same couplings to fermions as the SM Z boson.

q'	$2\sqrt{10}q_\chi$	$2\sqrt{6}q_\psi$	$2\sqrt{15}q_\eta$
q'_{qL}	-1	1	-2
q'_{uR}	-1	1	-2
q'_{dR}	3	1	1
q'_{lL}	3	1	1
q'_{eR}	-1	1	-2

Table 4.6.: q' *charges*

In table 4.7 all coupling constants of the 3 types of discussed models are shown.

4.2.4. Mixing effects between the new gauge bosons and the ordinary ones

In these extended electroweak models one must consider the possibility of mixing between the ordinary Z gauge boson and the new one(two). Such mixing can fortunately be neglected as the observed Z mass agrees strongly with the predictions from $SU(2) \times U(1)$ if the new gauge bosons are heavy, e.g. ≥ 1 TeV [13].

	ψ, χ, η	
	$\frac{g_V}{x_w}$	$\frac{g_A}{x_w}$
ν	$\frac{1}{6}\sqrt{\frac{5}{2}}\cos\beta - \frac{3}{2}\sqrt{\frac{1}{6}}\sin\beta$	$\frac{1}{6}\sqrt{\frac{5}{2}}\cos\beta - \frac{3}{2}\sqrt{\frac{1}{6}}\sin\beta$
e	$-\frac{2}{\sqrt{6}}\sin\beta$	$\frac{1}{3}\sqrt{\frac{5}{2}}\cos\beta - \sqrt{\frac{1}{6}}\sin\beta$
u	0	$\frac{1}{3}\sqrt{\frac{5}{2}}\cos\beta + \sqrt{\frac{1}{6}}\sin\beta$
d	$\frac{2}{\sqrt{6}}\sin\beta$	$\frac{1}{3}\sqrt{\frac{5}{2}}\cos\beta - \sqrt{\frac{1}{6}}\sin\beta$
	LR	
	$g_V\sqrt{\kappa^2-(1+\kappa^2)\cdot x_w}$	$g_A\sqrt{\kappa^2-(1+\kappa^2)\cdot x_w}$
ν	$\frac{1}{2}x_w$	$\frac{1}{2}x_w$
e	$\frac{3}{2}x_w - \frac{1}{2}(1-x_w)\kappa^2$	$\frac{1}{2}((1-x_w)\kappa^2 - x_w)$
u	$-\frac{5}{3}x_w + \frac{1}{2}(1-x_w)\kappa^2$	$-\frac{1}{2}((1-x_w)\kappa^2 - x_w)$
d	$\frac{1}{6}x_w - \frac{1}{2}(1-x_w)\kappa^2$	$\frac{1}{2}((1-x_w)\kappa^2 - x_w)$
	SSM	
	g_V	g_A
ν	$\frac{1}{2}$	$\frac{1}{2}$
e	$-\frac{1}{2} + 2x_w$	$-\frac{1}{2}$
u	$\frac{1}{2} - \frac{4}{3}x_w$	$\frac{1}{2}$
d	$-\frac{1}{2} + \frac{2}{3}x_w$	$-\frac{1}{2}$

Table 4.7.: *Coupling constants*

4.3. Extra Dimensions

From a modern physics point of view, a satisfactory answer to the question about extra dimensions can be found within the context of string theories or within a more unifiable framework, known as M theory [14]. The reason is that string theories provide the only known theoretical framework within which gravity can be quantifed and so plays a central role in our endeavors of unifying all fundamental forces of nature. A consistent quantum-mechanical formulation of a string theory, however, requires the existence of additional dimensions beyond the four ones we know. These new dimensions must be sufficiently small, in some appropriate sense, so as to have escaped our detection. Compactification, where additional dimensions are considered to be compact manifolds of a characteristic size R, provides a mechanism which can successfully hide them.
The hierarchy problem (disparity between the electroweak and the 4-dimensional Planck scales) can be avoided in the case of large extra dimensions.
In general there are the 3 known space-dimensions (the *brane*) and d extra dimensions orthogonal to the brane. So we live in $D = 3 + 1 + d$ dimensions, the *bulk*. Depending on the models, the extra dimensions can be large or small (TeV^{-1} range); matter, gauge bosons, gravitons and Higgs bosons can propagate either in the bulk or the brane. In the case where only gravitation propagates in the bulk, the SM remains with its usual behavior, only gravitation is modified, the extra dimensions must be compactified to avoid deviations from Newton's theory.
In any case, as the result of compactification, a field living in the bulk expands into a serie of Kaluza-Klein (KK) states (labeled by Kaluza Klein mode n), each KK-state appears as particle with mass $m(n)$ on the brane. Similar to a particle in a box, the momentum of the bulk field is quantified in the compactified dimension, from the 4d perspective of an observer on the brane, each allowed momentum in the compactified volume appears as a KK excitation of the bulk field. This builds a KK tower of states where each KK excitation carries identical spin and gauge quantum numbers. In appendix A as a simple example the KK modes of a 5 dimensional Abelian theory are presented in a more detailed way.

There are three principal scenarios ([15] and references therein and [16]):

- ⋆ **Large extra dimensions, ADD model**
  In a phenomenological approach, Arkani-Hamed, Dimopoulos and Dvali (ADD) propose to keep the fields of the SM in a 4 dimensional brane sitting in $4+d$ dimensional bulk with d compact extra

space like dimensions (radius R) containing the gravitation.
At distances small compared to R, the gravitational potential will simply change according to the Gauss law in $d+4$ dimensions, i.e.

$$V(r) \sim \frac{m_1 m_2}{M_G^{d+2}} \frac{1}{r^{d+1}},$$

where $r \ll R$ and M_G is the true gravitational scale to be distinguished from the Planck scale M_P. As the distance, at which gravity is probed, becomes much larger than R, the potential will again look effectively four dimensional, i.e.

$$V(r) \overset{r \gg R}{\to} \frac{m_1 m_2}{M_P^2} \frac{1}{r^1}.$$

We get $M_P^2 = M_G^{2+d} R^n$.
Hence, the weakness of gravity, observed by today's experiment, is not due to the enormity of the Planck scale M_P, but thanks to the presence of a large radius R. As a result, the true fundamental gravity scale M_G is much smaller than M_P. For a gravitational scale in the TeV range, one needs for example 2 extra dimensions of the order of 1 mm or 6 extra dimensions of the order of 10 fm. Even Cavendish-type experiments do not yet allow to observe deviations from Newton's law at this distances. However, only one extra dimension is excluded, as in this case we have $R \sim 10^{11}$ m - the dimension of the solar system where no deviations from Newton's law are found.
The bounds on the compactification radius from experimental data for the SM are much more severe (the SM is known up to 10^{-15} mm $(100\,\mathrm{GeV})^{-1}$) and so R has to be at least as small as an inverse TeV. The SM fields cannot not propagate in large extra dimensions.

⋆ **TeV sized extra dimensions**
TeV sized extra dimensions arise naturally in brane world theories. SM gauge bosons, gravitation, the Higgs boson and even fermions are allowed to propagate in the bulk, however they do not allow to reformulate the hierarchy problem.
Scenarios with TeV sized extra dimensions additionally to large extra dimensions offer interesting possibilities including a reformulation of the hierarchy problem: matter could be confined in the 3-brane, gravitation could propagate in the small and large extra dimensions as in the ADD model. The SM gauge fields could propagate also in the a number of additional small extra dimensions.

⋆ **Warped extra dimensions, RS model**
Randall and Sundrum (RS) propose another phenomenological model with one or two 4 dimensional branes sitting in a 5 dimensional bulk having a so-called anti-de-Sitter (or warped) geometry. The Standard Model fields are assumed to be constrained to one of these rigid branes. The 5 dimensional metric is given by

$$ds^2 = \exp^{-2k|y|} \eta_{\mu\nu} dx^\mu dx^\nu + dy^2.$$

The "warp" factor $\exp^{-2k|y|}$ in front of the 4 dimensional part of the metric allows to generate a low energy scale on one brane from a high energy scale on the other brane. In particular, a TeV scale can be generated from the 4 dimensional Planck scale for $kR \sim 12$ thus allowing another solution to the hierarchy problem. The 4 dimensional Planck scale in the RS approach is:

$$M_P^2 = \frac{M_5^3}{k} \left(1 - \exp^{-2kR\pi}\right).$$

The model used in the present study

In models with "large" extra dimensions, characterized by compactification radii $\gg 1/\mathrm{TeV}$, gravity propagates in the bulk, and the SM fields are confined to a 3-brane. The presence of the extra dimensions could be probed by searching for the Kaluza-Klein excitations of the gravitons. An interesting variation of these models assumes that only the fermions are confined in the 3-brane, whereas the gauge fields propagate also in a number of additional small extra dimensions orthogonal to the brane with compactification radius $\sim (1\,\mathrm{TeV})^{-1}$.
The model used here was motivated by the study in [17].
In this model one "small" extra dimension, compactified on S^1/Z_2 is considered, i.e. the extradimension

y is characterized by $y = 0 \to 2\pi R$ (S^1) and by $y \to -y$ (Z_2), the two fix points by this two symmetries $y = 0$ and $y = \pi$ are the orbifold points. All SM fermions are on the same orbifold point (D=0), gravity and the gauge bosons are propagating in the bulk.
The main signature is the appearance of a tower of KK resonances for each of the gauge fields propagating in the bulk. This resonances could be produced at future high energy colliders and detected through their decay to SM fermions. The model is completely specified by a single parameter M_C, the compactification scale. The masses M_n of the KK modes are given by the relation $M_n^2 = (nM_C)^2 + M_0^2$, where M_0 is the mass of the zero-mode excitation corresponding to the Standard Model gauge boson. The couplings of the Z boson and the γ are the same as the corresponding SM couplings, scaled by a factor $\sqrt{2}$.
For the case of more than one small extra dimension the situation is far more complex and depends upon the details of the compactifying manifold. Here we find that not only the KK excitation spacings are more intricate but many of the levels become degenerate.
Even with only one small extra dimension the excitations of the γ, the Z and the W bosons are nearly degenerated in mass.

4.4. Other models

Many other theories beyond the SM predict new vector bosons:

- ⋆ alternative left-right symmetric models ($ALRM$) [18],
- ⋆ the Un-unified Standard Model ($UNSM$) [18, 19],
- ⋆ the Foot-Hernandez model [20],
- ⋆ the model of Kuo [20],
- ⋆ the BESS model [21],
- ⋆ the little Higgs model [22],
- ⋆ warped Higgsless models [23],
- ⋆ several extra dimension scenarios [17]
- ⋆ ...

We shall not study them.

4.5. Conclusions

Although the Standard Model of the electroweak and strong interactions, that was discussed with its mathematical formalism in the first part of the chapter, describes nearly all experimental data available today, it is widely believed that it is not the ultimate theory. In many theories beyond the SM new vector bosons appear, in this work among others E_6 and LR models are chosen. In these models the heavy extra gauge bosons are characterized by their different couplings to the leptons but they behave otherwise as the usual Z boson. The SSM case will be studied as well: an extra gauge boson that is identical to the usual Z boson, except its mass.
Finally, one of the various extra dimension models is studied (motivated by [17]), where extra gauge bosons appear as a tower of gauge bosons: the case of one small extra dimension where the gauge bosons propagate with the graviton in the bulk, only matter is confined on the brane.
Their theoretical background was discussed and their characteristics (couplings to the SM particles) were shown. These are the ingredients for simulations. Their different decay properties will be presented and studied in the following chapters.

5. The LHC accelerator and the ATLAS experiment

This chapter describes the LHC and the ATLAS experiment. A description of the LHC machine and the reasons for its concepts will be given. An overview of the general purpose ATLAS detector will follow explaining the purpose of its different subdetectors and mentioning the challenges that the general purpose detectors will face.

5.1. The Large Hadron Collider

The Large Hadron Collider LHC is the next generation of colliders (hadron-hadron collider) being built at CERN, the European particle physics laboratory (Centre Européen pour la Recherche Nucléaire). It will succeed the Large Electron Positron Collider LEP and use its 27 km circular tunnel. The LHC is primarily a *pp* collider, however it can also be used as a heavy ion collider. First collisions are expected for 2007.
The LHC will be fed by existing particle sources and pre-accelerators. All of CERN's proton machines play a role in the injection scheme of LHC.

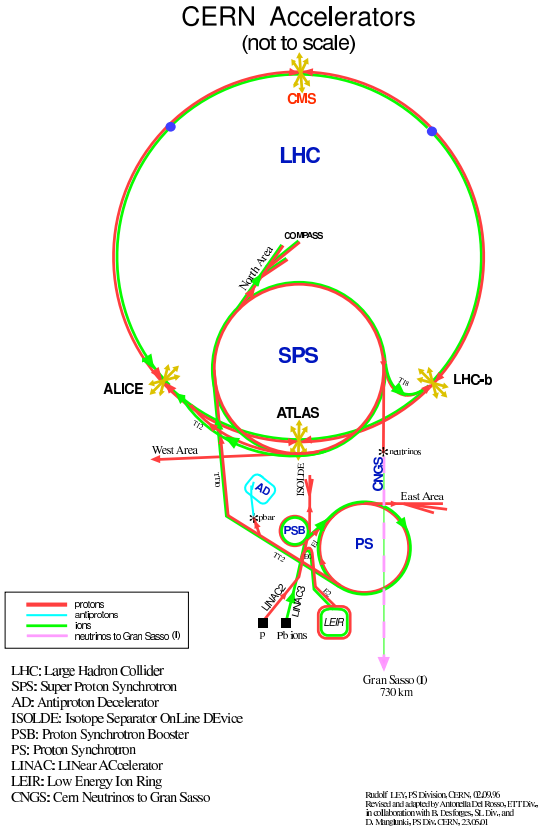

Figure 5.1.: *The* LHC *machine*

Figure 5.1 shows their relation in the complete acceleration chain. The protons are produced and accelerated to 52 MeV by the Proton Linac, before being injected into the 1.4 GeV Proton Synchrotron (PS) booster (PSB). The PS itself will accelerate the protons to 26 GeV and finally the Super Proton Synchrotron (SPS) will inject protons at 450 GeV into the LHC. The LHC will subsequently accelerate these up to 7 TeV per beam collision energy. The so-called beams are a succession of proton bunches.
In order to collide two beams of equally charged particles they must circulate in separate and opposite magnetic fields. In the LEP tunnel there is hardly room for two separate magnets. A solution to

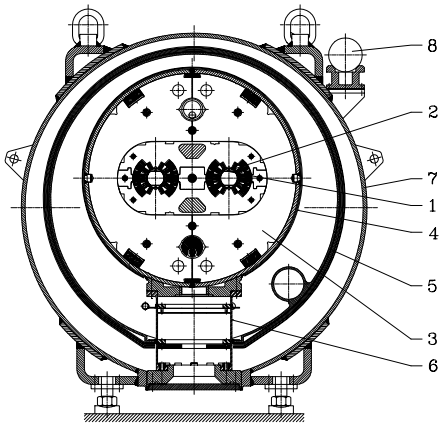

Figure 5.2.: *Cross-section of the* LHC *dipole magnet and cryostat*

this problem was found using a twin-aperture magnet with to coils and beam channels using the same mechanical structure and cryostat, figure 5.2.
The two beam channels lie side by side in the cold yokes of the main dipole and quadrupole magnets. This twin-aperture arrangement has enabled a cost saving of 30 % compared to two separate magnets as well as solving the obvious space problem.
In order to accelerate the proton beams to the required energy and to bend the beam around the LEP tunnel (a parameter that cannot be increased to produce gentler curves) the magnetic fields need to be of 8.36 T. However for an adequate safety margin the magnets require a quench field of at least 9 T. This high magnetic field can only be produced with superconducting magnets. However this alone is not enough. Superconducting magnets have to bee cooled to very low temperature (a few Kelvin) in order for the superconducting properties to be present. The LHC magnets will need to be cooled with super-fluid Helium at 1.9 K.
To keep the super-fluid Helium cooling the magnets at the required 1.9 K, there is a need for a cryogenics plant with a total cooling power of 144 kW equivalent capacity at 4.5 K. This will be provided by eight cryoplants of 18 kW each.
At the LHC, there will be a total of 3444 superconducting magnet units. These include 1232 main dipole magnets and 386 main quadrupole magnets of twin-aperture design. To these will be added 4928 small correctors to the main dipoles bringing the total to about 8400 units of different sizes and importance. In addition to these superconducting magnets there will be a number of room temperature magnets.

Parameter		*pp* (at high luminosity)
Beam Energy	TeV	7
Center-of-mass energy	TeV	14
Time between collisions	ns	24.95
Injection energy	GeV	450
Dipole field	T	8.36
Dipole magnet temperature	K	1.9
Number of bunches per ring		2835
Particles per bunch		10^{11}
Bunch length	cm	7.5
Bunch width	μm	15.9
Beam current	mA	530
Luminosity	$cm^{-2}s^{-1}$	10^{34}
Circumference	km	26.659
Cost to completion (approx.)	million CHF	3080

Table 5.1.: *Main Machine Parameters*

The LEP tunnel imparts to the LHC an eight fold symmetry and consequently eight potential interaction points around the ring. As it can be seen from figure 5.3 these are not all used for experiments. The beams will cross in four points where the physics experiments will be situated. In the other four octants the beams will not cross and the sections will be used for machine utilities such as acceleration, beam cleaning and beam dumping systems. Point 4, that contains beam acceleration systems, is designed to allow another experiment to be installed there in the future.

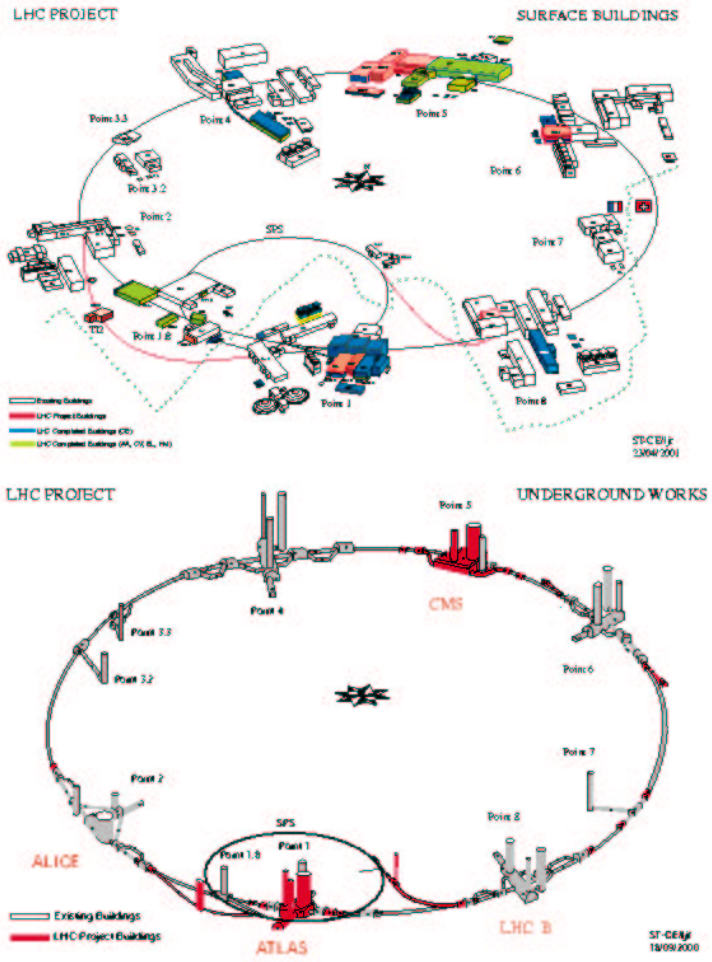

Figure 5.3.: *The* LHC *above and below ground (from [24])*

The four experiments can be divided into three categories; the two general purpose proton-proton experiments, ATLAS and CMS, which will be located in new underground caves at point 1 and 5 respectively; the heavy ion experiment ALICE located at point 2 in an existing cave; and the LHCb experiment devoted to B-physics at point 8.
The main machine parameters for the pp collisions are presented in table 5.1. As a pp collider, the beam energy of 7 TeV is giving a total center of mass energy of 14 TeV with a initial luminosity of $2 \times 10^{33} cm^{-2} s^{-1}$ ("low luminosity") and a bunch spacing of 25 ns. In a second time after prospectively 3 years the luminosity will be increased by a factor 5 ("high luminosity"). Then in one year an integrated luminosity of $100\,\mathrm{fb}^{-1}$ should be collected.
The LHC has the potential to greatly advance our understanding of fundamental physics and to constrain the theories which can describe it. Its high energy and luminosity allow exploration of a variety of important questions, such as the origin of mass, the predominance of matter over anti-matter, and the relationship of matter to the forces that act on it.
In particular the increase of energy and intensity relative to previous pp and $p\bar{p}$ colliders is shown in figure 5.4.
High energy allows the production of heavier particles - for a collider experiment the energy available to

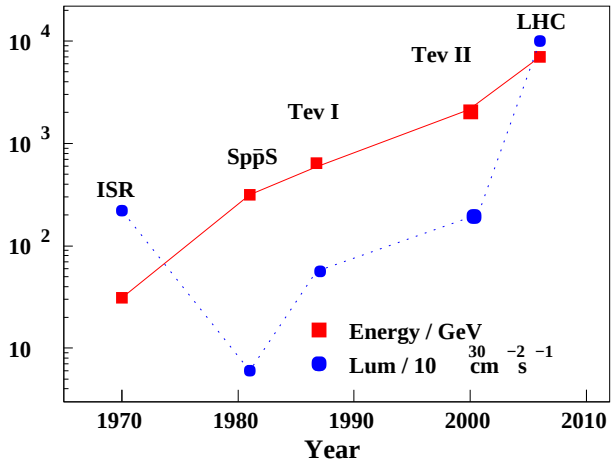

Figure 5.4.: *The energy and luminosity of the various proton-(anti-)proton colliders plotted against their start-up year (from [24])*

produce new particles increases with the beam energy. The luminosity gives a measure of the intensity of the beams, and is proportional to the total number of interactions of a specific type which might be expected.

5.2. Physics Goals

In common with many particles physics experiments, ATLAS would be better described as an experimental facility. A wide-ranging physics program includes new physics, but also studies of the Standard Model (SM).

- **Higgs:** the exploration of the mechanism of electroweak symmetry breaking, incorporating various Higgs boson searches. The Higgs boson is the only particle of the SM which has not yet been observed. Extensions to the SM such as supersymmetry often extend the Higgs sector, and so predict multiple Higgs bosons.
- **Electroweak theory:** the precision measurement of the top-quark and the W boson masses as well as the electroweak gauge boson couplings; B- physics. If discovered, deviations from the SM could give hints for new physics or exclude models beyond the SM.
- **New physics:** searches for supersymmetry, for large and small extra dimensions, searches for leptoquarks, searches for a substructure of quarks/leptons,... New particles, e.g. new extra gauge bosons, are predicted in several models at about the TeV scale, which if they exist should be observable at the LHC.
- ...

5.3. The ATLAS detector

The ATLAS (A Toroidal LHC ApparatuS) detector has been designed to exploit the full potential of the LHC. As such, the quest for the origin of the spontaneous symmetry-breaking mechanism in the electroweak sector of the SM is a major importance to ATLAS. The search for the Higgs boson (a possible manifestation of symmetry breaking) or the family of Higgs (in some models there is not only one Higgs boson predicted) is therefore a first benchmark for detector optimization.
The design of the ATLAS detector was described in the Letter of Intent LoI [25], in more detail in the Technical Proposal [26], and in even greater details in the individual sub detector Technical Design Reports (TDRs).
In the section 5.3.2 (and following) the sub-systems of ATLAS, the Muon spectrometer, the electromagnetic and hadronic calorimeter, the inner detector and the trigger system, will be described.

The basic design considerations for ATLAS are motivated by the physics at the LHC during the initial low luminosity stage and later during the high luminosity running.
They can be summarized as follows:

- ⋆ very good electromagnetic calorimetry for electron, γ identification and measurement, with a hermetic jet and missing energy calorimetry;
- ⋆ efficient tracking, first at high luminosity for lepton momentum measurements and secondly at low luminosity for b-quark tagging, enhanced electron and photon identification, as well as tau and heavy lepton flavor vertexing and reconstruction capability of some B decay final states;
- ⋆ stand alone precision muon momentum measurement up to the highest luminosity and very low p_T trigger capability at low luminosity;
- ⋆ high spatial acceptance in η [1];
- ⋆ capacity to measure particles of low p_T.

To maximize the physics reach it is necessary to have a large acceptance in the pseudorapidity[1] and to be able to trigger and measure particles at low p_T thresholds.
The objectives of performance for the ATLAS detector are shown in table 5.2.

Detector component	Characteristics and Resolution	covered η region
EM calorimeter	$10\%/\sqrt{E}\oplus\ 0.7\%$	$\pm$ 3.0
Preshower detection	Enhanced $\gamma-\pi^0$, γ-jet separation direction measurements, and b tagging with electrons	$\pm$ 2.4
Calorimetry for Jets and missing E_T Calorimetry		
Barrel and end-cap	$50\%/\sqrt{E}\oplus\ 3\%$	$\pm$ 3.0
Forward region	$50\%/\sqrt{E}\oplus\ 3\%$	$3<\eta<5$
Inner detector	30% at $p_T = 500\,\mathrm{GeV}$	$\pm$ 2.5
	Enhanced electron identification,	$\pm$ 2.5
	b- and τ-tagging,	$\pm$ 2.5
	secondary vertex detection at low luminosity	$\pm$ 2.5
Muon detection	10% at $p_T = 1\,\mathrm{TeV}$ in stand-alone mode at highest luminosity	$\pm$ 3

Table 5.2.: *Objectives of performance [26]*

The overall detector layout is shown in figure 5.5.
The detector geometry is based on the magnet configuration. It consists of an inner superconducting solenoid (with a field of 2 T) around the inner detector, and large superconducting air-core toroids arranged with an eight fold symmetry outside the calorimetry. This arrangement offers very few constraints on the inner detector and calorimetry systems and offers a high resolution, large acceptance and robust stand alone muon spectrometer.
Being the largest subdetector, the muon spectrometer defines the overall dimensions of the detector. This gives the detector a radius of $\sim$ 11 m and a length of $\sim$ 42 m (including the third layer of the forward muon chambers mounted on the cavern wall) and a weight of 7000 tons. This is considerably larger than current experiments/detectors at CERN or indeed anywhere in the world.

[1] For the definition of the pseudorapidity η see section 5.3.1.

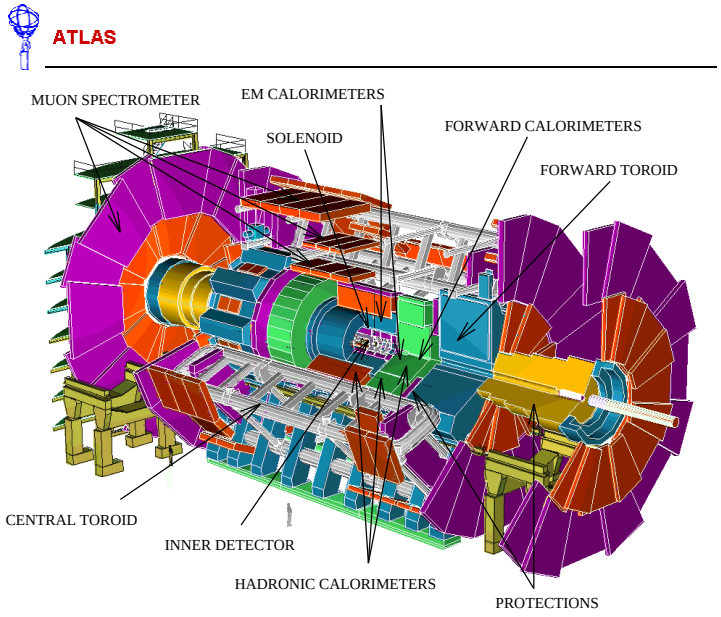

Figure 5.5.: *The* ATLAS *detector*

5.3.1. Detector geometry and terminology

The ATLAS detector has approximate cylindrical symmetry. It is most often described with a coordinate system $\{R,\phi,z\}$ or $\{R,\phi,\theta\}$, where the z-axis points parallel to the beam-pipe, R is the transverse distance from it and the azimuthal angle ϕ is defined such that the x-axis points from the interactions point to the center of the LHC ring. θ is the angle between the beam direction and the direction of the particle. The choice of the variables used is however R, ϕ and the pseudorapidity η as cross-sections in inelastic pp collisions are uniformly distributed in η, but not in θ.
The true rapidity $y = \frac{1}{2}\ln\left[(E+p_z)/(E-p_z)\right]$ of a Lorentz vector is defined such that the rapidity differences are conserved under a boost along the z-axis. However, the calculation of the true rapidity requires knowledge of the particle's mass, which is often difficult to determine experimentally. Hence the pseudorapidity $\eta = -\ln(\tan\theta/2)$ is defined in terms of the polar angle θ. This is a good approximation to the true rapidity in the relativistic limit. A highly relativistic particle 3-momentum vector is often described in ATLAS in terms of the three parameters p_T, ϕ and η, as in hadron colliders the initial z-momenta of the primary partons are not known.
The transverse momentum p_T and energy E_T are defined by $p_T = \sqrt{p_x^2 + p_y^2}$ and $E_T = \frac{E}{\cosh\eta}$, this quantities are conserved by a Lorentz boost along the z-axis.
Some particles, such as neutrinos, have a vanishingly small probability of interacting with the detector[2]. The presence of such "invisible" particles can be inferred from an apparent non-conservation of momentum in the transverse plane of observed particles. To achieve this, the experiment must completely surround the interaction point, so that particles cannot be lost. Electrical, optical and cryogenic services for central subdetectors of the experiment are therefore routed through the outer layers so that they do not create gaps. Two unavoidable gaps are created by the beam-pipes so final state particles in these directions inevitably go undetected. This is one of the reasons for restricting our interest to the missing transverse momentum $\not{p}_T$. The main motivation is however the fact that only the total transverse energy is known and only the total transverse momentum is conserved.
The central part is known as "barrel", completed by the two endcaps to ensure the covering of the whole solid angle around the interaction point.

[2] For example for a muon neutrino the charged interaction probability is of the order of 10^{-12} per GeV.

5.3.2. Inner detector

A three-dimensional view of the inner detector is shown in figure 5.6 and a cross-section in figure 5.7.

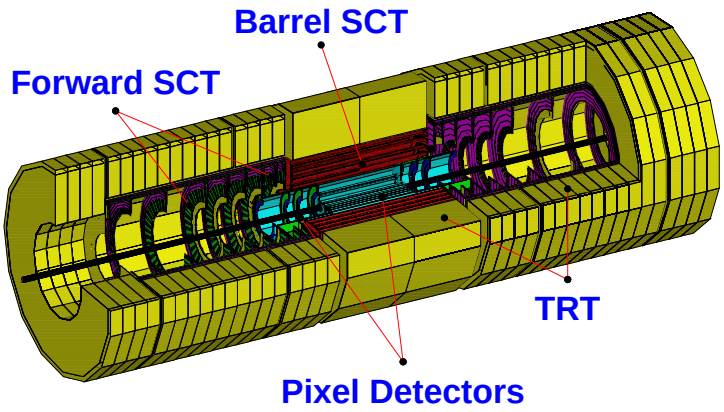

Figure 5.6.: *The inner detector*

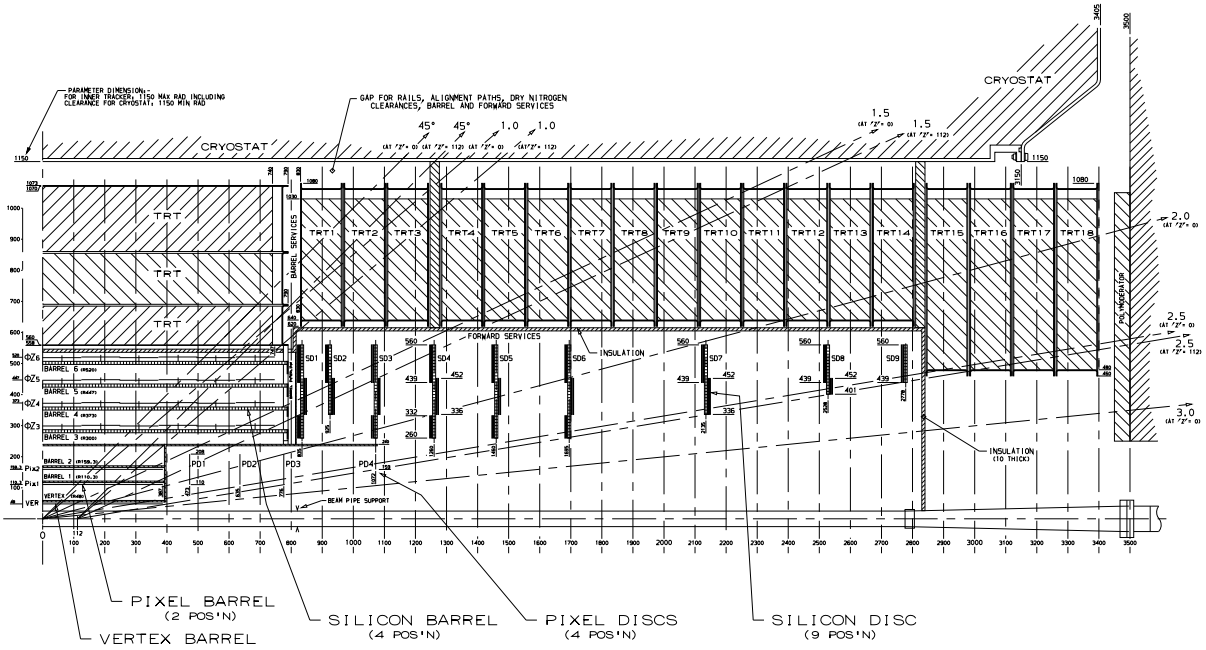

Figure 5.7.: *A cross-section of the ID layout through the beam axis*

The inner detector has to ensure track reconstruction of charged particles, measurements of their momentum and primary vertex and it participates in the electron identification. At low luminosity in addition secondary vertices for particles like the beauty or charmed mesons or the τ are measured.
The momentum and vertex resolution targets require high precision measurements to be made by fine granularity detectors because of the high track density that is expected at the LHC machine.
Semiconductor tracking (SCT) detectors offer the needed performance. Very close to the interaction point, where the highest granularity is needed, semiconductor pixel detectors will be used. Due to the significant amount of material that these precision layers introduce (and because of their cost), their number must be limited. Hence, in the final design, there will be seven layers (four strip and three pixel layers) crossed by each track. To obtain a large number of tracking points required for the pattern recognition, a straw tube tracker is used at higher radii. This offers the possibility of continuous track following with much less material per channel and lower cost. These two techniques offer very good pattern recognition with high precision ϕ and z measurements.
So, the particles cross (starting from the collision point) 3 concentric layers:

- ⋆ the pixel detector (high granularity silicon detectors),
- ⋆ the semiconductor SCT (silicon microstrip technology),
- ⋆ the transition radiation tracker TRT (a straw tube tracker with electron identification capability).

The inner detector, of cylindrical shape, is contained inside the super conducting solenoid magnet producing a field of 2 T at its center. It is 7 m long and has a radius of 115 cm. The detector is divided into three parts, a barrel part (±80 cm) and two endcaps. This layout provides full tracking over the pseudorapidity range $|\eta| \leq 2.5$.

Pixel Detector

The pixel detector will provide precision measurements over the full pseudorapidity range. This is crucial for impact parameter resolution. The drawback of pixel detectors is the complex readout electronics needed for each pixel. The readout chips in the final design are bonded to the substrate to achieve the required density of connections (each pixel has its own associated electronics and buffer). The pixel detector has 140 million pixels, each 50 μm in the $R\phi$ direction and 300 μm in the z direction. The inner layer, also called the vertex or B-layer, was originally intended for the low luminosity phase only, however there are plans to replace it in the high luminosity phase regularly because of radiation damage. For financial reasons, the second pixel-layer will be inserted later. In the barrel the high precision layers are arranged on concentric cylinders around the beam axis, whereas the endcap detectors are mounted on disks perpendicular to the beam axis. The spatial resolution is 12 μm in $R\phi$ and 66 μm in z.

Semiconductor Tracker

The SCT barrel uses silicon microstrip detectors to provide precision points in the $R\phi$ and z coordinates, using a small stereo angle (40 mrad) to obtain the z measurement. In the forward region, the modules use tapered strips, one set aligned radially, the stereo angle of the second set yielding the R coordinate. In the barrel the wafers measure $6.4 \times 6.4\,\mathrm{cm}^2$. Two such wafers are wire bonded end to end to form a 12.8 cm long module. Each wafer has 768 strips with 80 μm pitch. Two modules are glued back to back at a slight angle, the stereo angle. In the barrel the cylinders are positioned at radii of 300, 373, 447, 520 mm and in the forward region, there are three rings made up of nine wheels covering the required pseudorapidity range. The spatial resolution of the detector is 10 μm in $R\phi$ and 580 μm in z.

Transition Radiation Detector

The TRT uses straw tube detectors, surrounded by radiator material (foil and foam). This enables electron identification from the detection of transition-radiation photons created by the electron passing through the radiator.
Each straw is a 4 mm diameter aluminum tube with a maximum length of 150 cm. They are arranged in concentric layers in the barrel giving an average of 36 hits on each track. There are 50 000 axial straws in the barrel divided in two halves and read out at both ends. The endcap contains 320 000 radial straws with readout at the outer radius. A total of 420 000 electronic channels provide a drift time measurement giving a spatial resolution of 170 μm per straw at two independent thresholds. The lower threshold is for tracking hits and the higher one is for transition radiation hits.
The barrel section is built from three cylinders covering the range 56 to 107 cm. The two endcaps have 18 wheels, the first 14 nearest the interaction point cover a radius of 64 to 104 cm and the last four wheels extend down to a radius of 48 cm. The TRT has been designed to deal with high occupancy and high counting rates. As mentioned previously the spatial resolution of individual straws is 170 μm, but a measurement accuracy of 50 μm is achieved when averaged over all straws in the LHC design luminosity. The performance of the inner detector is well characterized by the resolution of the impact parameter of tracks from secondary vertices d_0. This is parametrized in $R\phi$ as $\sigma(d_0) = 11 \oplus 60/p_T\sqrt{\sin\theta}$ and in z as $\sigma(d_0) = 70 \oplus 100/p_T\sqrt{\sin^3\theta}$ (in μm) with the dedicates B-physics layer of pixels present at 4 cm radius.

5.3.3. Calorimetry

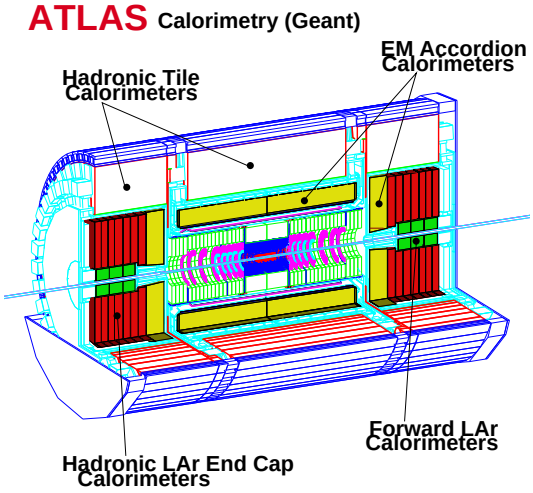

Figure 5.8.: *Three-dimensional view of the* ATLAS *calorimetry (from* GEANT*)*

The goals of the calorimetry are precise measurements of energy and position of electrons and photons (the electromagnetic part), the measurement of energy and direction (hadronic part) and the missing transverse energy. It participates in separating electrons, photons versus hadrons, jets at the electron identification and contributes to the trigger system.
The layout of the calorimetry is shown in figure 5.8. It consists of three sections: the electromagnetic (EM) calorimeter (Liquid Argon, LAr), the hadronic calorimeter (combination of scintillating tiles and LAr) and the forward calorimeter (EM and hadronic LAr), where the electromagnetic and hadronic calorimeter can be subdivided into barrel and endcap. There is a gap between the barrel and endcap section at $|\eta| \sim 1.3 - 1.5$ for the cryostat and inner detector services.
There are three cryostats, barrel and two endcaps. The barrel cryostat around the inner detector contains the inner detector superconducting solenoid, the LAr presampling layer and the electromagnetic LAr accordion calorimeter. The endcap cryostats enclose the electromagnetic LAr accordion calorimeter, the hadronic endcap LAr calorimeter and the forward LAr calorimeter. The hadronic tile calorimeter is located outside the cryostats.

Presampler
In the central part, the electromagnetic calorimeter is preceded radially by a presampler to correct for the energy lost in front of the calorimeter (inner detector, cryostat and the solenoid) to maintain excellent energy and position resolution. In the barrel (end-cap) there is a 1 cm (5 mm) liquid argon active layer with electrodes perpendicular (parallel) to the beam axis. The high granularity (see table 5.3) allows a good measurement of the polar angle of the photons.

Electromagnetic calorimeter
The sampling electromagnetic calorimeter measures positions and energy of photons and electrons by probing the electromagnetic shower produced in the detector: absorbing layers (dense material where the shower develops) alternating with detecting layers (ionization by the particles). Liquid Argon is used as the detecting layer, lead as absorber. The liquid Argon has the advantage to be homogeneous in the whole detector and to resist to the important radiation fluxes.
A read-out electrode is inserted parallel to the absorbers between each two of them. It receives the electric signal created by influence by the drift of ionization electrons in an uniform electric field perpendicular to the absorber-electrode plane. The typical drift time is about 600 ns.
The accordion structure (see figure 5.9) of electrodes and absorbers allows a total azimuthal (ϕ) coverage at the same time as a constant distance between electrodes and absorbers (2 mm).

presampler	barrel	endcaps	
coverage	$\|\eta\| < 1.52$		$\|\eta\| < 1.52$
longitudinal segmentation	1 layer	1 layer	
granularity $\Delta\eta \times \Delta\phi$	0.025×0.1	0.025×0.1	
ECAL LAr	barrel	endcaps	
coverage	$\|\eta\| < 1.475$		$1.375 \quad \|\eta\| < 3.2$
longitudinal segmentation	3 layers	3 layers	$1.5 \quad \|\eta\| < 2.5$
		2 layers	$1.375 \quad \|\eta\| < 1.5$
		2 layers	$2.5 \quad \|\eta\| < 3.2$
granularity $\Delta\eta \times \Delta\phi$			
layer 1	0.003×0.1	0.025×0.1	$1.375 \quad \|\eta\| < 1.5$
		0.003×0.1	$1.5 \quad \|\eta\| < 1.8$
		0.004×0.1	$1.8 \quad \|\eta\| < 2.0$
		0.006×0.1	$2.0 \quad \|\eta\| < 2.5$
		0.1×0.1	$2.5 \quad \|\eta\| < 3.2$
layer 2	0.025×0.025	0.025×0.025	$1.375 \quad \|\eta\| < 2.5$
		0.1×0.1	$2.5 \quad \|\eta\| < 3.2$
layer 3	0.05×0.025	0.05×0.025	$1.5 \quad \|\eta\| < 2.5$

Table 5.3.: *Granularity for LAr calorimetry*

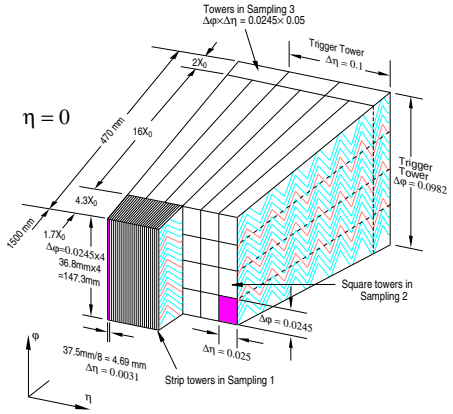

Figure 5.9.: *Readout granularity of the EM calorimeter*

The barrel ECAL covers the pseudorapidity range $|\eta| < 1.4$. The two end-caps consist of two concentric wheels covering the pseudorapidity region $1.4 < |\eta| < 2.5$ and $2.5 < |\eta| < 3.2$.

For $|\eta| < 2.5$ the electrodes are segmented radially in 3 layers to achieve high precisions, see figure 5.10. The first very short (6 radiation length X_0) layer, the so called "strips", that is closest to the beam axis has a very high granularity in η to achieve a high precision for the position η and the shower shape. This is important to discriminate between a shower produced by one photon and two very close photons that come from a π^0 decay.
The next layer ("middle") with a length of $16\,X_0$ decreasing with η, contains most of the shower: measurement of its energy and a second point to determine the flying direction. The granularity in η is 8 times less important than in the "strips". In the same time granularity is improving in ϕ direction.
The last layer ("back") contains parts of very energetic showers. The first two layers are sufficient to measure with precision showers with a transverse energy less than 50 GeV. The length of this last layer varies from 2 to $12\,X_0$, its granularity in η is 2 times lower than in the second layer.
The lateral segmentation of the electrodes in η is pointing to the center of the detector. A particle coming from the center crosses only one segmentation of each layer. The different granularities are given in table 5.3.

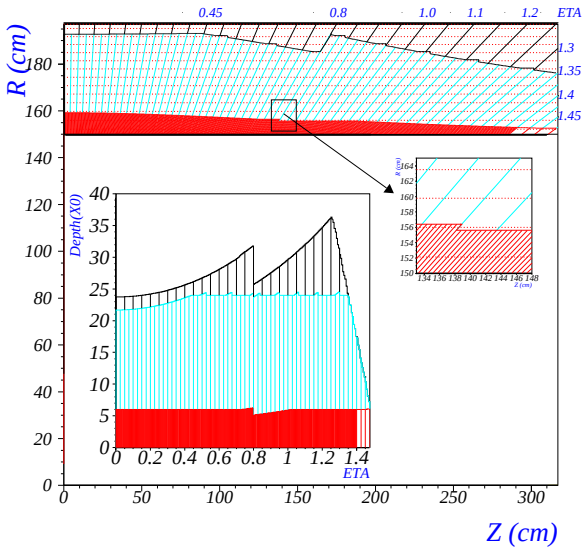

Figure 5.10.: *Segmentation of the barrel EM calorimeter. The bottom plot shows the thickness (in radiation length) up to the end of the three samplings (upstream material included).*

A cell is defined as the region of 4 electrodes in ϕ and one segmentation in η in the second layer, e.g. $\Delta\eta \times \Delta\phi = 0.025 \times 0.025$, this represents a surface of $4 \times 4\,cm^2$ at $\eta = 0$.
The electric signals are led to the radial extremities and summed in cells. This configuration avoids dead zones in ϕ due to instrumentation.

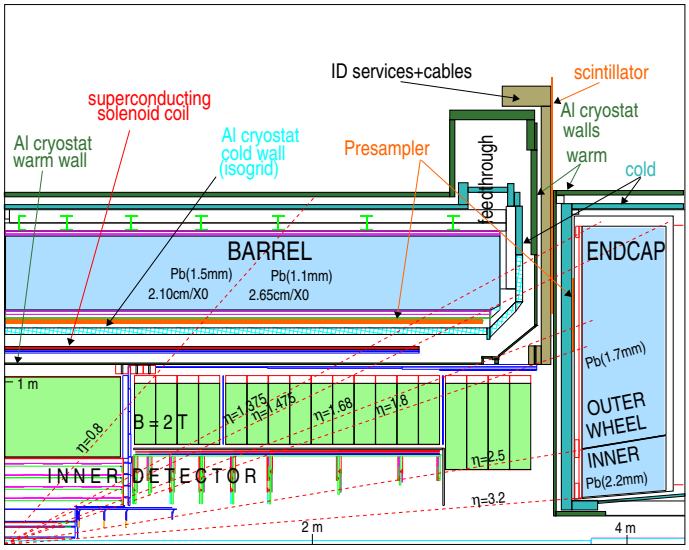

Figure 5.11.: *Longitudinal view of a quadrant of the EM calorimeter*

In the region $1.37 < |\eta| < 1.52$, the so-called crack, the energy measurement is declined. The effective depth of the barrel decreases from $|\eta| = 1.37$ on (see figure 5.11), the material (electronics and cryostats) in front of the EM calorimeter crosses up to $7\,X_0$, see figure 5.12. The showers start long before the end-caps and so can not be measured precisely.

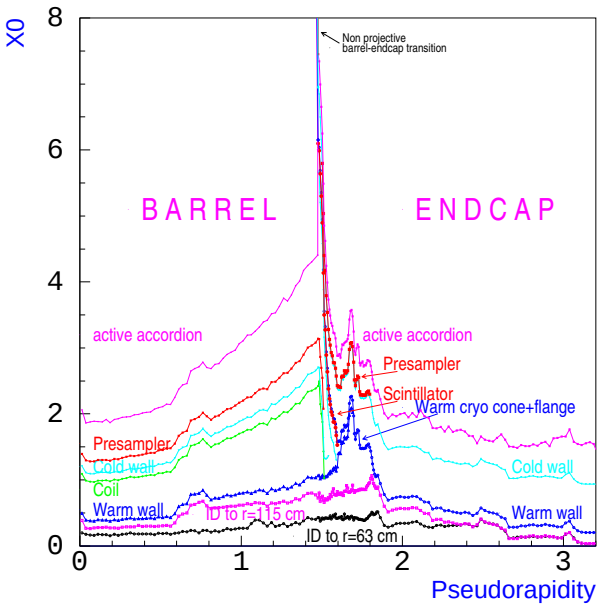

Figure 5.12.: *Breakdown of the material distribution in front of the EM calorimeter, over the full rapidity range*

Performance expected:
The energy resolution is given by

$$\frac{\sigma_E}{E} = \frac{a}{\sqrt{E}} \oplus \frac{b}{E} \oplus c,$$

where

- a is the sampling term that takes into account fluctuations on the number of primary processes detected
- b is the term for pile-up and the non-physics background, dominated by the electronic one
- c is a constant term, that is dominating at high energy and is over all due to the non-uniformity of the calorimetry, to leaks and dead matter before the calorimetry

The resolutions are given in table 5.4.

Calorimetry	a(%)	b(%)	c(%)
ECAL	10	< 0.5	0.7
HCAL	50	3.0	3.0

Table 5.4.: *Resolution for ECAL and HCAL*

The resolution in ϕ is $\sigma_\phi \sim 10\,mm/\sqrt{E(GeV)}$, in θ the goal is fixed to $\sigma_\theta \sim 70\,mm/\sqrt{E(GeV)}$.

Hadronic calorimeter
The principle of the Hadronic Calorimeter (HCAL) is shown in figure 5.13.
It is supposed to identify and measure jets and muons with low transverse momentum. It covers the region in pseudorapidity up to 5 and is composed of different techniques to respond to the different requests. Iron tile calorimetry is used up to $|\eta| \leq 1.7$ and below LAr is imposed in the so called forward calorimetry and the end-caps by the high radiation fluxes.
The hadronic tile calorimeter consists of a barrel and two extended barrel cylindrical parts. Each cylinder is built of 64 wedges along the azimuthal direction. The absorber material is steel and the scintillating tiles, read out by wavelength shifting fibers, are the active medium. The tiles lie in the $R\phi$ plane and have the width of one wedge. The fibers go to the supporting girder in which the electronic readout is

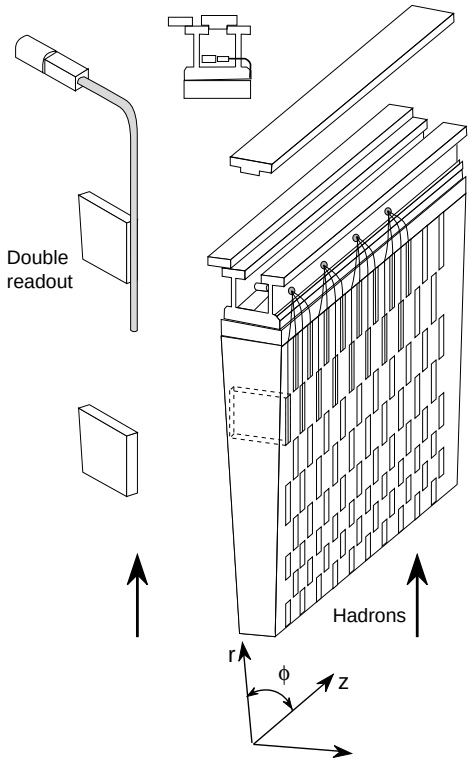

Figure 5.13.: *The principle of the Tile calorimeter design*

housed. The scintillating tile calorimeter has a pseudorapidity coverage of $|\eta| < 1.7$ with a granularity in $\Delta\phi \times \Delta\eta$ of 0.1×0.1.
The hadronic endcaps are LAr units using copper plates as the absorber medium. This reduces the capacitance of each cell and hence the electronic noise. The endcap consists of two wheels. The first has 25 mm copper plates and the second 50 mm copper plates. A gap of 8.5 mm exists between the copper plates, equipped with three parallel electrodes, the central one being the readout electrode. The pseudorapidity of the hadronic endcaps is $1.5 < |\eta| < 3.1$ with a granularity $\Delta\phi \times \Delta\eta$ of 0.1×0.1 up to $|\eta| = 2.5$ and then 0.2×0.2.
The forward calorimeter is very challenging due to the high level of radiation. To minimize the reflected neutron flux from the calorimeter face into the inner detector (highest and high η), the forward calorimeter is recessed by 1.2 m with respect to the EM calorimeter front face. In order to incorporate 9.5 active interaction length λ_I in the limited space, a high density calorimeter is required. The forward calorimeter consists of three sections, the first being made of copper, the other two of tungsten. All three sections consist of a metal matrix with regularly spaced longitudinal channels filled with concentric rods and tubes. Liquid argon is the sensitive medium flowing between the rods and the matrix. The pseudorapidity coverage of the three layers starts respectively at $\eta = 3.0$, $\eta = 3.1$ and $\eta = 3.2$, all finishes at $\eta = 4.8 - 4.9$. The energy resolution is given in the same form as for the ECAL, see table 5.4.

5.3.4. Muon Spectrometer

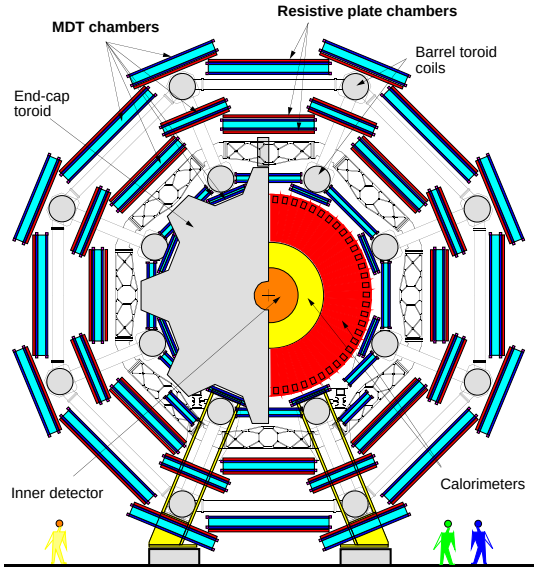

Figure 5.14.: *Transverse view of the spectrometer*

With no strong interactions and a relatively large mass, muons lose energy primarily by ionization. They can therefore pass through the calorimeters to dedicated detectors which can identify the particle and measure its momentum. The latter becomes especially important at higher energies ($\gtrsim 100\,\mathrm{GeV}$) where the relatively small size of the inner detector limits its accuracy in making momentum measurements.
The magnetic field in the muon detector is provided by superconducting air core toroids. For good track momentum resolution, a large magnetic field is desirable over long distances, so the overall scale of the magnet system is large - 20 m in diameter and 26 m long, and the average magnetic field strength is 0.6 T. The toroidal geometry keeps the magnetic field direction largely perpendicular to the muon trajectory.
In the barrel there are three layers (stations), one at the inner and outer edges of the toroids and one in the mid-plane. In the forward region, the chambers are positioned on either side of the endcap cryostat and a third layer on the cavern wall, see figure 5.14 and 5.15.

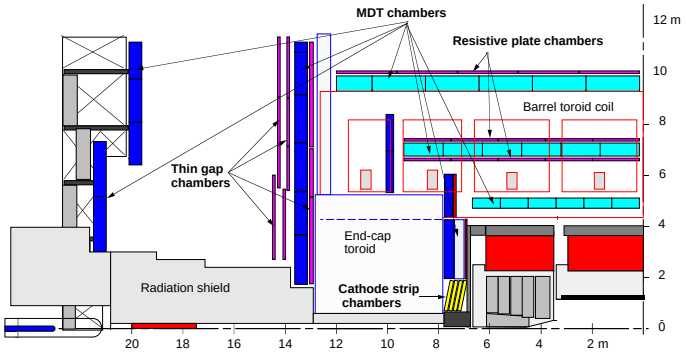

Figure 5.15.: *Side view of one quadrant of the muon spectrometer*

The barrel chambers cover the pseudorapidity range $|\eta| < 1$ while the endcap chambers cover $1 < |\eta| < 2.7$.
The chambers have been segmented into two categories reflecting their use: precision chambers, having good spatial resolution, and trigger chambers, having very good time resolution and enabling bunch crossing (BC) identification.

Precision chambers

For the precision measurements in the bending direction of the muon track, Monitored Drift Tube (MDT) chambers are used except in the innermost ring of the endcap inner station ($2 < |\eta| < 2.7$) where Cathode Strip Chambers (CSC) are used because of the higher particles fluxes.
Each muon chamber consists of two multilayers of detectors either side of a support structure. The MDT chambers consist of two multilayers of three or four planes of pressurized 30 mm aluminum drift tubes. The pressurized gas is non flammable and a pressure of 3 bars yields a single straw resolution of $\sim 80\,\mu$m. The CSCs are fast multiwire proportional chambers that measure position by determining the center of gravity of the induced charge on the strips. High rates are manageable by suitably fine segmentation of the strips. Each CSC has a resolution of $\sim 60\,\mu$m and they will be grouped in a similar way to the MDT straws.

Trigger chambers

Dedicated muon detectors with a fast response time (less than two microseconds) will give a rough measurement of p_T which can be used to initiate the read-out of the other sub-detectors. These trigger chambers have two-dimensional segmentation to facilitate pattern recognition and to identity which of the precision hits are related to a particular muon track. The second coordinate is measured with sufficient accuracy to allow corrections for magnetic field in inhomogeneities to be applied.
Triggering has to be achieved over $0 \leq |\eta| \leq 2.4$ for muons with energy greater than about 6 GeV, with a time resolution of approximately four nanoseconds - comfortably sufficient to identify a single bunch crossing.

5.3.5. DAQ and Trigger

In total the ATLAS detector has more then 10^8 electronic channels. The raw event data size is expected to be of the order of 1 Mbyte. If all events are read out (at 40 MHz) this would amount to an output of 40 terabytes of data per second, the storage of which would be grossly unachievable.
As can be seen in figure 5.16 the cross-section for producing high p_T physics at the LHC is many orders of magnitude below the total cross-section, so it is clear that efficient event selection will be extremely important. An overall rejection factor of nearly 10^7 is required while at the same time maintaining good efficiency for rare new physics.

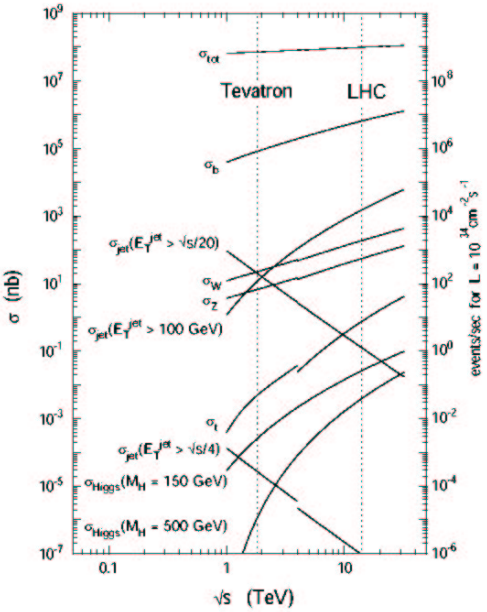

Figure 5.16.: *Energy dependence of some proton-(anti-)proton cross-sections at the* LHC *and at the* TEVATRON. *The discontinuity at $\sqrt{s} = 4\,TeV$ is caused by the transition from $p\bar{p}$ to pp, from [24].*

The ATLAS trigger system is based on three levels of selection, figure 5.17. Each subsequent level faces a lower event rate, and so can afford a higher level of sophistication per event. The first level trigger makes a decision based on reduced granularity calorimeter a muon detector information. Examples of objects which can initiate a first level acceptance are high p_T muons, isolated EM clusters, jets an missing p_T. With a latency of 2 μs the initial rate of 40 MHz is reduced to 100 kHz.

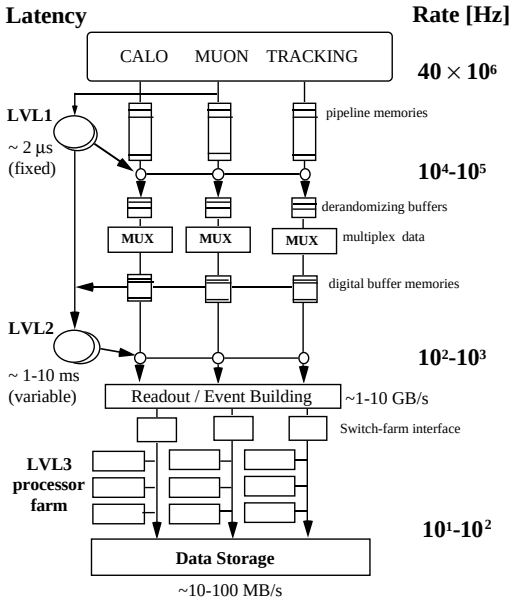

Figure 5.17.: *The three-level* ATLAS *trigger system*

The second level exploits completely the information given by the detectors and combines the information, but will concentrate on those regions of interest (ROI) already selected by level 1. The ID tracking data is considered for the first time at level 2, allowing selection of events with low energy electrons and heavy quark candidates. With a latency of 1-10 ms the second level has a rejection factor of about 100.
At the third and final level, the event filter, the event is fully reconstructed and a decision made whether to reject it or pass it to the permanent storage system for later analysis. With a latency of about 1 s the rate is reduced once more by a factor 10 to get a final rate of 10-100 Hz. This corresponds to 1 Pbyte per year for an event size of about 1 Mbyte.
The calculation power for the whole trigger system is estimated to about 10^5 to 10^6 MIPS (Million of instructions per second).

6. Z' production and decay properties at Hadron Colliders

6.1. Production

At a hadron collider, Z' production proceeds dominantly through the process $q\bar{q} \to Z'$.
A high-energy hadronic collision can be viewed as a collision involving quarks and gluons (partons). The partons are constituents of the incoming hadrons, and it is assumed that a collision involves one parton from each hadron, rather than a hadron as a whole. The other partons do not take part in the hard scattering.

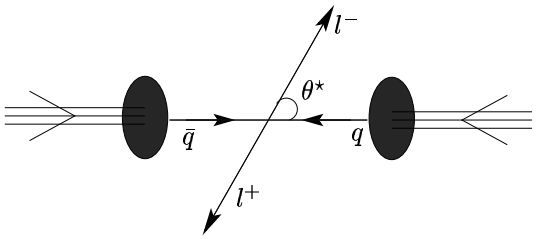

Figure 6.1.: *l^+l^- pair production in $p\bar{p}$ collisions, $\theta^\star = \measuredangle(e^-, q)_{Z'}$*

6.2. Decay

Considering only decays into known particles, the most efficient way of observing new gauge bosons in pp colliders is to identify charged leptons in the final state: $pp \to l^+l^-X$ (see figure 6.2).

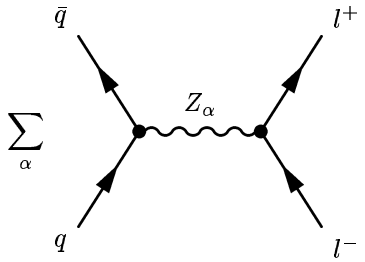

Figure 6.2.: *Lowest order graph contributing to the process $q\bar{q} \to l^+l^-$; $Z_\alpha = \gamma, Z, Z'$*

Hadronic decays ($Z' \to q\bar{q}$) are difficult to detect in the QCD background. Decays such as $Z' \to W^+W^-, f\bar{f}Z, f\bar{f}W, Z'Z, Z'\gamma$ [27, 28] are expected to be rare[(1)] and decays into neutrinos are invisible. For Feynman diagrams of the different decay channels see figure 6.3.

The unpolarized differential cross section for the process $pp \to l^+l^-X$ depends on the lepton invariant mass M_{ll}, on the rapidity Y of the Z' and on the angle $\theta^\star$. Rapidity is defined as

$$Y = \frac{1}{2} \ln \frac{E + p_z}{E - p_z},$$

where the z-axis (beam-axis) is chosen as direction. $\theta^\star$ is defined (see figure 6.1) as the angle between the negatively charged lepton and the quark in the center of mass of the colliding partons.

[1] For example, the decay $Z' \to W^+W^-$ is expected to be rare as its rate is suppressed by the square of the sine of the mixing angle between the Z and the Z', which is known from the LEP data to be small in the usual models.

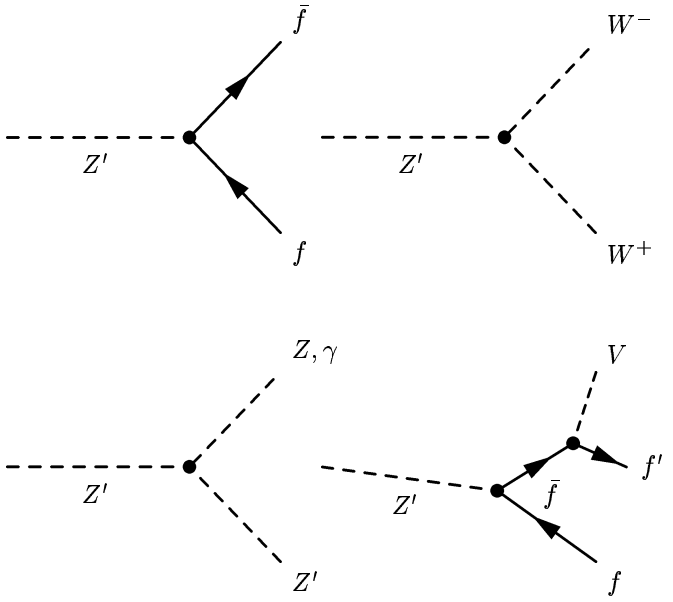

Figure 6.3.: *Decay channels,* $V = Z, W, \gamma$

The general form of this cross section is [8]

$$\frac{d\sigma}{dM\,dY\,d\cos\theta^\star} = \sum_{\text{quarks q}} [g_q^S(Y,M)S_q(M)(1+\cos^2\theta^\star) + g_q^A(Y,M)A_q(M)2\cos\theta^\star], \tag{6.1}$$

where S_q and A_q are the only model-dependent quantities as they involve the couplings of quarks and leptons to the different neutral gauge bosons; while g_q^S and g_q^A involve the parton distribution functions of the colliding hadrons.

6.2.1. Leptonic decay channels

e^+e^-

This channel is the most promising channel in ATLAS as the observed width will be dominated by the natural width and not by the detector resolution [17]. For the electrons, the energy is determined in the electromagnetic calorimeter. The energy resolution is dominated at high energy ($E > 200\,\text{GeV}$) by the constant term in calorimeter energy resolution. This term is estimated to $\sim 0.7\,\%$ (neglecting photon radiation), i.e. a resolution of 14 GeV for 2 TeV electrons.

$\mu^+\mu^-$

For this channel in ATLAS the decay width is dominated by the resolution of the detector. The energy resolution for the muons (measurements in the muon spectrometers) should be of the order of 20 % (i.e. 400 GeV for 2 TeV muons), that means generally higher than the expected natural decay width; as we will see later, the natural decay width for 4 TeV Z' bosons in the studied models is of the order of 20-200 GeV. A study of this channel was already performed in [29].

$\tau^+\tau^-$

The study of the τ channel [30] is more difficult as the τ is decaying into unobserved neutrinos, nevertheless a $Z' \to \tau^+\tau^-$ event is sufficiently constrained that it is possible to reconstruct the momenta of both τ's[2]: if a $\tau^+\tau^-$ pair is known to be the product of a Z' decay, it must satisfy two constraints. Since the width of the Z' is expected to be small compared to its mass, the invariant mass of the $\tau^+\tau^-$ system must equal $M_{Z'}$, assumed to be a known quantity. Similarly, measuring the jets not belonging to the τ decay and demanding transverse momentum balance yields the transverse momentum of the Z'. These

[2] in the cases $\tau \to e\nu\nu$ and $\tau \to \mu\nu\nu$

two constraints uniquely determine x_+ and x_-, where $x_\pm$ is the "visible" momentum fraction, i.e. the fraction of the $\tau^\pm$'s momentum contained in decay products which are observable through tracking and calorimetry [31].
In the τ channel further information can be extracted from the polarization asymmetry, the production asymmetry of left and right handed $\tau's$. Left and right handed $\tau's$ can be identified as the τ decay proceed through weak interaction, which violates parity. Left and right handed $\tau's$ have thus different decay properties.

In the following I have chosen to concentrate on the e^+e^- channel as it is the most promising and so the most suited for a discrimination - once a Z' should be discovered.

6.2.2. Background

The physical background that will be discussed in detail in chapter 8 is very small. The channel $Z' \to e^+e^-$ has two advantages: firstly it benefits from the high detector resolution of ATLAS on electrons and secondly it is very clean.

6.3. Observables sensitive to Z' properties

The LHC discovery potential for a Z' as a resonance curve above a small background in the reaction $pp \to Z' \to e^+e^-$ is well known [3]. The required luminosity to discover a Z' basically depends only on its cross section, and therefore on its mass and its couplings.
Once a Z' boson is observed at the LHC, one can measure its mass, its total width and its cross section. Furthermore, forward-backward asymmetries provide additional information about its couplings and interference effects with the Z boson and the photon. In addition one can include the analysis of the Z' rapidity distribution, which is sensitive to the Z' couplings to $u\bar{u}$ and $d\bar{d}$ quarks. As these variables are sensitive to the couplings and so to different models, they are proposed to be used to discriminate between the different models. We will follow the strategy proposed in [3].
In the following sections I will present these variables with their theoretical predictions when available.

6.3.1. Total decay width Γ

The total decay width is essentially obtained by a fit to the invariant mass distribution M_{ll} of the reconstructed dilepton system (the resonance curve) using a relativistic Breit-Wigner function. Hadrons are distributed according to a non-relativistic Breit-Wigner distribution and leptons and resonances according to a relativistic one:

$$p(M) \propto \frac{\Gamma^2 M^2}{(M_{ll}^2 - M_{Z'}^2)^2 + \Gamma_{Z'}^2 M_{Z'}^2}.$$

In the absence of any exotic decay channel the total decay width is given by the sum of the partial decay widths of neutrinos, leptons and quarks of all 3 generations. Rare decays such as $Z' \to W^+W^-$ are not included in the simulation, only fermionic decay channels are implemented. In weak interactions for the decay of a vector boson X into two spin-$\frac{1}{2}$ fermions f_1 and f_2 with a vertex factor $-ig_x\gamma^\mu \frac{1}{2}(g_V - g_A\gamma^5)$ (figure 6.4), the partial decay width Γ is given by [32]:

$$\Gamma(X \to f_1\bar{f}_2) = N_c \frac{g_x^2}{48\pi}(g_V^2 + g_A^2)M_X,$$

where the couplings g_A and g_V are taken from table 4.7. In the case of the Z or Z' boson, $g_x = \frac{g}{\cos\theta_w}$ with the notation of section 4.1.2 and with N_c a color factor[3].
As $\Gamma \propto M$ the results for $\frac{\Gamma}{M}$ are given in table 6.1 for the different models. Already at this stage, it is clear that the decay width alone will not be sufficient to discriminate.
The formula used above is valid for neglected fermion masses; the only fermion mass that cannot be totally neglected is the top quark. Correcting for the top mass leads to a little smaller $\frac{\Gamma}{M}$ depending on the models [31]. The partial decay width in quarks should also undergo small corrections due to final-state QCD interactions.

[3] 1 for leptons, 3 for quarks
[4] The ratio $\frac{\Gamma}{M}$ for the SSM is not identical to the same ratio for the ordinary Z because the Z cannot decay in $t\bar{t}$.

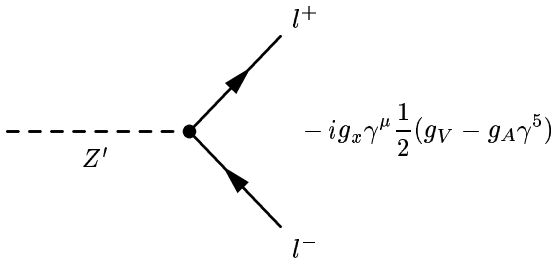

Figure 6.4.: *Z' decay vertex*

	$\frac{\Gamma}{M}$	$\Gamma(M = 1.5\,TeV)(GeV)$	$\Gamma(M = 4\,TeV)(GeV)$
$SSM^{(4)}$	0.030	44.7	119.2
Z'_ψ	0.005	8.0	21.2
Z'_χ	0.012	17.6	46.8
Z'_η	0.006	9.5	25.2
LR, $\kappa = 1$	0.020	30.6	81.6

Table 6.1.: *Total decay width (predictions)*

6.3.2. Cross section σ_{ll}

We call "leptonic cross section" the product of total cross section and the leptonic branching ratio: $\sigma_{ll} = \sigma_{tot} \cdot Br(Z' \to l^+l^-)$. The leptonic cross section is determined from the events in the peak of the mass distribution. As peak the mass range $M \pm 4\Gamma$ is used. In table 6.2 the results given by PYTHIA (generation of 10 000 events without interference only in the peak region) are shown.

	$\sigma_{ll}(fb)$ at $M = 1.5$ TeV	$\sigma_{ll}(fb)$ at $M = 4$ TeV
SSM	78.8	0.26
Z'_ψ	23.5	0.08
Z'_χ	47.9	0.13
Z'_η	26.3	0.09
LR	50.0	0.16

Table 6.2.: PYTHIA *predictions for the leptonic cross section*

The Z' cross section should be measured relatively to the number of produced Z bosons for the same lepton final state. Using this approach, many systematic uncertainties due to theoretical and experimental uncertainties will cancel, and the relative Z'/Z cross section ratio might be measured and calculated with an accuracy of about 1% [33]. However, it is not sure whether normalisation on the Z cross section will be a good choice as the mass of the Z' is much higher as the one of the Z. There could be large changes in acceptance,... going from Z to Z'. In any case, as absolute cross sections are difficult to measure, the cross section should be normalized to another well-known process, if possible in the same or close energy range.

As discriminating variable one must chose $\Gamma \cdot \sigma$ instead of σ and Γ, as both, the total width and the cross section are altered if exotic decays of the Z' boson are present, e.g. decay into gauginos $Z' \to \tilde{\chi}_i\tilde{\chi}_j$ [34]. However, this dependence disappears in the product, so it is the product that should be used in order to discriminate models independently of the decays [3]. Γ and σ separately would not bring any further information anyway.

6.3.3. Forward backward asymmetries

Another signature of the Z' gauge bosons are the forward-backward asymmetries [35, 36] in their production and leptonic decays. The differential cross section contains (see formula 6.1) a term proportional to $\cos\theta^\star$, i.e. the decay properties in forward and backward direction are not identical. This

term is due to the V-A structure of the electroweak interaction and its form is typical for particles of spin 1.

$$\frac{d\sigma}{d\cos\theta^\star} \propto \frac{3}{8}(1+\cos^2\theta^\star) + A_{FB}\cos\theta^\star \tag{6.2}$$

The forward backward asymmetry is defined as

$$A_{FB} = \frac{\sigma_F - \sigma_B}{\sigma_F + \sigma_B},$$

where $\sigma_F(\sigma_B)$ is the forward(backward) cross section; it is a function of the rapidity Y of the Z' and of its mass M. This means that the forward backward asymmetry is the asymmetry between the number of events where the electron is flying in forward respectively backward direction.

Concept of forward and backward direction

In pp collisions one has to be attentive to the forward/backward definition, i.e. to the definition of $\cos\theta^\star$ which refers to the direction of the initial positive charged parton (the quark).
In contrast to $p\bar{p}$ colliders, where a natural understanding of forward (backward) direction is given by the p ($\bar{p}$) direction, in pp collisions one has to introduce an artificial understanding of forward (backward) by examining the quark (antiquark) direction.
High mass dilepton events in pp collisions originate from the annihilation of valence quarks with sea antiquarks or from the annihilation of sea quarks with sea antiquarks. As the valence quarks have on average a much larger momentum than the sea antiquarks, the boost direction of the dilepton system approximates the quark direction [37]. So forward (defined as the quark direction) is approximated by the boost (or Z') direction. This approximation is usually correct for Z' bosons with large rapidities Y but frequently incorrect for a Z' with small rapidity (in this case the Z' often flies in the same direction as the antiquark, as the antiquark is faster than the quark.)

Because of this indetermination, firstly the *observed asymmetry* A_{FB}^{obs}, i.e. the asymmetry with respect to the Z' direction, will be determined. Secondly, the error introduced by this approximation will be corrected by introducing a dilution factor in order to recover the *true asymmetry* A_{FB}^{true}; the obtained result will be called *corrected asymmetry* A_{FB}^{corr}.

The forward-backward asymmetry as a function of M

As $\cos\theta^\star$ is defined as the angle between the electron and the quark direction, $A_{FB}^{true}(M)$ is calculated as:

$$A_{FB}(M)^{true} = \frac{(\int_0^1 - \int_{-1}^0) d\cos\theta^\star \frac{d\sigma}{dM d\cos\theta^\star}}{\int_{-1}^1 d\cos\theta^\star \frac{d\sigma}{dM d\cos\theta^\star}}. \tag{6.3}$$

Experimentally the quark direction will not be known and will be approximated by the Z' direction. In this case, one can also write A_{FB}^{obs} as

$$A_{FB}(M)^{obs} = \frac{(\int_0^{Y_{max}} - \int_{-Y_{max}}^0) dY (\int_0^1 - \int_{-1}^0) d\cos\theta^\diamond \frac{d\sigma}{dM dY d\cos\theta^\diamond}}{\int_{-Y_{max}}^{Y_{max}} dY \int_{-1}^1 d\cos\theta^\diamond \frac{d\sigma}{dM dY d\cos\theta^\diamond}}, \tag{6.4}$$

where $\theta^\diamond$ is now the angle between the electron and the z-axis of the detector. The Z' rapidity is determined as usually with respect to the z-axis. One has to emphasize that in formula 6.4 the approximation that the Z' direction equals the quark direction is already made - contrarily to formula 6.3.

So one can determine on the one hand $A_{FB}(M)$ by counting the events to get the different cross-sections. On the other hand it can be determined by a fit on $\frac{d\sigma}{d\cos\theta^\star}$ (formula 6.2).

Furthermore, the following characteristics are predicted:

- Calculation shows that the asymmetry is close to zero on the mass peak for the SSM [17].
- For E_6 models [3]:
  - since the up type quarks have no axial couplings to the Z' boson, they do not contribute to the asymmetry on the Z' peak,
  - the on-peak asymmetry completely vanishes for three β values: $\beta = \arctan(-\sqrt{\frac{3}{5}}) - \frac{\pi}{2}, 0, \pi$; where left and right handed Z' couplings of both d-quarks and charged leptons are equal,
  - off the Z' resonance, there is always an asymmetry that is generated by the Z boson couplings.
- In KK models, typical dips occur in the asymmetry curves [20].
- For masses below the peak, but close to the resonance, the asymmetry can also be used to distinguish between a Z' and pure DY or even between the different models (off-peak asymmetry).

The forward-backward asymmetry as a function of Y

For $A_{FB}(Y)$ we have:

$$A_{FB}(Y) = \frac{(\int_0^1 - \int_{-1}^0) d\cos\theta^\diamond \frac{d\sigma}{dY\, d\cos\theta^\diamond}}{\int_{-1}^1 d\cos\theta^\diamond \frac{d\sigma}{dY\, d\cos\theta^\diamond}}. \tag{6.5}$$

In this definition one has to take $\theta^\diamond$ because Y is defined according to the z-axis and not to the quark direction.
In pp interactions, the forward-backward asymmetries are necessarily antisymmetric about Y=0 [13] and hence the $\cos\theta^\diamond$ distributions are symmetric because the Y distribution is symmetric.
This asymmetry is explained by the following:
If $Y > 0$, then the electron is expected (for example) to be most of the time forward. Therefore, we have $A_{FB}(Y) > 0$. If $Y < 0$, then the electron will be backward most of the time and $A_{FB}(-Y) < 0$ as the used axis is the z-axis. In brief, the electron either tends to follow the Z' direction or tends to fly in the opposite direction; it doesn't care whether the Z' is forward or backward. So, $\theta^\diamond$ is with respect to the z-axis symmetric and $A_{FB}(Y)$ is antisymmetric with respect to 0.
$A_{FB}(Y)$ is indeed very sensitive to the specific form of the couplings, as one can see by comparing the predictions for several models in figure 6.5.

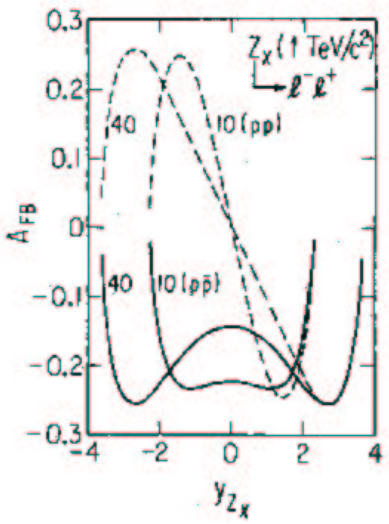

(a) $A_{FB}(Y)$ for $M_{Z'_\chi}$ at $\sqrt{s} = 10$ TeV for pp and $\bar{p}p$ [13].

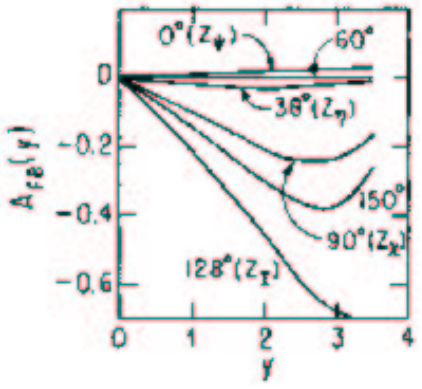

(b) $A_{FB}(Y)$ at $\sqrt{s} = 40$ TeV at $M_{Z'}$=1 TeV for pp for various models [38].

Figure 6.5.: $A_{FB}(Y)$ *distributions*

6.3.4. The Z' rapidity distribution

The Z' rapidity distribution is also expected to discriminate between the different models as it allows to obtain the fraction of Z' bosons produced from $u\bar{u}$, $d\bar{d}$ or sea-quark initial states. The Z' rapidity distribution itself is not sufficient to discriminate between the models, a more precise analysis on the relative parton distribution functions for u and d quarks must be done.
Another proposal is given in [39], in which the rapidity ratio r_{y_1}, with y_1 chosen in $0 < y_1 < y_{max}$, is studied and connected to the couplings of the Z'.

$$r_{y1} = \frac{\int_{-y1}^{y1} \frac{d\sigma}{dy} dy}{\left[\int_{-y_{max}}^{-y_1} + \int_{y_1}^{y_{max}}\right] \frac{d\sigma}{dy} dy}$$

None of these ideas will be considered in this work.

6.4. Limits on Z' discovery from existing data and Z' reach in ATLAS

Limits on the existence of a Z' may be divided into two categories: limits from direct search, and limits from indirect arguments. Direct search limits arise from the failure to observe a Z' resonance in high-energy collisions, whereas indirect search limits arise from a collection of diverse effects where the existence of a Z' would affect physical observables even if the Z' were too massive to be produced on-shell. Both direct and indirect searches lead to model-depend constraints. Although the direct and indirect limits on $M_{Z'}$ are similar, the ranges of parameter space excluded by the two methods are different and the two methods are complementary.
If the Z' charges are generation dependent, there exist severe constraints in the first two generations from precision measurements; constraints on a Z' which couples differently to the third generation only are somewhat weaker [40].
If the Z' has suppressed or no couplings to leptons (i.e. it is leptophobic [41]), then these experimental limits will be even weaker. A light Z' ($M_{Z'} \lesssim M_Z$) boson has been ruled out in pre-LEP experiments unless it has extremely weak couplings to leptons [42]. Searches for a Z' via hadronic decays at CDF are unable to rule out a Z' for the SSM case in any mass region.

6.4.1. Current indirect constraints

Indirect constraints are obtained by high precision measurements of neutral-current processes at low energies, Z-pole constraints on Z-Z' mixing and indirect constraints from precision electroweak measurements off the Z-pole.
At low energy Z-Z' mixing implies a shift in some electroweak parameters and the couplings of the effective neutral-current Lagrangian are sensitive to the mixing. The Z-pole observables, like mass, (partial) decay width(s), branching ratios, asymmetries depend also on the Z-Z' mixing and thus on the existence and properties of a Z'. At high-energy (off the Z-pole) constraints arise by comparing measurements of asymmetries and cross-sections with the SM predictions. These processes are also sensitive to direct Z' exchange.
The present Z' mass limits for the different models are summarized in table 6.3 [43].
The limit in the KK case given in table 6.3 is given in the hypothesis of a "SM" Higgs, i.e. a light Higgs boson propagating in higher dimensions. In the case of a trapped Higgs boson with a large mass (up to 500 GeV) relatively light KK mass scales are possible [45]. In Higgsless models, lighter KK gauge bosons are possible [46] as well.
It is also possible to reconcile a heavy ($M > 170$ GeV) Higgs boson with the precision electroweak fits by adding heavy Z' vector bosons. The shifts on the electroweak parameters due to the Z' can compensate the effect of a heavy Higgs boson in some cases [47]. In these models the indirect limits presented above are not valid.

6.4.2. Current direct search limits

High-energy experiments have searched for on-shell Z' production and decay. Searches can be classified by the initial state of which the Z' is produced (e.g. hadron or e^+e^- colliders), and the final state into which the Z' decays (e.g. di-electron, di-muon channels).

Z' model	Mass (95% C.L.)	Exp/Author	
Z_{SSM} Sequential SM	>1500 GeV	K.Cheung (2001)	precise electroweak
	>690 GeV	CDF (1997)	$p\bar{p} \to e^+e^-; \mu^+\mu^-$ combined
	>1787 GeV	LEPII (2003)	combined electroweak
$Z_{LR}, \kappa = 1$ Left-Right Sym. Model	>860 GeV	K.Cheung (2001)	precise electroweak
	>630 GeV	CDF (1997)	$p\bar{p} \to e^+e^-; \mu^+\mu^-$ combined
	>804 GeV	LEPII (2003)	combined electroweak
Z_χ $SO(10) \to SU(5) \times U(1)_\chi$	>680 GeV	K.Cheung (2001)	precise electroweak
	>595 GeV	CDF (1997)	$p\bar{p} \to e^+e^-; \mu^+\mu^-$ combined
	>673 GeV	LEPII (2003)	combined electroweak
Z_ψ $E_6 \to SO(10) \times U(1)_\psi$	>350 GeV	DELPHI (2000)	$e^+e^- : Z - Z'$ mixing
	>590 GeV	CDF (1997)	$p\bar{p} \to e^+e^-; \mu^+\mu^-$ combined
	>481 GeV	LEPII (2003)	combined electroweak
Z_η E_6 models	>619 GeV	G.Cho (2000)	precise electroweak
	>620 GeV	CDF (1997)	$p\bar{p} \to e^+e^-; \mu^+\mu^-$ combined
	>434 GeV	LEPII (2003)	combined electroweak
KK	$\geq$ 4 TeV		precise electroweak, [17] and references therein

Table 6.3.: *Current mass limits for various Z' models [43, 44]*

The present Z' mass limits are given as well in table 6.3 [43]; the results of CDF should improve using Run II data and combining with $D\emptyset$ data..
In LEPII no significant evidence is found for the existence of a Z' boson in any of the models. The lower limits on the Z' mass are shown in figure 6.6 and given as well in table 6.3.

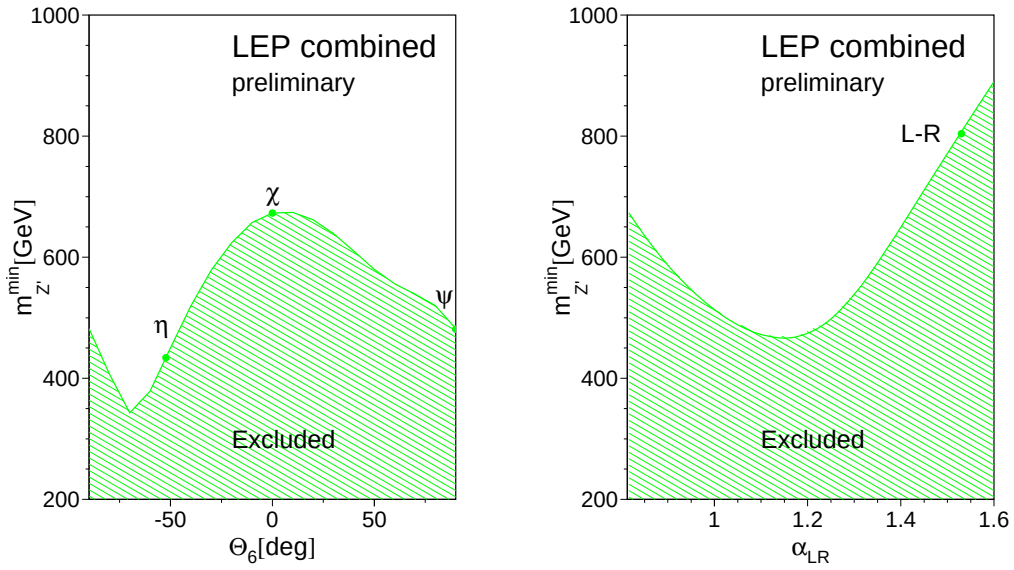

Figure 6.6.: *The 95% confidence level limits on $M_{Z'}$ as a function of the model parameter Θ_6 for E_6 models and α_{LR} for left-right models. The $Z - Z'$ mixing is fixed: $\Theta_{ZZ'} = 0$.*

For a heavy Z' ($M_{Z'} >> M_Z$), the best limits come from $p\bar{p}$ colliders via Drell-Yan production and subsequent decay to charged leptons. CDF quotes limits on $\sigma(p\bar{p} \to Z'X) \cdot Br(Z' \to l^+l^-) < 0.04\,\text{pb}$ at 95% C.L. for $l = e + \mu$ combined (Run I).

6.4.3. Reach at LHC

The discovery potential for a Z' boson (SSM case) is presented in figure 6.7 [48] for the LHC detector ATLAS. Shown is the value of σ_{ll} relative to the value for the ordinary Z boson, that is needed for a $5\,\sigma$ confidence level signal as a function of the mass of the Z' for an integrated luminosity of $100\,fb^{-1}$ for three different decay channels: e^+e^-, $\mu^+\mu^-$ and jet-jet.[5]
One can see for instance that a 2 TeV Z' could be discovered in the e^+e^- channel with $100\,fb^{-1}$ if $\sigma_{ee,Z'} \gtrsim 0.007\sigma_{ee,Z}$.
The e^+e^- channel is the most promising and lighter Z' bosons would be easier to discover than heavier ones.

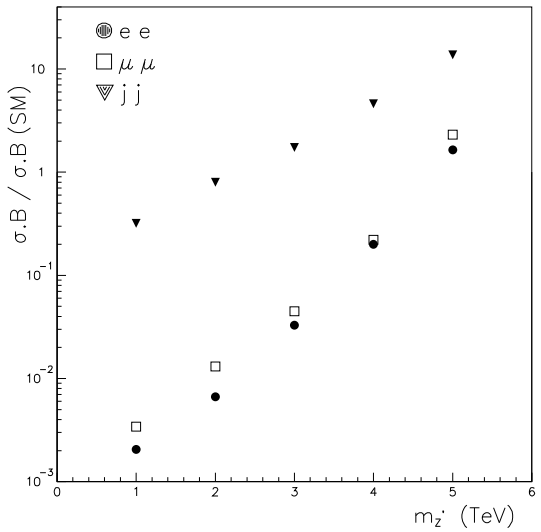

Figure 6.7.: *Discovery potential for a SSM Z' with $100\,fb^{-1}$ as a function of its mass at* ATLAS.

Moreover, ATLAS should be able to detect Z' bosons up to 5-8 TeV for $100\,fb^{-1}$ and up to 10-11 TeV for $300\,fb^{-1}$ by direct and indirect search depending on the model [17, 3].

6.5. Conclusions

In this chapter, first production and decay properties of the Z' at a hadron collider such as the LHC have been presented. One of the leptonic decay channels namely $Z' \to e^+e^-$ was chosen, as it gives a very clear signal that should easily be observed and studied at LHC- if a Z' exists. In fact, Z' bosons at low masses up to about at least 600-700 GeV depending on the model, are already excluded: by direct and also indirect searches. ATLAS should be able at high luminosity to detect new gauge bosons up to 10-11 TeV.
Once such an extra gauge bosons would be discovered, its decay properties will be examined to identify its theoretical framework. For this purpose the following variables are good candidates: the total decay width, the cross-section, forward-backward asymmetries. They will be studied in the next chapters and the capability and precision of ATLAS in extracting these variables will be examined to evaluate their discriminating power.

[5] For the jets $p_T > 300$ GeV is required.

7. Analysis at generation level ($M = 1.5$ TeV and $M = 4$ TeV)

Analysis is done at generation level in order to understand the phenomenology and to develop and validate the methods of analysis without any hadronisation or detector effects. The potentially discriminating variables are studied and compared to theoretical predictions to confirm the analysis procedure and their discrimination power is studied.
The generator gives access not only to the generated 4-momentum (in the lab frame) and the particle identification, but also to the complete filiation of all particles.

7.1. Event generation

In a first step events are generated with PYTHIA 6.2 [49]: 2 proton beams with a center-of-mass energy of 14 TeV. This generation is done within ATHENA [50] (version 7.0.2), the future unique program in ATLAS for all simulation, reconstruction and analysis. It is based on C++, the object oriented structure allows a modular approach according to the dimension and complexity of the ATLAS project.
The Z' boson is generated in the $pp \to Z' \to e^+e^-$ channel at masses of 1.5 TeV and 4 TeV. The first value was chosen as it is a realistic proposal regarding the present limits and for comparison purpose with other studies. Furthermore it is a reasonable value for studies at 10 fb^{-1} which offers interesting possibilities for commissioning. The second value was chosen as the Z'_{KK} is already excluded below 4 TeV.
For the different E_6 and LR models (and the SSM) the couplings g_V and g_A are varied for the 3 lepton families. For the Z'_{KK} an user defined external process was interfaced to ATHENA[1]: the full Breit-Wigner shape for the first two excitations of the photon and the Z boson are included. The higher lying states are resummed. The matrix elements are interfaced to the PYTHIA event generator as an external process, and the generated events use the full PYTHIA machinery for QCD showering from the initial state quarks and for hadronisation. Masses and couplings are defined, the different decay widths calculated.
For each model 60 000 events are generated at both values for the mass. This corresponds of course not to a realistic integrated luminosity, but high statistics were preferred here to validate the analysis procedure. Generation is made without initial and final state radiation (ISR and FSR) to be as close as possible to theory[2]. By ISR, radiation of the incoming quarks is understood and by FSR, radiation of the outgoing leptons. In order to get a better efficiency, cuts are introduced at the generation level: 1 TeV for the total energy in the center-of-mass of the Z' for a Z' at a mass of 1.5 TeV. At 4 TeV the cut is at 2.5 TeV.
As it will be mentioned in section 8 the main irreducible background of the Z' signal is the Z/Drell-Yan production and decay as the physics underlying this process is exactly the same. Therefore, the Z' is not produced independently but always with this complete interference structure. In section 7.5 I will have a closer look to the effect of the interference.
The dependence on different parton distribution functions is not studied in this work, this should be done later. In [17] the dependence on different parton distribution functions was already studied in the case of a Z'_{KK} in a study of the compactification scale. CTEQ5L was used.

7.2. Analysis at generation level

First I will show some basic distributions of the signal. Then I will discuss in detail the analysis done for $M = 1.5$ TeV and at the end of the chapter I will present the results for $M = 4$ TeV. In this chapter no detector simulation is done at all. As a first step the potential discriminating variables are determined using the generated events without any simulation or detector effects. They are compared with the

[1] external process for PYTHIA: T.Rizzo and G.Azuelos [17], interface with ATHENA M.Schäfer
[2] In small samples a cross-check with generation with ISR and FSR was made, and

$$M_{inv}(\text{with FSR}, e^+ + e^- + \sum_\gamma) = M_{inv}(\text{without FSR}, e^+ + e^-)$$

was verified.

theoretical predictions to confirm the analysis procedure and their discrimination power is studied.

Besides the DY background no background is considered at this step.

The integrated luminosity $\mathcal{L}$ of the generated ntuple files can be determined from the number of events generated N_{gen} and the cross section σ_P given by PYTHIA: $\mathcal{L} = \frac{N_{gen}}{\sigma_P}$.

The analysis is done with ROOT [51].

For all statistical errors the gaussian law is used:

$$\Delta^2 f(x_1, ...x_n) = \sum_{i=1}^{n} \left(\frac{\partial f}{\partial x_i}\right)^2 \Delta^2 x_i.$$

7.3. Kinematics of the Z'

Several cuts are applied to ensure that only events with exactly two leptons with opposite charge that have the Z' boson as "mother" are used[3].
In figure 7.1 the p_T and pseudorapidity $|\eta|$ of the leptons, as well as the angle α, the opening angle between them in the transverse plane are presented for the SSM and the Z'_χ model as examples.
The p_T distribution follows a Jacobian law that peaks at $\sim \frac{M}{2}$. The second "peak" at about 500 GeV, which is much better visible for the Z'_χ model than for the SSM, has its origin in the $\sqrt{\hat{s}}$ cut at 1 TeV in the generation. In the case of the Z'_χ model the cross section of the Drell-Yan is important, so that the cut at 1 TeV resembles in the invariant mass spectrum to a second "resonance" (see figure 7.2(a)). In the case of the SSM model, the cross section of the Z' is important compared to the Drell-Yan, the cut at 1 TeV has less effect.
In figure 7.1 the p_Z distribution of the Z' is given as well. It is symmetric and one can see that the Z' is not produced at rest, but it is not too much boosted either.

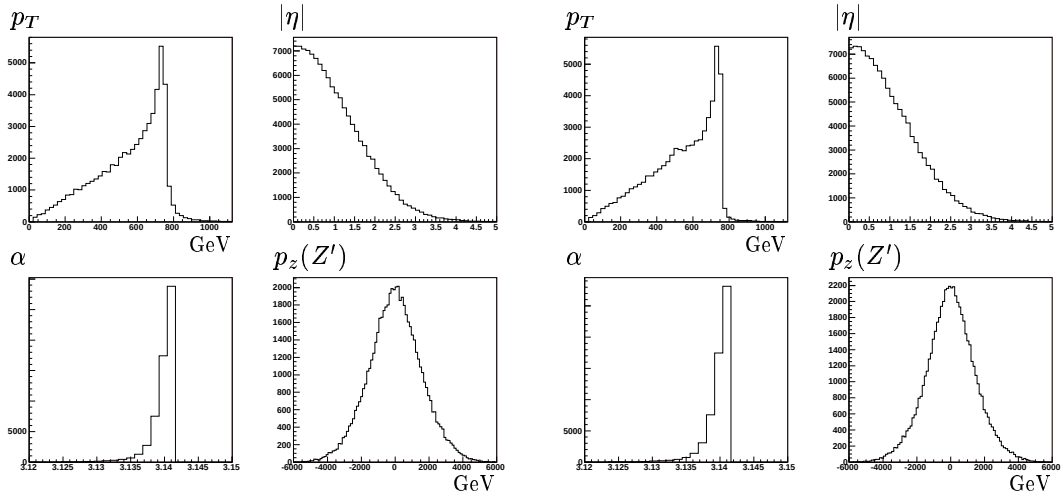

(a) SSM (b) Z'_χ

Figure 7.1.: *Kinematics for the SSM and the Z'_χ model*

[3] In fact, at this step all events are chosen as the generation works fine.

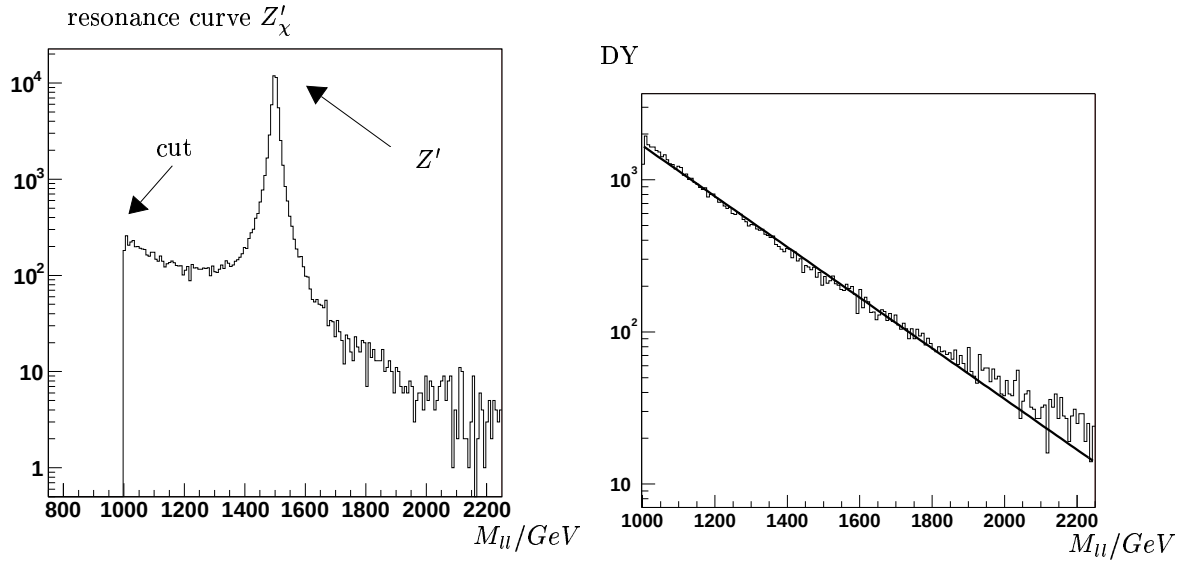

(a) *Invariant mass distribution for the Z'_χ model*

(b) *Invariant mass distribution for the DY process*

Figure 7.2.: *Invariant mass distributions*

7.4. Invariant mass spectrum

The invariant mass of the two leptons is calculated by summing the two 4-momenta (known from PYTHIA in the lab frame) and calculating the invariant mass:

$$M^2 = \sqrt{E^2 - \vec{p}^2}, \quad \text{with} \quad p = (\vec{p}, E) = (\vec{p}_{e^-} + \vec{p}_{e^+}, E_{e^-} + E_{e^+}).$$

The invariant mass spectrum for the ordinary Z boson, for the Drell-Yan-background of the Z' and of course for the different Z' models have been studied. The ordinary Z boson was studied only for validation purpose and I will not present the confirming results here, the Drell-Yan was studied as it is the main underlying background that is never separated from the signal. I recall that there was (except for the ordinary Z boson) a cut at 1 TeV in energy in generation.

Drell-Yan

The Drell-Yan distribution is approximated (figure 7.2(b)) by an exponential. This function will later be used to determine the decay width.

7.5. Z'- DY interference

To study the effect of interference the Z' is produced[4] on the one hand with the full interference structure (black/solid line in figure 7.3), on the other hand I produced the Z' and Drell-Yan separately and added them (normalized on integrated luminosity, red/dashed line in the figure).
I chose to present the SSM and the Z'_ψ model, as the SSM is the model with the biggest cross section and decay width and the Z'_ψ model the one with the smallest ones.
One can see that the interference affects the peak, but not really its width (figure 7.3): with interference it is wider at the right side, but narrower at the left side. In the region at about 1000-1200 TeV the interference effects are the strongest ones and destructive. At low energies, at least at about 400 GeV the two curves converges, one finds the pure DY.
The effects are more important for the SSM, i.e. for Z' models with higher cross section/large decay

[4] To study interference effects also at low energy I chose here at generation level a cut at 400 GeV instead of 1 TeV.

width. In these cases the indirect discovery possibilities are important through the deviation from the SM Drell-Yan.

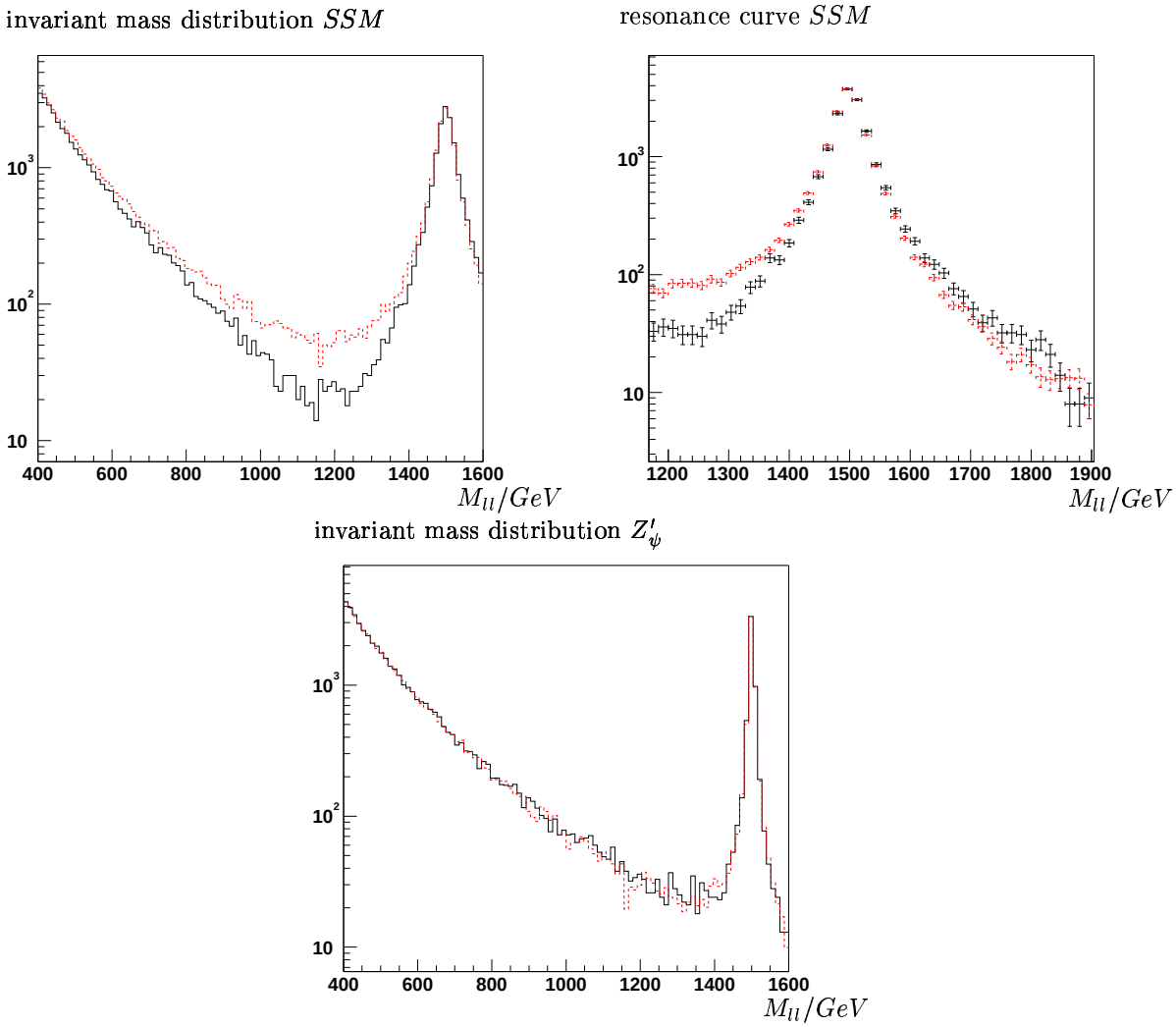

Figure 7.3.: *Interference effects for the SSM (first line) and the Z'_ψ model (second line), black/solid line with full interference structure, red/dashed line only Z' and DY*

7.6. Total decay width Γ

I made a fit with the following function over a large range around the peak:

$$f(x) = \frac{a}{(x^2 - \breve{M})^2 + b} \cdot \exp^{-cx} + d\exp^{ex},$$

where

- $\frac{a}{(x^2-\breve{M})^2+b}$ is a Breit-Wigner (BW) with $b = \Gamma^2\breve{M}$ and $\breve{M} = M^2$,
- $\exp^{-cx}$ takes into account the parton luminosity and the deformation of the peak by the interference,
- $d\exp^{ex}$ takes into account the Drell-Yan background, e is fixed to the value obtained by a fit of an exponential on the low-mass part of the distribution.

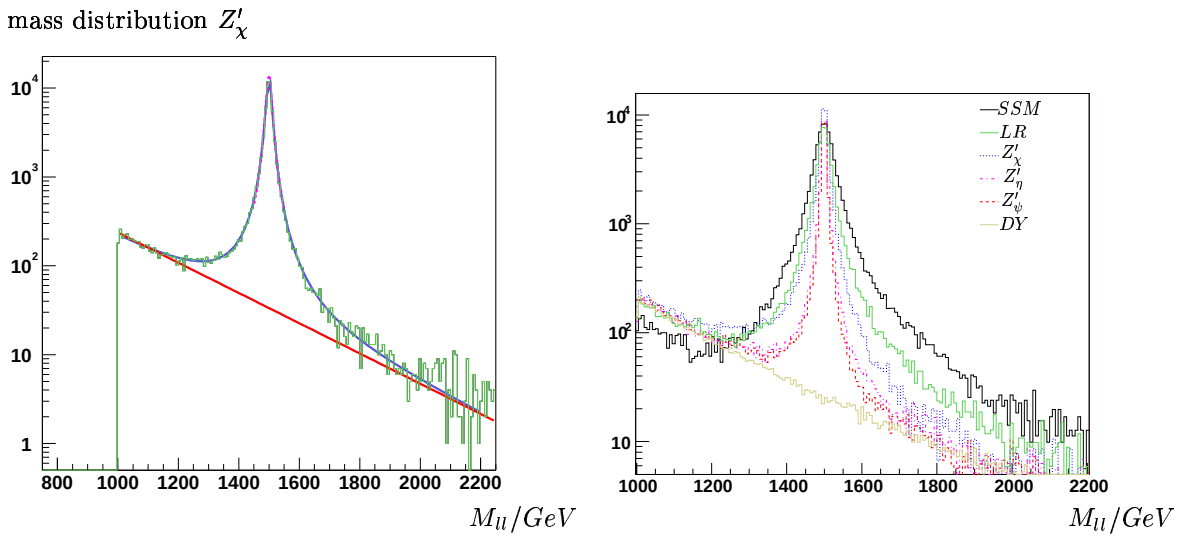

(a) *Fit for decay width (Z'_χ model)* (b) *resonance curve*

Figure 7.4.: *Decay width*

In figure 7.4(a) the fit result is shown for one model. The Drell-Yan is drawn in red/solid line, the BW in magenta/dashed line and the full fit in blue/solid line.
The value for the mass obtained by the fit is in good agreement with the generated mass. The fit with this function converges fine also in a wider range than the peak itself. For the models with high cross section there is a little problem at the left side of the peak, the fitted function is always higher than the histogram. This originates from the interference effects that are important and destructive in this region, as shown in section 7.5. Nevertheless, the shape of the peak is modelized fine.
In figure 7.4(b) the reconstructed di-lepton mass for all studied models are shown. They are normalized to have the same luminosity. In table 7.1 the obtained mass and decay widths are shown with the corresponding errors and the theoretical prediction. There is also shown the result of a simpler fit: only a BW in the peak-region. It is shown clearly that my more complex function works better. A good agreement is obtained, the width is slightly (1%-6%) overestimated. This systematic error grows with decreasing Γ and it is due to the approximation of the DY and the effect of the interference. The errors are taken from the errors from the fit parameters $\breve{M}$ and b:

$$M = \sqrt{\breve{M}} \rightarrow \Delta M = \frac{\Delta \breve{M}}{2\sqrt{\breve{M}}}$$
$$\Gamma = \sqrt{\frac{b}{\breve{M}}} \rightarrow \Delta^2\Gamma = \frac{\Delta^2 b}{4b\breve{M}} + \frac{b\Delta^2\breve{M}}{\breve{M}^3}$$

The total decay width offers the possibility to discriminate between the models but it could never be the only discriminating variable as the values of several models are too close. For the models with very small decay width, like the Z'_ψ or Z'_η, it could even be difficult to extract the natural decay width in spite of the good detector resolution which is of the same order or slightly higher (as we will see in chapter 9).

	M(GeV)	Γ_{BW}(GeV)	Γ(GeV)	Γ_{theo}(GeV)
SSM	1499.87 ± 0.17	47.33 ± 0.42	45.92 ± 0.33	44.7
Z'_ψ	1499.96 ± 0.02	8.51 ± 0.09	7.97 ± 0.09	8.0
Z'_χ	1499.89 ± 0.06	18.9 ± 0.14	18.40 ± 0.13	17.6
Z'_η	1499.96 ± 0.03	10.51 ± 0.09	10.07 ± 0.09	9.5
LR	1499.92 ± 0.10	32.49 ± 0.26	31.54 ± 0.21	30.6

Table 7.1.: *Results of the fit for the mass and the decay width*

7.7. Leptonic cross section σ_{ll}

To determine the leptonic cross section the events in $M \pm n\Gamma$ are counted (N_{tot}). I took $n = 4$. This is justified by figure 7.5 where I studied $\frac{\sigma(n\Gamma)}{\sigma(15\Gamma)}$ for the LR model that is quite large and for the Z'_ψ model, the narrowest one. $n = 4$ was chosen as a compromise of loosing signal and counting too much background. This loss of about 5% of signal could have to be considered later in the determination of the cross section. However, most of this lost events are Drell-Yan and not Z' events.

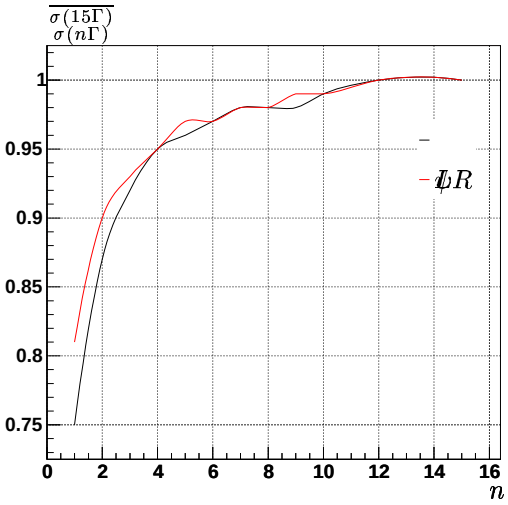

Figure 7.5.: $\sigma(\pm 4\Gamma)$

In this $M \pm 4\Gamma$ window I take only the Z' events ($N_{Z'}$):

$$N_{Z'} = N_{tot} \cdot \frac{\text{total surface - DY surface}}{\text{total surface}},$$

where the surfaces are determined as follows:

$$\begin{aligned} \text{total surface} &= N_{tot} l \\ \text{DY surface} &= \frac{d}{e} \cdot (\exp^{eB} - \exp^{eA}), \end{aligned}$$

where l is the dimension of a bin, and where A and B are the bin numbers corresponding to $M \pm 4\Gamma$. With α the acceptance[5] in $M \pm 4\Gamma$ of the selection,

$$\sigma_{ll} = \frac{N_{Z'}}{\alpha} \frac{1}{\mathcal{L}},$$

where the integrated luminosity $\mathcal{L}$ is known from generation from PYTHIA as shown above.
Errors ($\mathcal{L}$ given by PYTHIA is considered to be correct and Δe and Δd are known from the fit) are evaluated as follows:

$$\begin{aligned} \Delta^2\sigma &= \left(\frac{1}{\alpha\mathcal{L}}\right)^2 \Delta^2 N_{Z'} + \left(\frac{N_{Z'}}{\mathcal{L}\alpha^2}\right)^2 \Delta^2\alpha \\ \alpha &= \frac{N_{Z'}}{N_{init}} \rightarrow \Delta^2\alpha = \frac{\alpha(1-\alpha)}{N_{init}} \\ N_{Z'} &= N_{tot} - N_{DY} \rightarrow \Delta^2 N_{Z'} = \Delta^2 N_{tot} + \Delta^2 N_{DY} \\ \Delta^2 N_{tot} &= N_{tot} \quad \text{(counting error)} \end{aligned}$$

[5] Here at generation level is $\alpha = 1$ and $\Delta\alpha = 0$. However, the formulas are already shown for $\alpha \neq 1$ for later use in the chapter about full simulation.

$$N_{DY} = \frac{\text{DY surface}}{l} = \frac{1}{l}\frac{d}{e}(\exp^{eB} - \exp^{eA})$$
$$\rightarrow \Delta^2 N_{DY} = \left(\frac{d}{le}\cdot\left(B\exp^{eB} - A\exp^{eA}\right) - \frac{N_{DY}}{e}\right)^2 \Delta^2 e + \left(\frac{N_{DY}}{d}\right)^2 \Delta^2 d$$

The results are presented in table 7.2. A good agreement with the predictions from PYTHIA is achieved.

7.8. Leptonic cross section times decay width $\sigma_{ll} \cdot \Gamma$

To get the discriminating variable $\sigma_{ll} \cdot \Gamma$ the obtained values are multiplied, the results are presented in the same table as above. The error is calculated by $\Delta^2(\sigma\Gamma) = \Gamma^2\Delta^2\sigma + \sigma^2\Delta^2\Gamma$.

	σ(fb)	$\Gamma \cdot \sigma$(fb·GeV)	σ(fb) theory
SSM	76.93 ± 0.52	3532.48 ± 34.87	78.8
Z'_ψ	22.78 ± 0.13	181.63 ± 2.23	23.5
Z'_χ	46.68 ± 0.32	859.18 ± 8.31	47.9
Z'_η	25.94 ± 0.15	261.08 ± 2.85	26.3
LR	49.65 ± 0.51	1565.82 ± 19.03	50.0

Table 7.2.: *Results on σ and $\sigma \cdot \Gamma$*

7.9. Rapidity

The rapidity distribution is symmetric as one can see in figure 7.6(a) for the SSM model. It is shown for all models in figure 7.6(b). The rapidity distribution itself does not provide the possibility to discriminate between models. As mentioned in section 6.3.4 one has to analyze the relative parton distribution functions or the rapidity ratio.

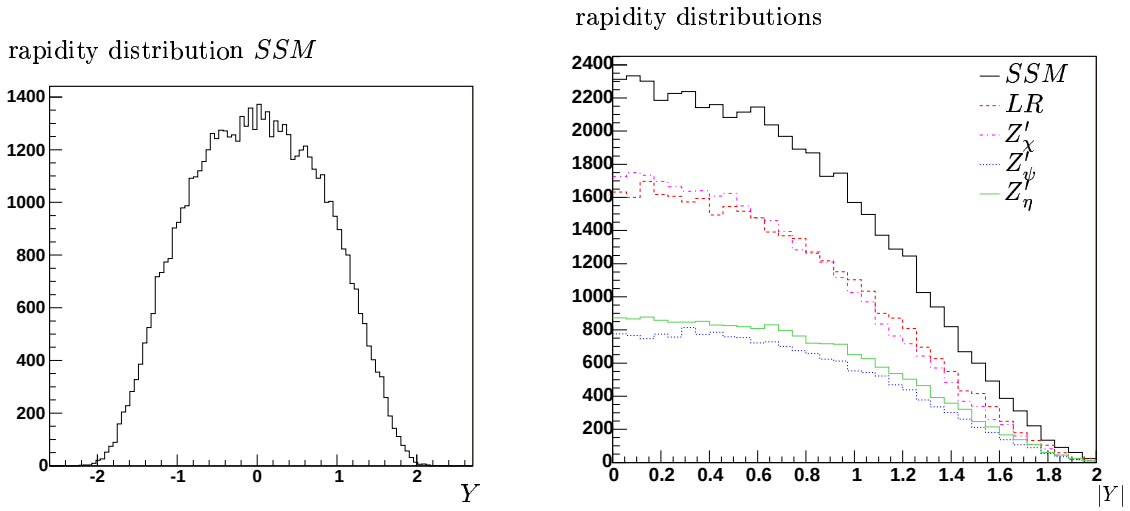

(a) SSM

(b) *all models, normalized on* $\int \mathcal{L}$.

Figure 7.6.: *Rapidity distributions*

7.10. Forward and backward direction

As it was mentioned in section 6.3.3, the forward and backward direction terms are defined according to the quark direction, which is approximated by the fastest one of the two participating quarks, i.e. the Z' direction.
Example: to produce a Z' at a given mass M we need in the center of mass an energy equal to $E = M = \sqrt{x\bar{x}s}$, with $s = \sqrt{14\,\mathrm{TeV}^2}$, $x(\bar{x})$ is the fraction of the momentum carried by the quark(antiquark), $x\bar{x} < 1$. To get an idea about the x and $\bar{x}$ values: for a symmetric collision ($x = \bar{x}$) and $M = 1.4\,\mathrm{TeV}$ one gets $x = 0.1$. Sea quarks exist only at low x (i.e. $\bar{x} < 0.1$). At high x only the valence quarks subsist. This means that the collision, for high Z' masses, is asymmetric ($x > \bar{x}$) and the produced boson is boosted in the quark-direction in most of the cases.

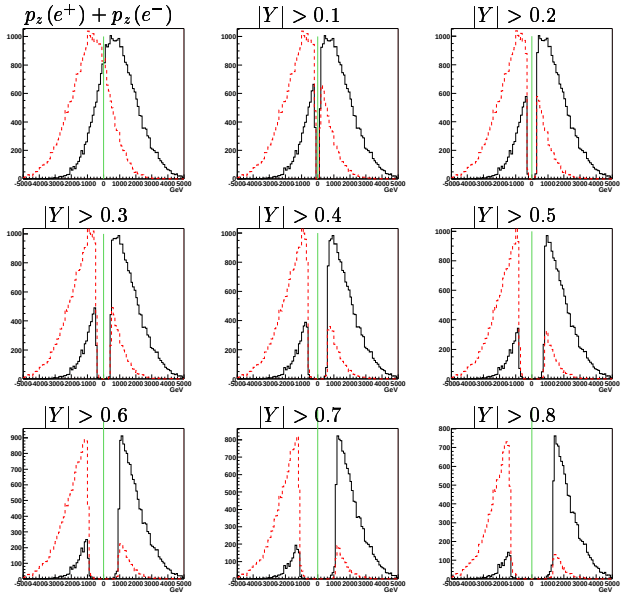

Figure 7.7.: *Study of the assignment of forward and backward (SSM) for different $|Y|$ cuts, for the legend see text.*

In figure 7.7, $p_Z(e^+) + p_Z(e^-)$ is histogrammed in black (solid line) for $p_Z(q) > 0$[6] and in red (dotted line) for $p_Z(q) < 0$. For the black histogram all events on the left side of the vertical line (the events with $p_Z(e^+) + p_Z(e^-) < 0$) are those where the approximation is wrong; for the red one those on the right side. From top/left to bottom/right a rapidity cut on the Z' is introduced and incremented in steps of 0.1. In table 7.3 the percentage of wrong quark direction is presented as a function of the rapidity cut for the SSM. This percentage is decreasing with an increasing cut.
In table 7.4 the percentage is presented for the different models without rapidity cut and with rapidity cut at 0.8, i.e. the quark direction and therewith the forward/backward definition is correctly approximated in 76% of the cases and in about 90% of the cases with a cut. So one possible idea is to use for the asymmetry study only events with high rapidity to get an *observed asymmetry* close to the *true asymmetry* without caring about this approximation.

no cut	$\|Y\| > 0.1$	$\|Y\| > 0.2$	$\|Y\| > 0.3$	$\|Y\| > 0.4$	$\|Y\| > 0.5$	$\|Y\| > 0.6$	$\|Y\| > 0.7$	$\|Y\| > 0.8$
24%	21%	19%	17%	16%	14%	12%	10%	9%

Table 7.3.: *Percentage of wrong quark direction with rapidity cuts, SSM, the statistical error is negligible*

In figure 7.8 the fraction ϵ of wrong quark direction assignment is shown as a function of the rapidity Y of the Z'. For $Y = 0$ (Z' at rest) the percentage is 50%. The function $\epsilon(Y)$ is modelised by a polynom of second degree for $\frac{d\epsilon}{dY} \geq 0$, and by $\epsilon = 0$ otherwise. Therefore a second possibility is to use this function to correct the *observed asymmetry* with a dilution factor.

[6] In this first step at generation level the quark momentum is known.

	SSM	Z'_ψ	Z'_η	Z'_χ	LR
all events	24%	23%	22%	27%	25%
with cut	9%	8%	8%	11%	10%

Table 7.4.: *Percentage of wrong quark direction without and with the cut* $|Y| > 0.8$*, all models, the statistical error is negligible*

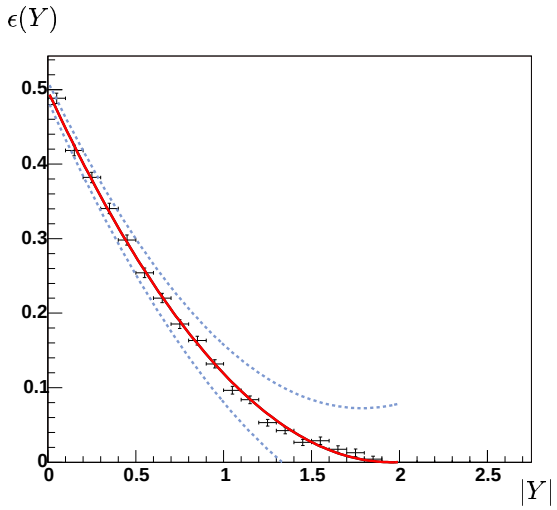

Figure 7.8.: *Ratio* $\epsilon(Y)$ *of wrong quark assignment for the SSM (fit in red/solid line, errors on the fit in blue/dashed line)*

7.11. $\cos\theta$ distributions

To determine $\cos\theta^{\star}$[7] and $\cos\theta^{\diamond}$[8] the quark and the electron have to be boosted into the Z' rest frame. This is done with the ROOT TLORENTZVECTOR-class. The Z' 4-momentum is the sum of the electron and positron 4-momentum. Electron and quark have to be boosted by $-\frac{\vec{p}(Z')}{E(Z')}$. The quark nearly never changes its direction (i.e. $p_Z(q)_{\text{lab}} \uparrow\uparrow p_Z(q)_{Z'}$).
$\cos\theta^{\star}$ $(\measuredangle(e^-, q)_{Z'})$ is calculated by

$$\cos\theta^{\star} = \frac{\vec{p}(e^-)_{Z'} \cdot \vec{p}(q)_{Z'}}{|\vec{p}(e^-)_{Z'}|\,|\vec{p}(q)_{Z'}|},$$

and $\cos\theta^{\diamond}$ $(\measuredangle(e^-, z)_{Z'})$ by

$$\cos\theta^{\diamond} = \frac{p_z(e^-)_{Z'}}{|p_z(e^-)_{Z'}|}.$$

In addition, I define θ^* as the same angle as $\theta^{\star}$, but in the case that the quark direction is only approximated:

$$\cos\theta^{*} = \frac{\vec{p}(e^-)_{Z'} \cdot \vec{p}(Z')_{\text{lab}}}{|\vec{p}(e^-)_{Z'}|\,|\vec{p}(Z')_{\text{lab}}|}.$$

The different distributions are shown for the Z'_χ model in figure 7.9(a). $\cos\theta^{\diamond}$ is symmetric as expected. $\cos\theta^{\star}$ is more or less asymmetric according to the asymmetry of the model. $\cos\theta^{*}$ follows $\cos\theta^{\star}$ but the asymmetry is diluted as the quark direction is not correctly approximated in a certain percentage of events.
In 7.9(b) for all models including the Drell-Yan the $\cos\theta^{\star}$ distributions are compared. Already without calculating asymmetries, the differences between the models are evident.

[7] angle between the e^+ and the q
[8] angle between the e^+ and the z-axis

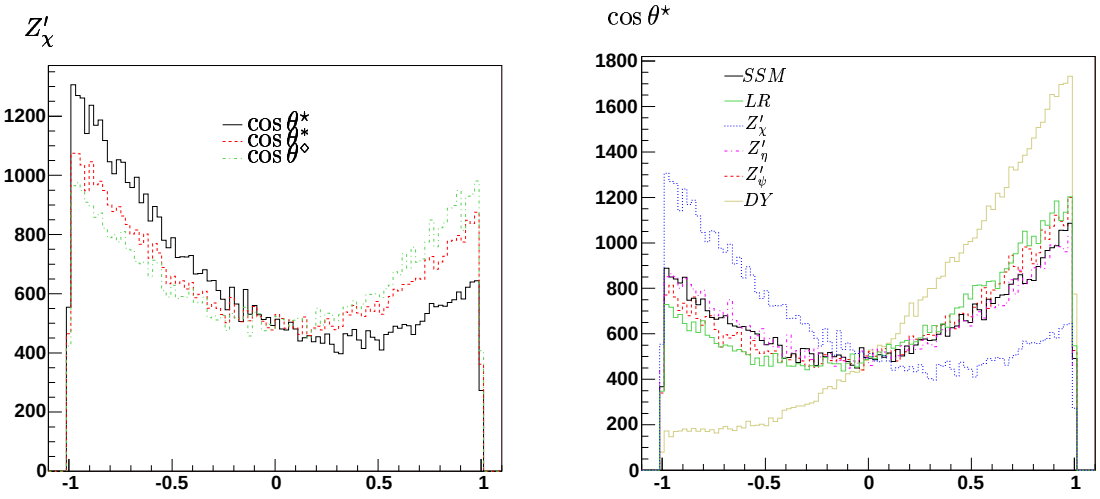

(a) $\cos\theta$ *distributions for the* Z'_χ *model*

(b) $\cos\theta^\star$ *distributions for all models*

Figure 7.9.: *Angular distributions*

7.12. $A_{FB}(M)$

As described in section 6.3.3 $A_{FB}(M)$ can be defined and determined in several ways:

- ⋆ with the Z' direction (*observed asymmetry*) ⟷ with the q direction (*true asymmetry*)
  - by fitting ⟷ by counting
  - with cut in $|Y|$ ⟷ without cut in $|Y|$
- ⋆ by introducing a dilution factor (*corrected asymmetry*, see section 7.12.4)

The different techniques with their limits and precisions are described in the next paragraphs.
I choose 5 equidistant bins (100 GeV) in M from 1250 GeV to 1750 GeV. The result of the bin around 1500 GeV is taken for the "on-peak asymmetry". The dimension of the bins was chosen as a compromise between estimated available statistics, the decay width of the boson and the effects of the detector resolution.
The effect of a cut in $|Y|$ is only studied as an example in one case, as later this method cannot be used as we will see in the chapter about analysis on full simulation. The low acceptance for events with high $|Y|$ impedes this. The effect of the ignorance of the quark direction is studied in several cases. In the section 7.12.4 this effect will be corrected by introducing a dilution factor.
Results are presented at the end of the section in the comparison paragraph.

7.12.1. ... by counting by formula 6.3

According to formula 6.3, $A_{FB}^{true}(M)$ is determined by

$$A_{FB}^{true} = \frac{N_+ - N_-}{N_+ + N_-},$$

where $N_\pm$ is the number of events with $\cos\theta^\star \gtrless 0$ in a bin of mass.

The results are presented in the figures of section 7.12.5 and will be commented there as well.
The error is calculated in the following way as N_+ and N_- are not independent: I use $\Delta^2\epsilon = \frac{\epsilon(1-\epsilon)}{N}$ for $\epsilon = \frac{n}{N}$, where n is a subset of N.

$$
\begin{aligned}
N &= N_+ + N_- \\
A_{FB}^{true} &= \frac{N_+ - N_-}{N_+ + N_-} = 2\frac{N_+}{N} - 1 \\
\rightarrow \Delta^2 A_{FB}^{true} &= 4\Delta^2(\frac{N_+}{N}) = 4\frac{N_+ \cdot N_-}{N^3}
\end{aligned}
$$

7.12.2. ... by counting by formula 6.4

In the same way, $A_{FB}^{obs}(M)$ is determined according to formula 6.4 by

$$A_{FB}^{obs} = \frac{N_+ - N_-}{N_+ + N_-},$$

where $N_\pm$ is the number of events with $\cos\theta^\diamond \cdot Y \gtrless 0$ in a M bin.
The result is presented in the figures of section 7.12.5 in magenta (◯).
This will not be used later in full simulation because the statistics available do not allow to correct $N_\pm$ by the acceptance, that in this case should be known as a function of Y and $\cos\theta$.
The errors are calculated in the same way as above.

$$\Delta^2 A_{FB}^{obs} = 4\frac{N_+ \cdot N_-}{N^3}.$$

7.12.3. ... by fitting

In each M-bin A_{FB}^{true} is determined by an unbinned fit[9] of

$$\frac{d\sigma}{d\cos\theta^\star} \propto \frac{3}{8}(1+\cos^2\theta^\star) + A_{FB}^{true}\cos\theta^\star$$

to the $\cos\theta^\star$ distribution, see figure 7.10 (black/solid line binned fit, color/dashed line unbinned fit). For the $\cos\theta^*$ distribution (approximation of the quark direction) I proceed in the same way.
The result of the fit is presented in the figures of section 7.12.5. The error is the error of the fit parameter from the unbinned fit.

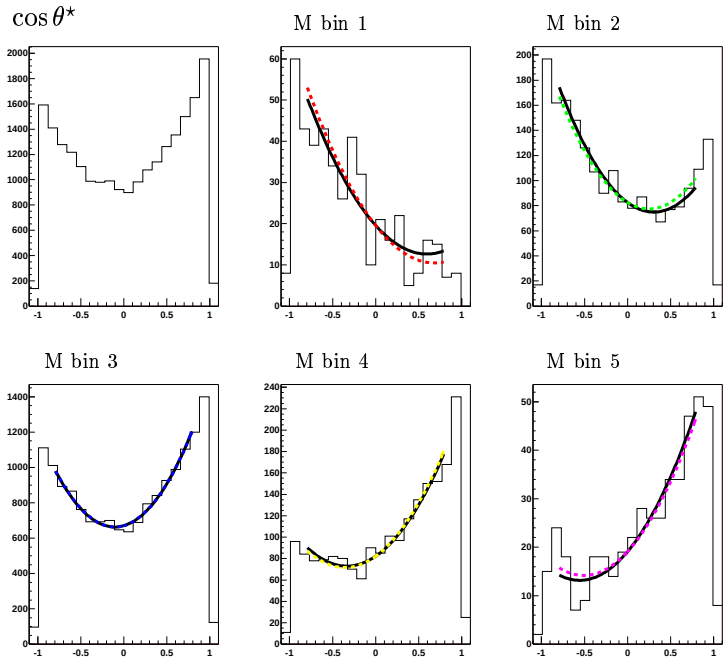

Figure 7.10.: $A_{FB}(M)$ *fit (black binned fit, colored unbinned fit)*

[9] The initial parameters are determined by a binned fit.

7.12.4. Dilution

In the case where one wants to correct the *observed asymmetry* A_{FB}^{obs} in order to recover as much as possible the *true asymmetry* A_{FB}^{true}, a dilution factor D must be introduced. If ϵ is the probability to chose the wrong quark direction, we have:

$$\begin{aligned} N_o^+ &= N_t^+(1-\epsilon) + \epsilon N_t^- \\ N_o^- &= N_t^-(1-\epsilon) + \epsilon N_t^+ \\ A^{true} &= \frac{N_t^+ - N_t^-}{N_t^+ - N_t^-} \\ A^{obs} &= \frac{N_o^+ - N_o^-}{N_o^+ - N_o^-} \\ &= (1-2\epsilon)A^{true} = D \cdot A^{true}, \end{aligned}$$

where $N_t^{\pm}$ is the number of events with $\cos\theta \gtrless 0$ in the case of the true angle (i.e. $\cos\theta^\star$, the angle with the quark direction). $N_o^{\pm}$ is the number of events in the case of the observed angle (i.e. $\cos\theta^*$, the angle with the Z' direction).
It was shown that a simple determination of a global dilution factor D is not possible. On the one hand it was tried to be determined by a simple division of the *observed* and *true* asymmetries in the Monte Carlo simulation in the different mass bins, on the other hand it was calculated by $1-2\epsilon$. It was shown that this "global" dilution factor depends of the mass range and above all it depends on the model, as ϵ depends on the mass range and the model. Besides, the first method has problems of instability in the case of asymmetries close to zero.

So the strategy of a two dimensional fit was adopted:

$$\begin{aligned} \frac{d\sigma}{d\cos\theta^\star} &\propto \frac{3}{8}(1+\cos^2\theta^\star) + A_{FB}^{true}\cos\theta^\star \\ \frac{d\sigma}{d\cos\theta^*} &\propto \frac{3}{8}(1+\cos^2\theta^*) + A_{FB}^{obs}\cos\theta^* \\ &= \frac{3}{8}(1+\cos^2\theta^*) + (1-2\epsilon(Y))A_{FB}^{true}\cos\theta^*, \end{aligned}$$

as $A_{FB}^{obs} = (1-2\epsilon(y))A_{FB}^{true}$ and ϵ depends on Y as it was discussed in 7.10. A two-dimensional fit is done to the $\cos\theta^*$ distribution and to the $\epsilon(Y)$ function that is parametrized as a polynomial of second degree.
The results (presented in 7.12.5) are quite satisfactory, the *true* asymmetry is well recovered. In the error bars besides the statistical error from the fit the systematic error from $\epsilon(Y)$ is included. It was estimated by varying the function $\epsilon(Y)$ within its error bars and by examining the $\epsilon(Y)$ functions obtained from the different models. The $\epsilon(Y)$ functions (unlike the mean ϵ value) is independent from the models - at least they are compatible within their error bars.

7.12.5. Comparison of the various determination techniques

Legend for the figures:

- $*$ black, fitting with quark direction
- ■ red, fitting with Z' direction
- □ blue, counting without cut and with the quark direction
- △ yellow, counting without cut and with the approximated quark direction
- ▲ blue, counting with cut and with the quark direction

▼ green, counting with cut and with the approximated quark direction

◯ magenta, counting (2^{nd} method)

The method by fitting and the two methods by counting lead nearly to the same result, fitting is a little better, in the sense that the errors are smaller. This is presented for the quark-direction case (without cut) for the SSM and for the Z' direction case (without cut) for the Z'_η model in figure 7.11.

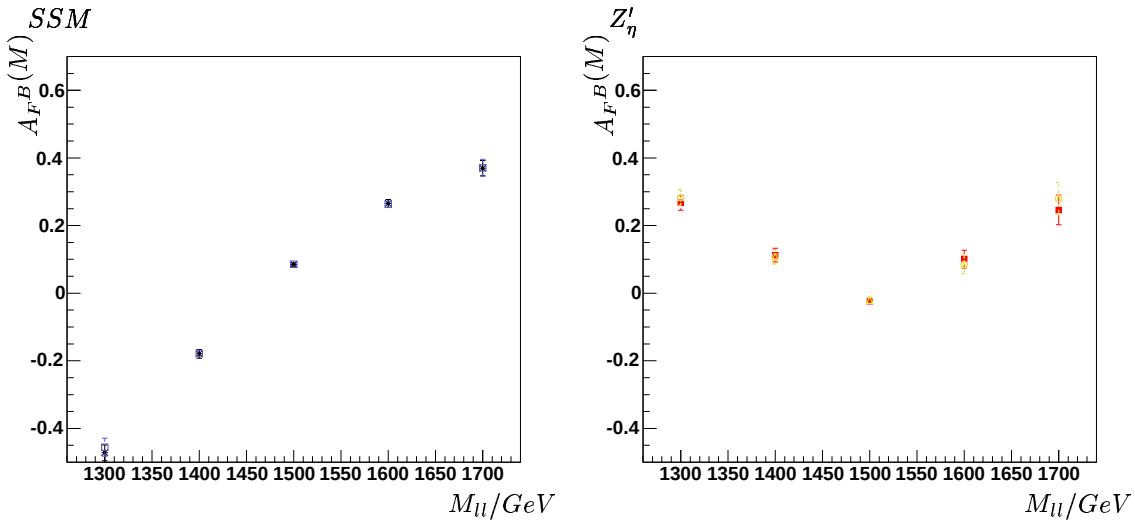

Figure 7.11.: *On the left side fitting and counting are compared in the case of the real quark direction, on the right side fitting and the 2 counting methods are compared in the case of the Z' direction. A_{FB} is shown in both cases as a function of the Z' mass in GeV. For the legend see text.*

One can see that approximating the quark direction dilutes the asymmetry: its absolute value is smaller in this case as it can bee seen in 7.12 for the LR model by fitting.
The effect is clearly higher without a cut in Y. This is also illustrated in figure 7.12 where counting with and without cut for the two cases true and approximated quark direction are compared (also for the LR model).

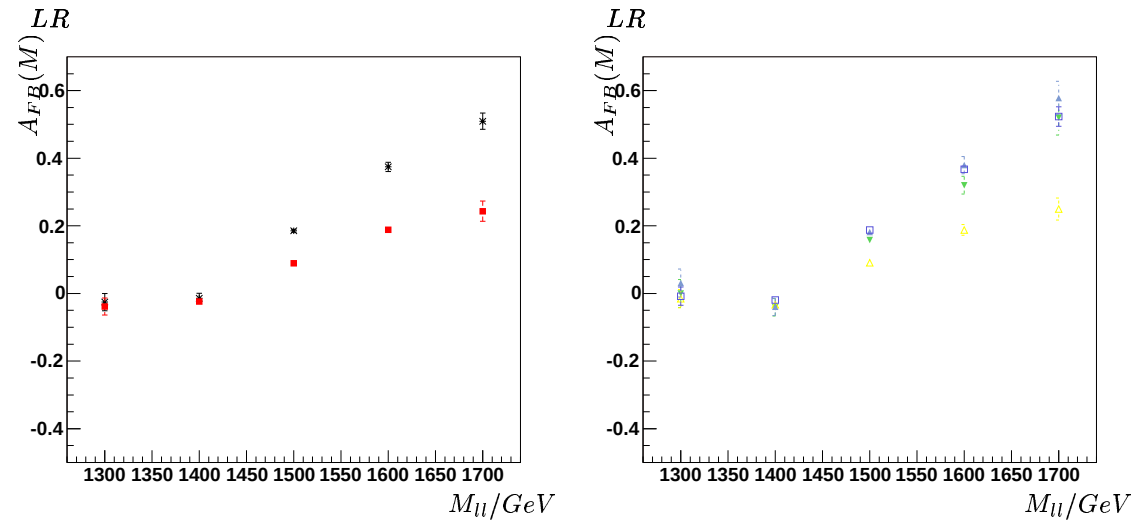

Figure 7.12.: *Effect of the approximation of the quark direction on the left side, on the right side effect of a rapidity cut in the cases quark direction and Z' direction. A_{FB} is shown as a function of the Z' mass in GeV. For the legend see text.*

In figure 7.13 the *true*, the *observed* and *corrected asymmetry* are compared for the SSM and the Z'_ψ. In both cases (determining the *observed asymmetry* or the *corrected asymmetry*) an asymmetry close to zero is difficult to determine precisely.
In all cases the on-peak errors are smaller as there is more statistics.

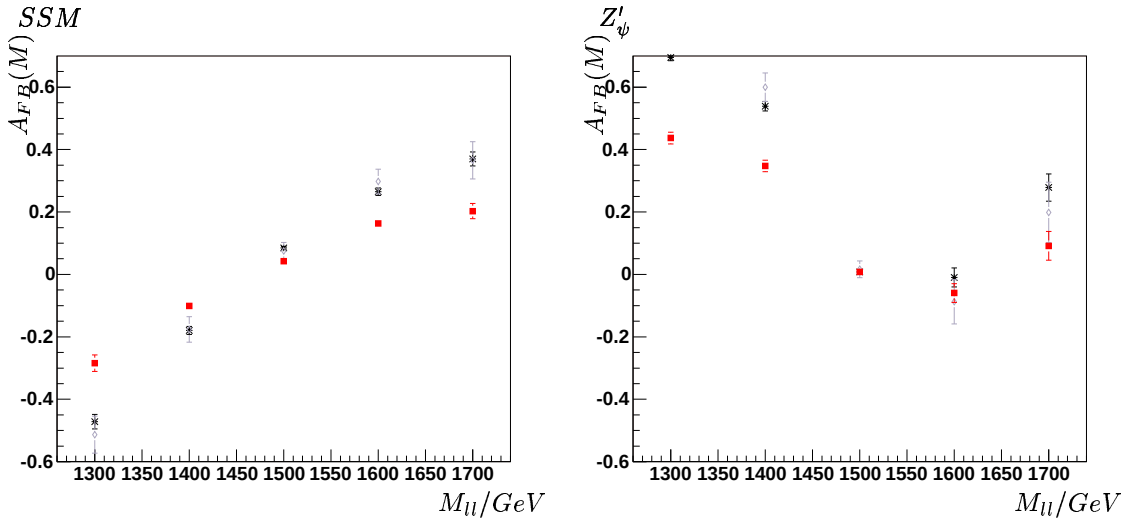

Figure 7.13.: *2 dimensional with a introduce a dilution factor.*
In black (∗) the true asymmetry, in red (■) the observed asymmetry and in gray (◊) the corrected asymmetry (result of the 2 dimensional fit).

Finally in figure 7.14 for all models the expected *true* (i.e. with the true quark direction) asymmetry is shown. In table 7.5, the on-peak values are given for several methods.
For validation purpose the results for the Drell-Yan were compared with the prediction published in [3]. Its asymmetry is constant at about 0.6. Additionally, the results are successfully compared to a similar analysis in [3] ($E6$, LR models and SSM) and in [17] (Z' of Kaluza-Klein).

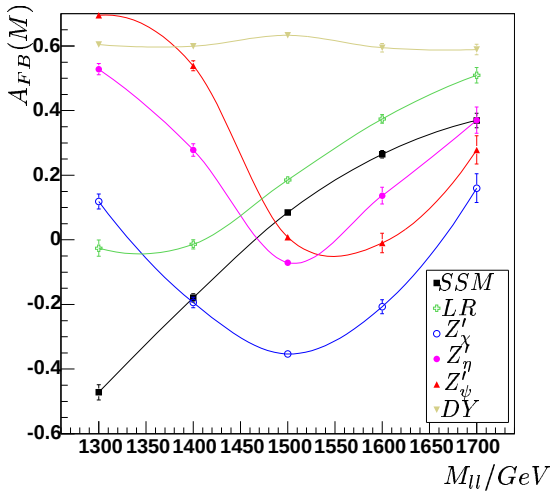

Figure 7.14.: $A_{FB}(M)$ *for the different models (by fitting, with the true quark direction)*

	fit 1D		counting		fit 2D
	$\angle(e^-, q)$	$\angle(e^-, Z')$	$\angle(e^-, q)$	$\angle(e^-, Z')$	
SSM	0.084 ± 0.004	0.042 ± 0.004	0.085 ± 0.005	0.042 ± 0.05	0.075 ± 0.027
Z'_ψ	0.008 ± 0.004	0.008 ± 0.004	0.009 ±0.005	0.007±0.005	0.016 ± 0.027
Z'_χ	-0.353 ± 0.004	-0.135 ± 0.004	-0.351±0.04	-0.133±0.005	-0.255 ± 0.027
Z'_η	-0.071 ± 0.004	-0.024 ± 0.004	-0.067±0.005	-0.021±0.005	-0.046 ± 0.027
LR	0.185 ± 0.004	0.090 ± 0.004	0.188±0.005	0.090±0.005	0.166 ± 0.027

Table 7.5.: *On-peak values for the different models for the different methods*

7.12.6. Off-peak asymmetry

The off-peak asymmetry is expected to provide some discrimination power as well. To have a first look at the off-peak asymmetry the *true asymmetry* was determined also for masses much lower than the peak. It is clear that the behavior of the $A_{FB}(M)$ curve gives more information than a mean value of the asymmetry in the off-peak region. To evaluate the behavior it is imperative to take into account the natural width. Indeed at values of mass where one is already off-peak for the Z'_ψ models, one is still on-peak for the Z'_{SSM}. So it was chosen to put on the axis not the leptonic mass in units of GeV, but the leptonic mass in units of Γ. In figure 7.15 one can see first the variation of the asymmetry as a function of M, scaled in GeV, and then scaled in units of Γ. The importance of the choice of the axis is clear.

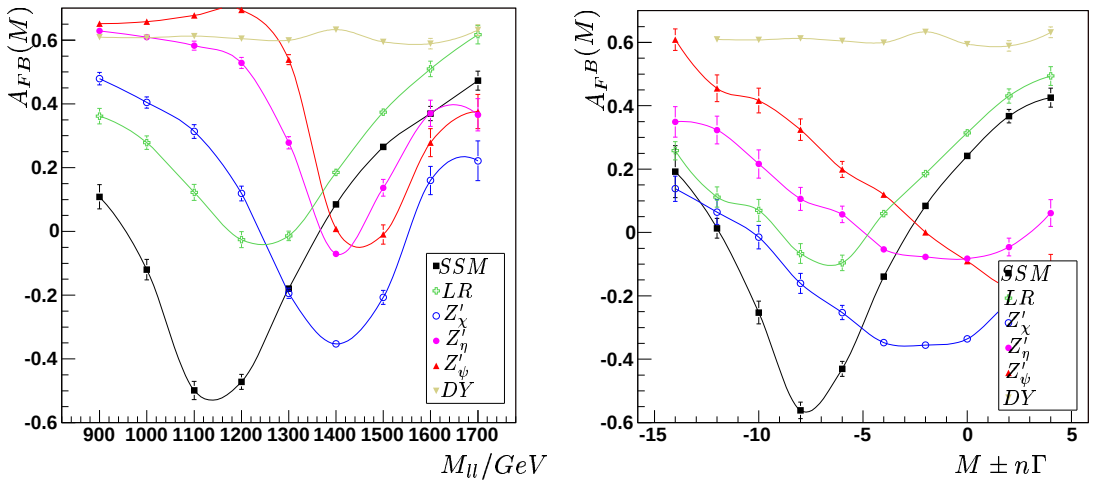

Figure 7.15.: *Off-peak asymmetry - different scales of the mass axis*

7.13. $A_{FB}(Y)$

According to section 6.3.3 $A_{FB}(Y)$ is determined by

$$A_{FB} = \frac{N_+ - N_-}{N_+ + N_-},$$

where $N_\pm$ is the number of events with $\cos\theta^\diamond \gtrless 0$ in a bin in Y and with a mass close to the peak are taken into account ($M \pm 30\,\text{GeV}$). I chose 10 equidistant bins from -2 to 2, as Y varies essentially from -2 to 2.
In figure 7.16 the results for all models are shown, they are in a good agreement with the predictions presented in 6.3.3. The graphs are all symmetric about $Y = 0$ and have quite different shapes.
The error-bars in the Y direction correspond to the chosen binning. The errors on the asymmetry are

calculated in the same way as for $A_{FB}(M)$:

$$\Delta^2 A_{FB} = 4\frac{N_+ \cdot N_-}{(N_+ + N_-)^3}.$$

It was chosen to characterize $A_{FB}(Y)$ by the slope of a straight line fitted to the 6 points of the 6 inner bins. The values are given in table 7.6.

SSM	0.07 ± 0.01
Z'_ψ	0.01 ± 0.01
Z'_χ	-0.22 ± 0.03
Z'_η	-0.04 ± 0.01
LR	0.16 ± 0.03
DY	0.52 ± 0.07

Table 7.6.: *Slope of* $A_{FB}(Y)$

7.14. Results at $M = 4$ TeV

7.14.1. Forward and backward direction

As shown in table 7.7 for the SSM the percentage of wrong quark direction assignment decreases with an increasing cut in $|Y|$ much faster than at 1.5 TeV. But, as the $|Y|$ themselves are smaller as well (not higher than 1.5), the total probability for wrong quark direction assignment does not change: it is about 24% (see table 7.8 for the different models). In contrast to 1.5 TeV this total probability is less dependent on the models. So at high enough mass one could perhaps determine a global dilution factor for the asymmetry. The Z'_{KK} is not different from the other models.

no cut	$\|Y\| > 0.1$	$\|Y\| > 0.2$	$\|Y\| > 0.3$	$\|Y\| > 0.4$	$\|Y\| > 0.5$	$\|Y\| > 0.6$	$\|Y\| > 0.7$	$\|Y\| > 0.8$
24%	20%	16%	12%	9%	7%	5%	3%	2%

Table 7.7.: *Percentage of wrong quark direction with rapidity cuts, SSM, the statistical error is negligible*

	SSM	Z'_ψ	Z'_η	Z'_χ	LR	KK
all events	24.0%	24.0%	24.5%	24.8%	24.6%	24.2%

Table 7.8.: *Percentage of wrong quark direction without cut in $|Y|$, all models, the statistical error is negligible*

The $\epsilon(Y)$ function is changing with the mass, but it remains independent of the models, including the Z'_{KK}.

7.14.2. Kinematics

The kinematic distributions are in agreement with those at 1.5 TeV, the ones of the Z'_{KK} do not differ either (see figure 7.17).

7.14.3. Interference

For the already studied models, the interference effects are the same as before. For the Z'_{KK} the effect of the destructive interference (figure 7.18) on the "left side" of the peak is quite impressive. In other popular KK models [17] the interference is constructive. Anyhow, the Z'_{KK} offers a good possibility to be discovered (or excluded) indirectly by studying possible deformations of the Drell-Yan.
We make in the KK case the approximation that there is no DY under the peak itself.

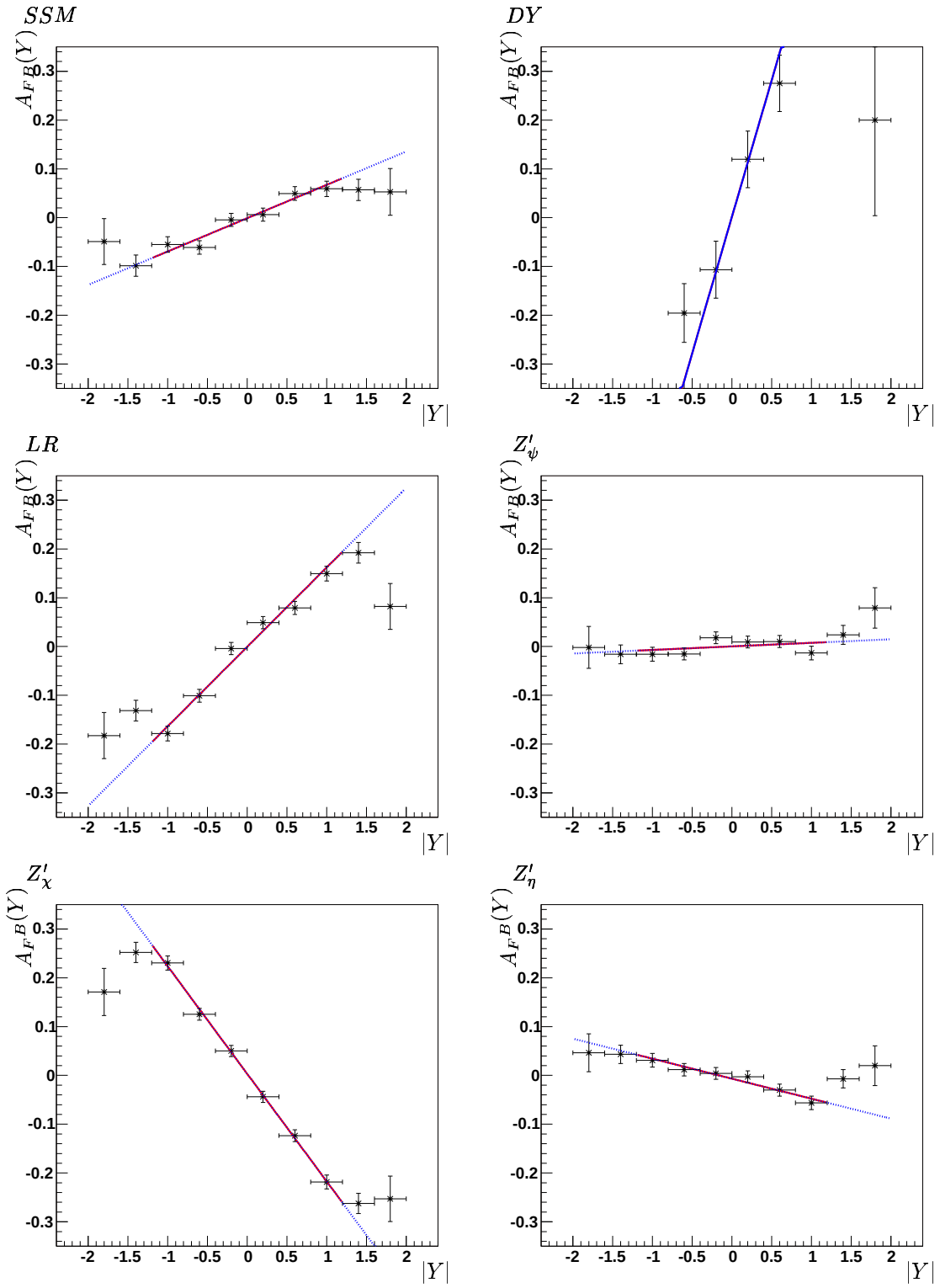

Figure 7.16.: $A_{FB}(Y)$ *for all models*

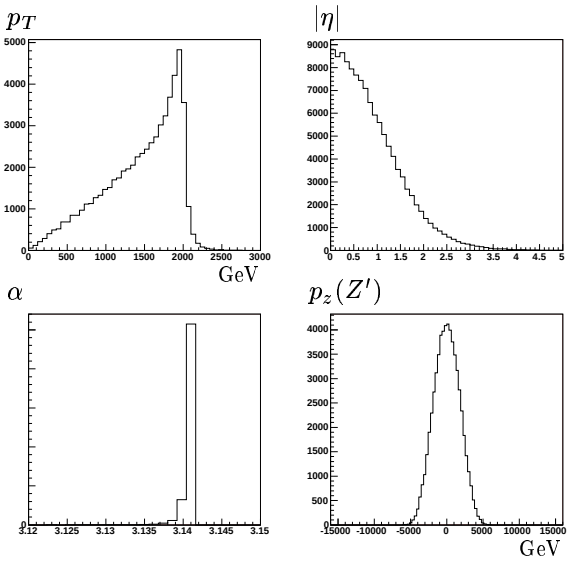

Figure 7.17.: *Kinematics for the KK model*

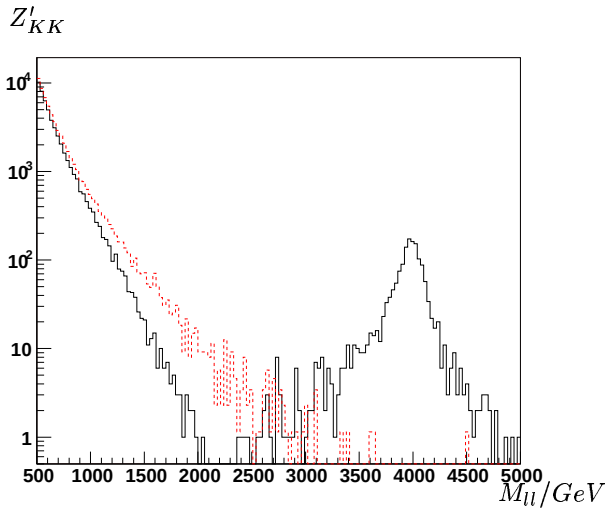

Figure 7.18.: *Interference for the Z'_{KK}*

7.14.4. Total decay width Γ

The same fit is used as at 1.5 TeV. For the Z'_{KK} no DY is added. The results of the fit are presented in table 7.9. The Z'_{KK} is much wider than the other ones.
At higher mass the fit is more sensitive to the input parameters (fit range, binning,...) and the systematic error is bigger. As at low mass, the decay width is always overestimated. This systematic error on the decay width grows with mass and decreases with the decay width. All distributions are shown superimposed in figure 7.19 (normalized by the integrated luminosity).
A deepened study of the DY and the effect of the interference will be necessary as the obtained fit results depend strongly on the parametrization of the DY. With a better understanding of the DY at this energy scale and the effect of interference this systematic error should be reduced.

7.14.5. Leptonic cross section σ_{ll}

The leptonic cross section is determined in the same way as before. The results are presented in table 7.10 and compared to the predictions from PYTHIA. $\Gamma \cdot \sigma$ is given as well. The Z'_{KK} has a cross-section

all models

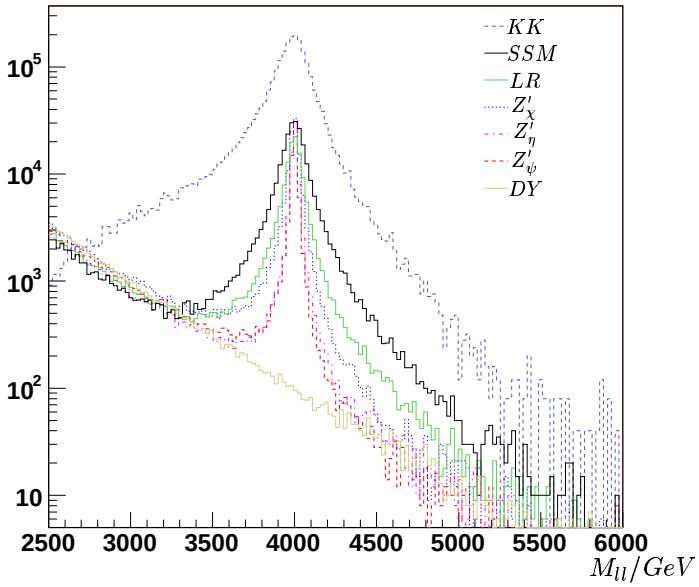

Figure 7.19.: *Resonance curve*

	M(GeV)	Γ(GeV)	Γ(theo.)(GeV)
SSM	3998.1 ± 0.4	121.9 ± 0.8	119.2
Z'_ψ	3998.5 ± 0.1	24.7 ± 0.3	21.2
Z'_η	3999.1 ± 0.1	30.0 ± 0.3	25.2
LR	3998.0 ± 0.3	88.0 ± 0.6	81.6
Z'_χ	3999.4 ± 0.2	51.1 ± 0.4	46.8
KK	3998.7 ± 0.6	180.0 ± 1.2	

Table 7.9.: *Decay width at 4 TeV*

10 times more important than the other ones. There are several possible explanations: the Z'_{KK} resonance contains the first resonance of the γ and of the Z, the γ couplings are different from the Z couplings and the couplings of the KK resonances are $\sqrt{2}$ higher than those of the SM.

	σ(fb)	$\Gamma \cdot \sigma$(fb·GeV)	σ(fb) theory
SSM	0.25 ± 0.001	30.67 ± 0.27	0.26
Z'_ψ	0.08 ± 0.0005	1.90 ± 0.03	0.08
Z'_χ	0.14 ± 0.0008	6.95 ± 0.07	0.13
Z'_η	0.09 ± 0.0005	2.69 ± 0.03	0.09
LR	0.16 ± 0.001	13.95 ± 0.14	0.16
KK	2.30 ± 0.01	415.18 ± 3.18	2.3

Table 7.10.: *Results on σ and $\sigma \cdot \Gamma$*

7.14.6. $A_{FB}(M)$

For the study of the asymmetry and above all the $\cos\theta$ distributions only events with $M > 3.5$ TeV are taken into account, otherwise the asymmetry of the DY dominates. 200 GeV was chosen for the size of the bins in M. In figure 7.20 the different $\cos\theta^\star$ distributions are shown. The distribution of the Z'_{KK} is quite similar to the one of the DY.

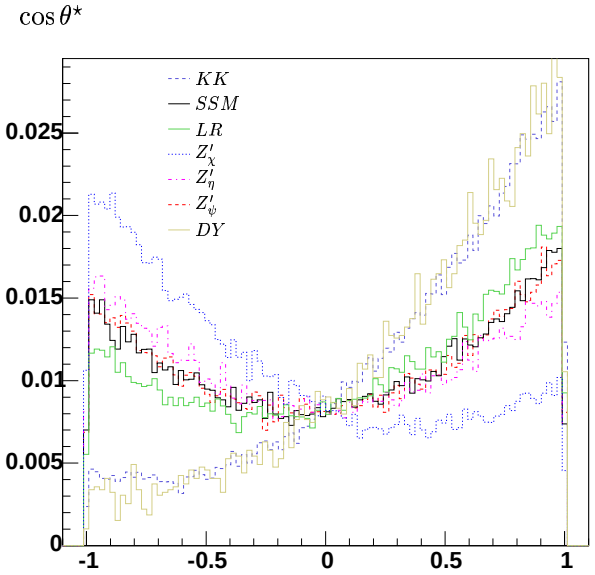

Figure 7.20.: $\cos\theta^\star$ *distributions for all models*

The different *true asymmetries* are shown in figure 7.21. They are quite similar to the ones at 1.5 TeV. $A_{FB}(M)$ of the Z'_{KK} is constant as well as the one of the DY at about 0.6. The characteristic dip at the peak mass can be seen.

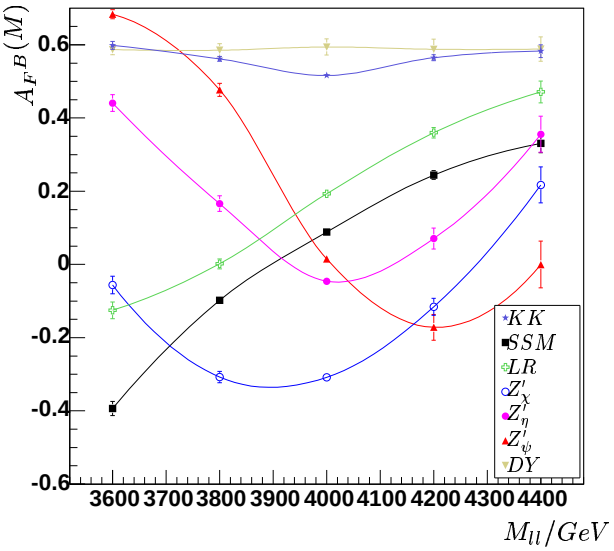

Figure 7.21.: $A_{FB}(M)$ *for the different models (by fitting, with the true quark direction)*

The results for the *true asymmetry*, the *observed asymmetry* and the *corrected asymmetry* are shown in table 7.11, all values are the on-peak asymmetries.

7.14.7. $A_{FB}(Y)$

Events in $M \pm 80$ GeV are taken into account. The results for the slopes are presented in table 7.12. Once more the Z'_{KK} (figure 7.22) is quite similar to the DY, this is probably due to the contribution of the γ'.

	fit 1D		fit 2D
	$\angle(e^-, q)$	$\angle(e^-, Z')$	
SSM	0.09 ± 0.01	0.04 ± 0.004	0.09 ± 0.03
Z'_ψ	0.01 ± 0.01	0.00 ± 0.005	-0.01 ± 0.03
Z'_χ	-0.31 ± 0.01	-0.15 ± 0.005	-0.26 ± 0.03
Z'_η	0.05 ± 0.01	-0.02 ± 0.005	0.04 ± 0.03
LR	0.19 ± 0.01	0.09 ± 0.005	0.16 ± 0.03
KK	0.52 ± 0.01	0.27 ± 0.005	0.47 ± 0.03

Table 7.11.: *On-peak asymmetries for all models at 4 TeV*

SSM	0.15 ± 0.03
Z'_ψ	-0.02 ± 0.02
Z'_χ	-0.49 ± 0.06
Z'_η	-0.06 ± 0.02
LR	0.28 ± 0.04
KK	0.84 ± 0.01
DY	0.82 ± 0.16

Table 7.12.: *Slope of* $A_{FB}(Y)$

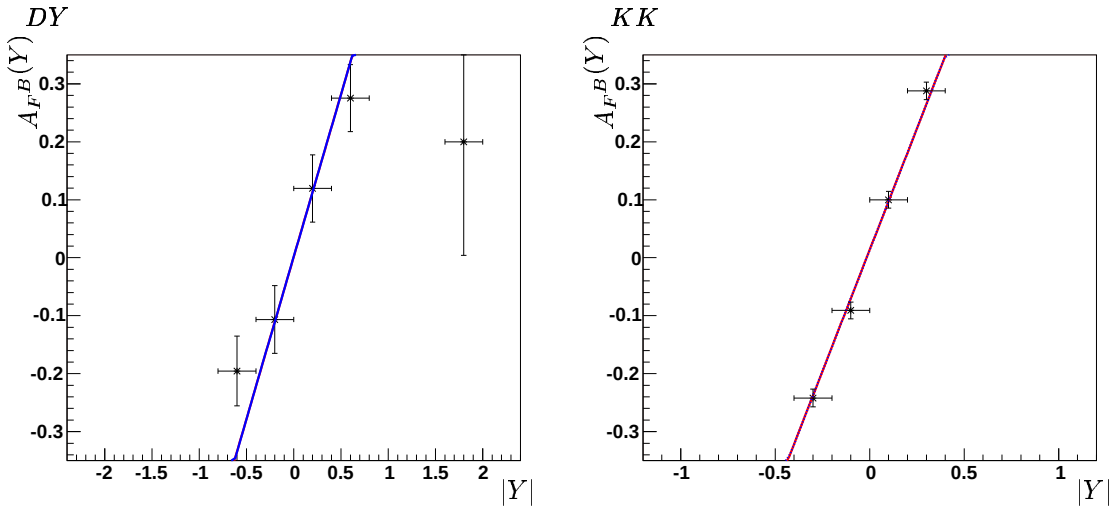

Figure 7.22.: $A_{FB}(Y)$ *for the the* Z'_{KK} *and the* DY

7.14.8. Z'_{KK} special case

As a cross-check the Z'_{KK} was studied very briefly at $M = 1.5\,\text{TeV}$. As for the other models the asymmetries are varying only very slowly in mass. For the decay width $\Gamma = 66.51 \pm 0.40\,\text{GeV}$ was found, what is perfectly in agreement with $\Gamma \propto M$. The cross-section is about $615 \pm 2.6\,\text{fb}$, this corresponds to more than 30 evts/day at low luminosity.

In fact, the decay width determined in this way for the Z'_{KK} is the "effective" decay width of the first photon and the first Z resonance, as they are nearly degenerated in mass. In another step it was tried to study the decay width of both resonances separately, i.e. a fit to the mass distribution by a sum of two Breit-Wigner functions (multiplied by an exponential for the parton luminosity and peak deformation) was done. The hypothesis that the ratio of $\frac{\Gamma(\gamma^{(n)})}{\Gamma(Z'^{(n)})}$ is constant an known was made.

In the used generator we have at $M = 4\,\text{TeV}$ $\Gamma(\gamma^{(1)}) = 169.7\,\text{GeV}$ and $\Gamma(Z'^{(1)}) = 242.0\,\text{GeV}$. By fitting (figure 7.23) $\Gamma(\gamma^{(1)}) = 166.3 \pm 1.4\,\text{GeV}$ and $\Gamma(Z'^{(1)}) = 236.2 \pm 2.0\,\text{GeV}$ was found.

Nevertheless, one has to be careful with this view as there is an important interference between the Z and γ resonances which is totally neglected in this approach.

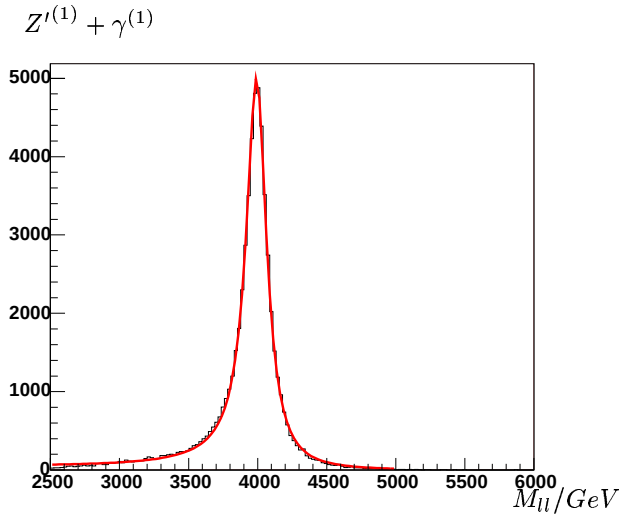

Figure 7.23.: *Fitting the Z' mass distribution*

7.15. Conclusions

The different discriminating variables have been studied, i.e. the total decay width, the leptonic cross-section and the asymmetries.
The total decay width is affected by a systematic error that increases with mass and decreases with the decay width. A better understanding of the DY at this energy scale as well as of the interference and the parton luminosity are needed to parametrize better the invariant leptonic mass distribution. In [52] it was already shown that different generators (PYTHIA and HERWIG) lead to the same results for the DY in the energy range up to 4 TeV. The multiplicative exponential that cares about parton luminosity and peak deformation by interference has to be studied better as well. Nevertheless the more complicated function $BW \cdot exp + exp$ improves the result compared to a simple BW function. The decay width grows proportionally to the mass.
The cross-sections are in a good agreement with the predictions from PYTHIA. The cross-section of the Z'_{KK} is one order of magnitude higher than the one of the other models.
The asymmetry was studied on the one hand as a function of the mass of the Z' boson. Several methods are in a good agreement for the *observed* and the *true asymmetry*. With the help of a dilution factor the *true asymmetry* can be approximately recovered. A more deepened study of $\epsilon(Y)$ (the probability of wrong quark direction assignment) is needed to improve these results.
On the other hand the asymmetry was studied as a function of the rapidity of the Z' boson. $A_{FB}(Y)$ is symmetric around the origin. It was decided to characterize $A_{FB}(Y)$ by the slope of a straight line fitted to the bins at low $|Y|$.
Both asymmetries are varying only slowly with the mass of the Z' boson.

8. Physical background

As physical background all signals with the e^+e^- signature have to be considered, as well as all processes including an electron(positron) and a photon since photons can be misidentified as electrons. There are the following processes:

- ⋆ **Drell-Yan** $Z/\gamma \rightarrow e^+e^-$, this process can never be separated from the signal and it is always included with the complete interference structure in the simulations that have been performed.
- ⋆ $\boldsymbol{ZZ} \rightarrow e^+e^-e^+e^-$, two combinations of electrons with opposite charge can be misidentified as a Z'.
- ⋆ $\boldsymbol{ZW^{\pm}} \rightarrow e^+e^-e^{\pm}\nu$, the electron from the W with an electron from the Z with the opposite charge can be misidentified as a Z'.
- ⋆ $\boldsymbol{W^+W^-} \rightarrow e^+\nu e^-\bar{\nu}$.
- ⋆ $\boldsymbol{Z\gamma} \rightarrow e^+e^-\gamma$, in the case of a misidentification of the photon as an electron.
- ⋆ $\boldsymbol{W^{\pm}\gamma} \rightarrow e^{\pm}\nu\gamma$.
- ⋆ $\boldsymbol{t\bar{t}} \rightarrow W^+bW^-\bar{b} \rightarrow e^+\nu e^-\bar{\nu}X$.
- ⋆ $\boldsymbol{b\bar{b}} \rightarrow e^+\nu e^-\bar{\nu}X$

The $b\bar{b}$ case can be excluded by kinematic considerations. In figure 8.1 the transverse momentum of muons of the process $b\bar{b} \rightarrow \mu X$[1] is shown. The distribution of electrons would be the same. As it was shown in chapter 7.2, the p_T from electrons from Z' decays is nearly always higher than 50 GeV, while the p_T from $b\bar{b}$ are always lower than 30 GeV. Thus, the $b\bar{b}$ background is eliminated by a cut in p_T.

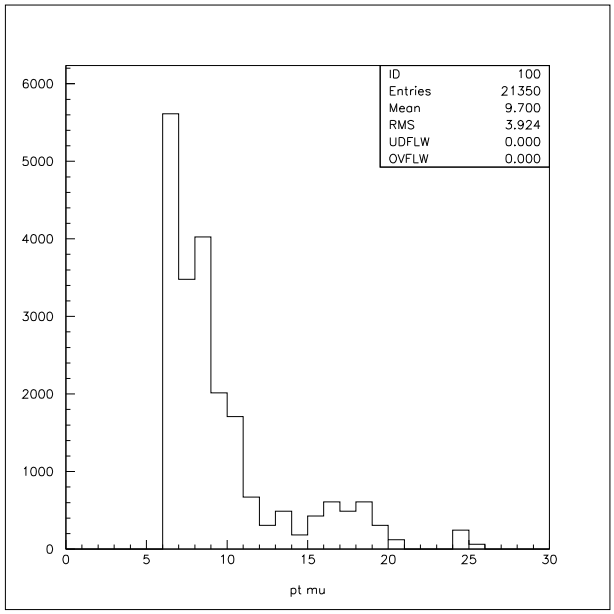

Figure 8.1.: *Transverse momentum of muons from* $b\bar{b} \rightarrow \mu X$

In principle, the $Z' + DY \rightarrow \tau^+\tau^-$ process has to be considered as well, since a τ decays in 17% of the cases into an electron and neutrinos. This produces some additional background and a deformation of the DY background shape. Nevertheless it should be rather negligible because of the low branching

[1] Shown are decays of the $b\bar{b}$ pair with at least one muon of at least 6 GeV.

ratio and because a selection criteria on the angle between the two electrons (which will be applied later) should be very efficient in removing it.

In the next sections I will give the cross-sections and the number of expected events (without any selection) at fixed integrated luminosity for the different backgrounds and compare them to the Drell-Yan.

8.1. Cross sections around $M = 1.5$ TeV and $M = 4$ TeV

In figure 8.2(a) the expected number of events as a function of the reconstructed di-lepton mass is presented for the different processes, normalized to $\int \mathcal{L} = 100\, fb^{-1}$ for M around 1.5 TeV. The number of possible combinations to build a di-lepton pair is considered. In table 8.1 the different cross-sections obtained from PYTHIA are given (20 000 events and cut in center-of-mass energy 1 TeV, the decay is forced to e^+e^-X or $e^\pm\gamma X$). Even if these cross-sections are sometimes higher or of the same order than the DY-one, the number of events in the considered mass-range is always smaller, except the $W\gamma$. Including the photon-rejection of about 95% also this background will be negligible (see photon-electron seperation in section 9.1.2).

process	cross-section (mbarn)
DY	$6.59 \cdot 10^{-12}$
$W\ \gamma$	$2.03 \cdot 10^{-11}$
ZZ	$9.45 \cdot 10^{-14}$
WW	$5.83 \cdot 10^{-12}$
$Z\ \gamma$	$3.93 \cdot 10^{-12}$
ZW	$1.16 \cdot 10^{-12}$
$t\bar{t}$	$1.83 \cdot 10^{-11}$

Table 8.1.: PYTHIA *cross-section with a cut at 1 TeV on the center of mass energy*

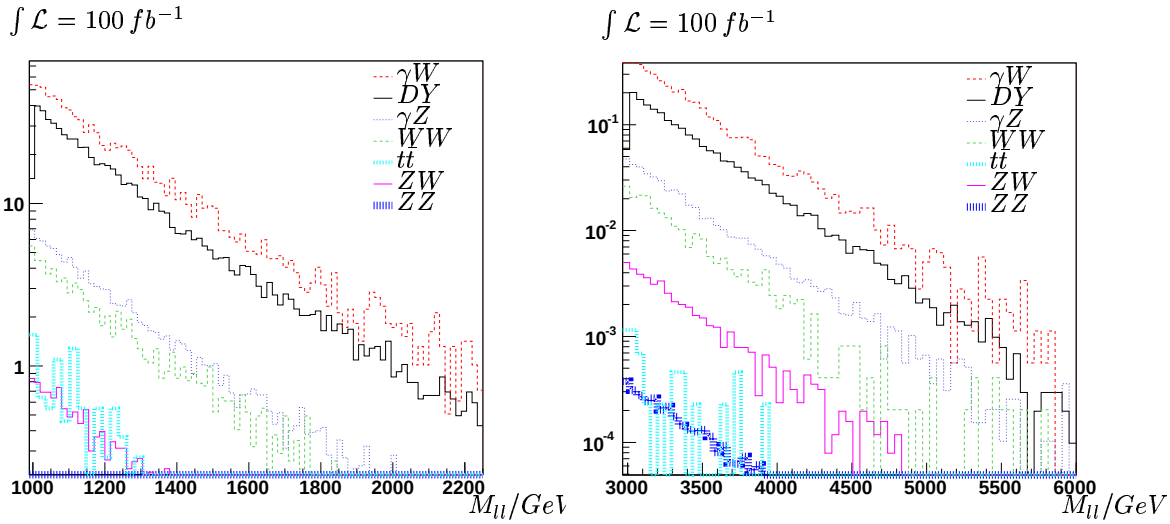

(a) *around $M = 1.5$ TeV*

(b) *around $M = 4$ TeV.*

Figure 8.2.: *Background*

In figure 8.2(b) the same for M = around 4 TeV. The gap between "signal" (i.e. the DY) and the background decreases, but remains quite large.

8.2. Expected events and significance

In table 8.2 the number of expected Z' events and the significance $\frac{S}{\sqrt{B}}$ are shown in the window $M \pm 4\Gamma$. As background only the Drell-Yan is considered. The results are given for $20\,fb^{-1}$, i.e. one year of data taking at low luminosity at $M = 1.5\,\text{TeV}$. The values are given for an (non-realistic) acceptance α of 1, and for an estimated acceptance of 0.4.
The cross-sections for the DY are varying from one model to another as cross-sections mentioned in the table are the ones in the interval $M \pm 4\Gamma$.

	$\sigma_{Z'}(fb)$	$\sigma_{DY}(fb)$	evts Z'	evts DY	$\frac{S}{\sqrt{B}}$, $20\,fb^{-1}$	
			$20\,fb^{-1}$	$20\,fb^{-1}$	$\alpha = 1$	$\alpha = 0.4$
SSM	76.9	0.64	1538	13	426	269
Z'_ψ	22.8	0.22	456	4	228	144
Z'_χ	46.7	0.60	934	60	270	171
Z'_η	25.9	0.29	518	29	211	133
LR	50.2	1.06	1004	106	219	139

Table 8.2.: *Expected events and significance, $M = 1.5\ TeV$*

Already after one year of data taking at low luminosity even with a worse acceptance a Z' boson at $M = 1.5\,\text{TeV}$ would be discovered in all models.
In table 8.3 the same calculation is made for the case of $M = 4\,\text{TeV}$. Here one year of high luminosity ($100\,fb^{-1}$) is taken. Also in this case the Z' boson would be discovered in all models.

	$\sigma_{Z'}(fb)$	$\sigma_{DY}(fb)$	evts Z'	evts DY	$\frac{S}{\sqrt{B}}$, $100\,fb^{-1}$	
			$100\,fb^{-1}$	$100\,fb^{-1}$	$\alpha = 1$	$\alpha = 0.4$
SSM	0.25	0.003	25	0.3	46	29
Z'_ψ	0.10	0.001	10	0.1	32	20
Z'_χ	0.14	0.002	14	0.2	31	20
Z'_η	0.10	0.001	10	0.1	32	20
LR	0.16	0.003	16	0.3	29	18
KK	2.3	–	230	–	–	–

Table 8.3.: *Expected events and significance, $M = 4\ TeV$*

8.3. Summary

The $Z' \to e^+e^-$ channel is extremely clean, all backgrounds are nearly negligible compared to the Drell-Yan. The number of such background events for all processes except the Drell-Yan is estimated to less than one third of Drell-Yan events in the peak region. At 4 TeV compared to 1.5 TeV the background increases in importance but not enough to become non negligible.
Not evaluated here are dijets mis-tagged as electrons. If we wanted to study the other leptonic channels, for the muon channel cosmics would have to be considered and the tau channel would be the most difficult to extract from background.

9. Full simulation

As before, the events are generated with PYTHIA. The cut in center-of-mass energy was reduced to 500 GeV for the case of a 1.5 TeV Z' (and to 2 TeV for a 4 TeV Z') in order to keep as much information as possible on the Drell-Yan and the interference. For the Z'_{KK} it was even decreased to 1 TeV. We chose to generate 100 fb^{-1} for the SSM and for the other models the integrated luminosity necessary for the same number of events (10 000) in the peak-region in the case of $M = 1.5$ TeV. In the 4 TeV case, the SSM and the KK are studied with a smaller number of events. In table 9.1 the integrated luminosities are presented. Pure DY was also generated. ISR and FSR were included to be as realistic as possible.
The simulation was made at CERN in the framework of DC1 (Data Challenge 1 [53] with GEANT 3 [54], ATHENA version 7.0.0). In DC1 for the first time $\sim 10^7$ events were generated and simulated in laboratories around the world. Reconstruction was done within ATHENA (version 7.0.2), without electronic noise.
No pile-up was included, but the final detector layout was used. There is a certain ambiguity: to discriminate between the models and even to discover high mass extra gauge bosons, high luminosity will be needed. But pile-up was not yet available for the full-simulation at the moment where the simulations were done. So my work had to be done in the low luminosity scenario - even if the present analysis is not realistic in a low luminosity scenario and has to be redone once the high luminosity simulation will be available.

		$\int \mathcal{L}(fb^{-1})$
$M = 1.5$ TeV	SSM	122
	Z'_ψ	321
	Z'_χ	131
	Z'_η	312
	LR	135
$M = 4$ TeV	SSM	30371
	KK	517

Table 9.1.: *Integrated luminosity in full simulation*

9.1. Identification of isolated electrons

9.1.1. Isolation

The Z' electrons and positrons are expected to be isolated. This is indeed what we observe in figure 9.1, in which the distributions of the distance and transverse energy of the closest cluster with $E_T > 40$ GeV of Z' electrons are shown. The peak at 3.1 in distance is the other electron. The two peaks in transverse energies are also the second electron, either at around 750 GeV for Z' events or at around 250 GeV for DY events.
As a first approximation, without having studied background or electronic noise, an electron will be defined as *isolated* if the closest cluster with $E_T > 40$ GeV is not closer than $d = 0.5$[1]. As the signal distribution in distance is flat, this radius can be adapted later to the background.

9.1.2. Identification

Isolated electrons are easy to identify (contrarily to electrons in jets).
Only clusters with a transverse energy higher than 50 GeV are taken into account.

In the electromagnetic calorimeter electrons have to be separated from jets and photons. The preliminary electron identification variable of ATHENA 'ISEM' is used [55] - even if it is optimized to low energy

[1] The distance d is defined as $d = \sqrt{\Delta\phi^2 + \Delta\eta^2}$.

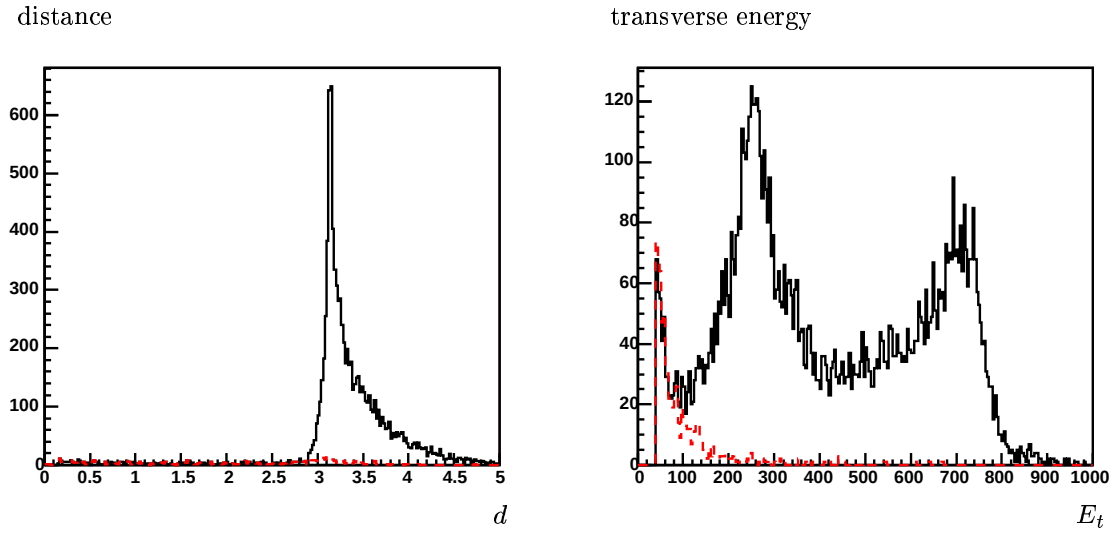

(a) distance to the closest cluster

(b) its transverse energy (a cut at 40 GeV is applied)

Figure 9.1.: *in black/solid line the closest cluster, in red/dashed line the closest cluster that is not the other lepton*

electrons, but it seems to work quite fine. This variable includes criteria on the shower shape and on the energy leakage in the hadronic calorimeter. At least one matched track in the inner detector is required. In addition isolated tracks are required: i.e. not more than one extra-track in a broad window (0.05 in η and 0.1 in ϕ) around the chosen track. To reject photons a good track quality is required, i.e. a high total number of hits (≥ 6) in pixels.
Other proposed separation criteria as $\frac{E(calo)}{p(tracking)} \sim 1$ for electrons, $\Delta\phi$ and $\Delta\eta$ small between the calorimeter and the tracker are not used, as they reject too much electrons at high p_T. Furthermore a good alignment between the tracker and the calo will only be possible after some years of running and not in the first years where hopefully a Z' boson would be discovered.
For this study I used available single electron, single photon and dijet samples from the DC1 production, in each case the samples with the most appropriate energy range.

As the $Z' \rightarrow e^+e^-$ channel is a very clean signal without much background, efficiency on electrons can be kept maximum, which is also interesting in the Z' case in which 2 electrons are required.

As later in the section about calibration, I am presenting here only provisional ideas until these points are included in a common way in ATHENA. Indeed this topic is not the goal of my work, I only finalized some straight-forward solutions without perfecting or optimizing efficiency, for example without trying to recover electrons without tracks,... All these points have to be covered later in a more detailed way.

Electron - jet separation

Jets form contrarily to electrons or photons several clusters in the electromagnetic calorimeter. So one has to separate the electron cluster from the different jet clusters. The jet efficiency will be defined with respect to the total number of jet clusters.
Most of the jet clusters are rejected by the variable 'ISEM' or the track isolation criteria. Most of the electrons that are lost are lost by the track isolation criteria.

Electron - photon separation

As well as electrons, photons usually form only one cluster, the efficiency is therefore normalized on the total number of photons.
For photon rejection the most important criteria is the requirement of at least one matched track. The

criteria on the quality of the track improves this. The variable 'ISEM' does not allow very well to separate electrons from photons as the showers are quite similar.

Efficiencies

In table 9.2 the efficiencies are presented. The jet and photon rejection seem to be sufficient in view of the little background, the electron efficiency of about 90% allows a good enough acceptance given the high cross section of the Z' signal.

single electrons 200 GeV	91%
single electrons 1 TeV	87%
single photons 200 GeV	4 %
dijets 560 GeV	0.13%

Table 9.2.: *Electron identification: efficiencies*

9.2. Electron energy calibration

9.2.1. Electromagnetic calibration in ATHENA

The total reconstructed energy in the electromagnetic calorimeter in ATLAS is proposed in the TDR 'Calorimeter Performance' to be calculated in the following way:

$$E_{tot} = w_{glob}(w_{ps}E_{ps} + E_{strips} + E_{middle} + E_{back}), \tag{9.1}$$

where w_{glob} is a global calibration factor and $E_{ps}, E_{strips}, E_{middle}, E_{back}$ are the energies measured in a given cluster of cells in the presampler, strip layer, middle and back samplings of the calorimeter respectively and w_{ps} is the presampler weight. The presampler is used where available to correct for the energy lost in the upstream material. The strip section provides information on the early part of the shower, besides contributing the energy measurement. Most of the shower energy, however, is deposited in the middle sampling. It is assumed that the energy is already converted from μA to GeV. The goal is to optimize the energy resolution.[2] Further corrections must be applied: η and ϕ modulations, out of cone corrections (amount of energy out of the box defining the cluster).
However, the calibration is done at present in two steps (see [56] and references therein). Starting from the cell energy deposited in the liquid Argon per layer ($e_{0,1,2,3}$), the cell level calibration is applied: $E_k = \Omega w_k e_k$, where Ω is a scale factor and the w_k's are the longitudinal weights for material and leakage corrections of the 4 layers k. In a second step, cluster level corrections are applied: cluster position corrections (S-shape, ϕ-offset) and cluster energy corrections (ϕ/η modulations, out of cone corrections, barrel/endcap crack). The total energy reads

$$E_{rec} = \sum_{\text{cells } j, \text{layers } l} w_l E_l^j.$$

The longitudinal weights are determined from photon test-beams by optimization of the resolution and fixing w_1 to one. Ω is then calculated indirectly from the beam energy. The cluster corrections are optimized on photons as well.
So for electrons one has for the moment to "de-calibrate" and to "re-calibrate" [56] at cluster-level. Of course this procedure is only a tide-over until separate photon and electron calibration will be implemented in ATHENA.

9.2.2. Corrections for electrons

The present calibration in ATHENA is adapted to photons. Calibration is made on cell-level, but one can only de-calibrate clusters. So the constants w_{glob} and w_{ps} from equation 9.1 have to be extracted from

[2] For high energy electrons one should later not only optimize the resolution, but also ensure a good linearity. A good knowledge of the energy scale is important to reduce the systematic error on the decay width.

the present samples. Then, for electrons the following new parametrization is applied, as proposed in [56]:

$$E_{rec} = \lambda(b + w_0 E_{ps} + E_1 + E_2 + w_3 E_3)$$

The standard calibration is canceled by dividing by the weights and the scale, in the same way weights and scale for the electrons are applied. They are determined in the same way from test-beam results as the photon constants. Out of cone,... corrections are not considered: neither for de-calibrating, nor for calibration. They make part of the new weights in this temporary solution.
De-calibration and re-calibration are finalized only for the barrel, as the current photon weights are calculated with an incomplete end-cap simulation. Correct end-cap electron calibration will be available only in one of the next versions once this problem is solved. This de-calibration and re-calibration procedure was finalized and tested on the process $H \to 4e$, i.e. the work was adapted to lower energy electrons.
In the next paragraphs I present the result on single electron datasets to justify that this work can also be applied to more energetic electrons, as well as the result from electron coming from Z' decays and the impact on the Z' mass. For the Z' electrons, only electrons in the barrel are considered.

9.2.3. Results for single electrons at 200 GeV

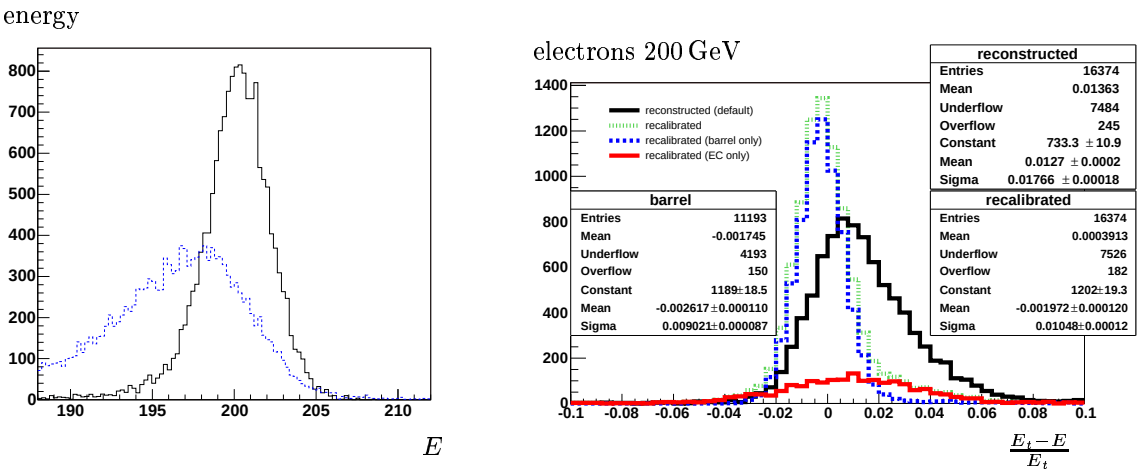

(a) *Energy*
blue/dashed line: standard calibration
black/full line: electron calibration

(b) *Resolution*

Figure 9.2.: *Single electrons, 200 GeV from DC1*

In figure 9.2 initial and re-calibrated energy as well as the resolution are shown. The central value as well as the resolution are improved. The tail in the green/dashed function (re-calibrated, barrel and end-cap) is essentially due to the end-cap (red line) which is not re-calibrated. Besides this strong effect, the tail in the blue function (re-calibrated, barrel only) is due to energy loss by Bremsstrahlung.
The obtained resolution of 0.9% is in agreement with the required one: $\frac{\sigma(E)}{E} = \frac{9.5\%}{\sqrt{E}} \oplus 0.45\% = 0.8\%$. The low energy calibration is therefore valid at this energy scale.

9.2.4. Results for single electrons at 1 TeV

In figure 9.3 the results at 1 TeV are presented. Here the resolution is a little worse, there is a tiny non-linearity in energy, as the obtained resolution is 0.8% whereas the required one is $\frac{\sigma(E)}{E} = \frac{9.5\%}{\sqrt{E}} \oplus 0.45\% = 0.5\%$. However, the calibration works quite fine and therefore will be used for the electrons from the Z'.

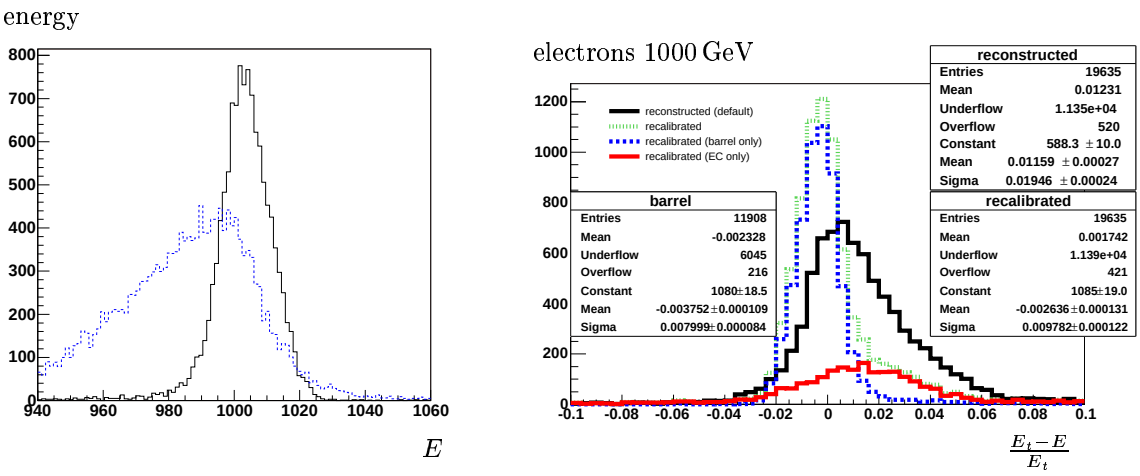

(a) *Energy*
blue/dashed line: standard calibration
black/full line: electron calibration

(b) *Resolution*

Figure 9.3.: *Single electrons, 1000 GeV from DC1*

9.2.5. Results for electrons from $Z' \to e^+e^-$

In figure 9.4 the effect of the re-calibration on the Z' electrons is shown. For the barrel electrons, I obtain $\frac{\sigma(E)}{E} = 0.7\%$ in a good agreement with the predicted one of $\frac{\sigma(E)}{E}|_{750\,GeV} = 0.6\%$.

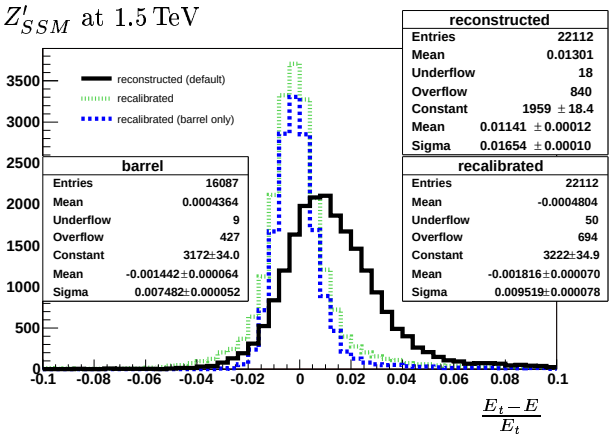

Figure 9.4.: *Electrons from a SSM Z' at 1.5 TeV*

In addition, the effect on the mass distribution is shown for the *SSM* model in figure 9.5. I stress that only barrel electrons are used. In 9.5(a) the mass distributions themselves are shown: truth, before and after re-calibration. With the standard calibration, the mass is underestimated, after re-calibration the right mass value is obtained, the effect of the detector resolution can be seen.
In 9.5(b), this resolution is shown with a log scale: in the central part the resolution is gaussian with a σ of about 10 GeV, i.e. $\frac{\sigma(E)}{E} = 0.75\%$ what is in a good agreement with $\sqrt{2} \cdot \frac{\sigma(E)}{(E)}|_{\text{electrons}} = 0.8\%$. Outside the central part, one has to deal with long tails, which are on the one hand due to Bremsstrahlung (on the right side) and on the other hand certainly due to this temporary de- and re-calibration procedure. As this is only a temporary remedy it is now not tried to understand and correct this tails in details. This should be (and will be) done once a real and physical calibration is implemented. For the moment I am satisfied to parametrize the obtained resolution function including a physical function (gaussian) in the central part. A satisfactory result was obtained with a combination of 3 gaussians - one for the tail on the left-side, one for the central part and another one for the tail on the right-side. This parametrization

is common to all studied models. For comparaison, another resolution function, the sum of only two gaussians, was also tested. One will see that the result of the fit for the decay width is quite sensitive to the resolution function.

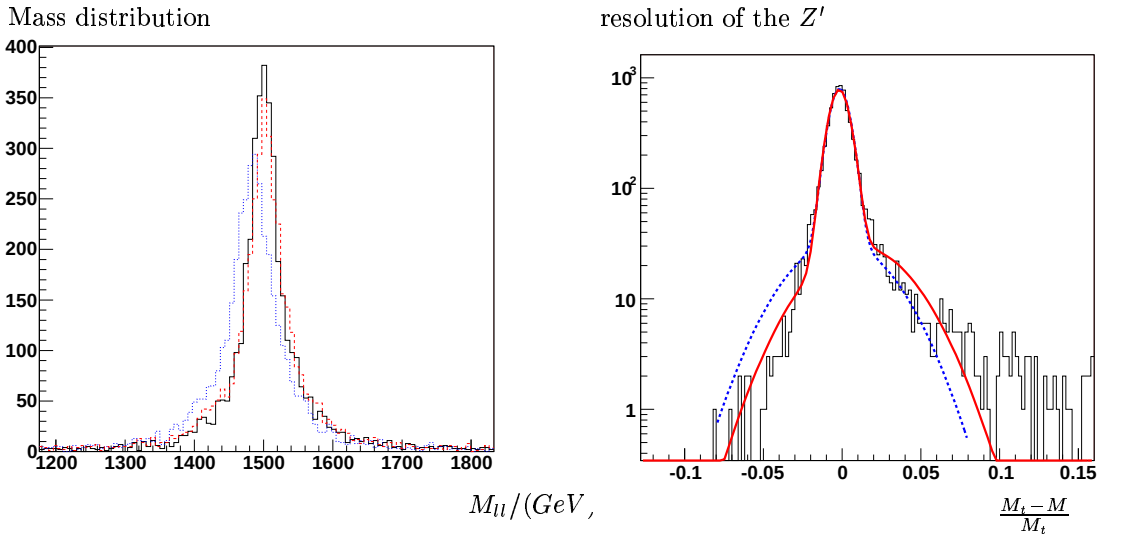

(a) mass distributions
black/solid line truth
blue/dashed line reconstructed
red/dotted line re-calibrated

(b) resolution of the mass, approximated by G+G+G (red/solid line) and G+G (blue/dashed line)

Figure 9.5.: *Effect of the re-calibration on the mass, Z'_{SSM} at 1.5 TeV*

9.3. Analysis of the simulated events

As in the chapter about analysis on generation level, I present at first the results at 1.5 TeV and at the end the results at 4 TeV.

9.3.1. Event selection

Only events with two identified electrons (see section 9.1.2) are kept. Given the acceptance of the calorimeter, all electrons have $|\eta| \leq 2.5$. In addition, it is ensured that the two electrons are isolated (see section 9.1.1), of opposite charge and "back to back": a cut on the angle in the transverse plane between the two leptons in the laboratory frame at 2.9 is applied.
So a total acceptance of about 45% is achieved. Furthermore, as the calibration is not valid in the end-cap, in the study of the decay width and the cross-section only the events with both leptons in the barrel are taken into account. Excluding the events with one or two leptons in the end-cap the total acceptance is reduced to about 35%. In table 9.3 the effect of the different cuts is presented for the SSM as an example.
The trigger on single electrons will be at $p_T = 25\,\text{GeV}$ and for double electrons at $p_T = 20\,\text{GeV}$ and should therefore have a 100% efficiency on this channel.

Today no electronic noise, no pile-up (low luminosity) and no background are included in the simulation, so selection criteria for the signal cannot really be studied. Nevertheless some future selection criteria (e.g. the isolation cut and the cut in the angle α) are already included. Another selection criteria could be for example to keep only events with no missing transverse momentum.
The effect of the electronic noise should be less important than the impact of pile-up at high luminosity. This can be studied later in simulations in the framework of DC2, the next common ATLAS simulation.

initial events	20000 evts
at least two identified and isolated electrons	11418 evts
opposite charge	10683 evts
"back to back"	9184 evts
accepted (all)	9184 evts
accepted (barrel)	7036 evts

initial clusters	57738 clusters
$E_T > 50$	38770 clusters
'ISEM'	34740 clusters
tracks	30986 clusters
hits	30808 clusters
isolation	30451 clusters

Table 9.3.: *Acceptance*

9.3.2. Matching with "truth"

As cross check, the identified electrons and positrons are matched with "truth". The distance[3] is in general smaller than 0.08, the size of about 2 clusters, see figure 9.6(a).

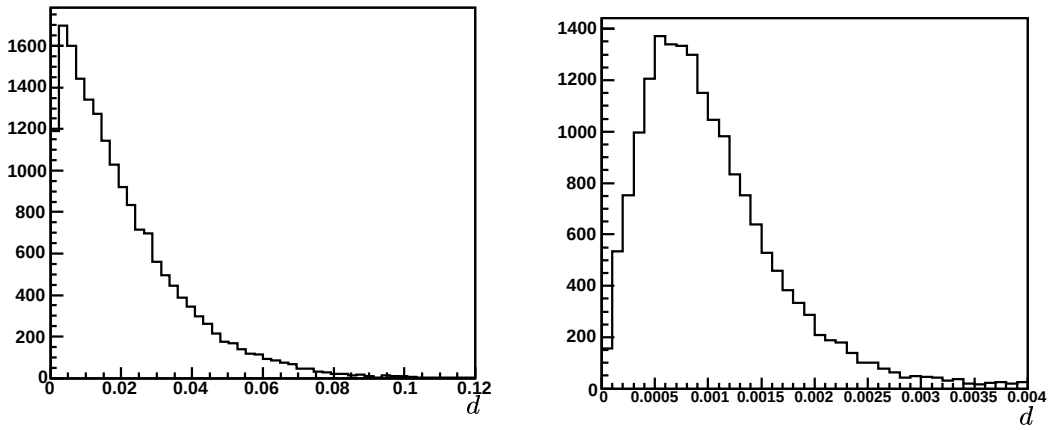

(a) *distance from truth matching* (b) *distance from track matching*

Figure 9.6.: *Distances*

9.3.3. Matching between the calorimeter and the tracker

The matching between the cluster in the calorimeter and the track in the tracker works quite fine. In general, the distance is inferior to 0.03 at a cluster size of 0.35 in the middle layer, see figure 9.6(b). From now on, in each case either the variable of the cluster or of the track are used - each time the most precise one, i.e. the energy from the cluster and the direction (θ and ϕ) from the tracker.

$$\begin{aligned} p_x &= \cos\phi^{track} \cdot E_t^{calo} \\ p_y &= \sin\phi^{track} \cdot E_t^{calo} \\ p_z &= \cot\theta^{track} \cdot E_t^{calo} = \sinh\eta \cdot E_t^{calo} \\ E &= \sqrt{\cot\theta^2 + 1} \cdot E_t^{calo} = \cosh\eta \cdot E_t^{calo} \end{aligned}$$

[3]The distance d is defined as $d = \sqrt{\Delta\phi^2 + \Delta\eta^2}$.

9.3.4. Losses of the electrons (FSR and Bremsstrahlung)

In this first study in full simulation, photons emitted by the electron that are not close enough to the electron to deposit their energy in the same cluster as the electron are neglected. Only the energy of one cluster is taken as electron energy. In a next step, after a study of noise and background one has to try to recover these photons.
A first look showed that there are indeed some photons of up to 500-600 GeV (in the case of a Z' at 1.5 TeV) which deposit their energy in the clusters next to the leptons. For the moment, most of this events are cut by the isolation cut.

9.3.5. Acceptance

The acceptance as a function of the mass (figure 9.7) is not really flat, but this effect is neglected.

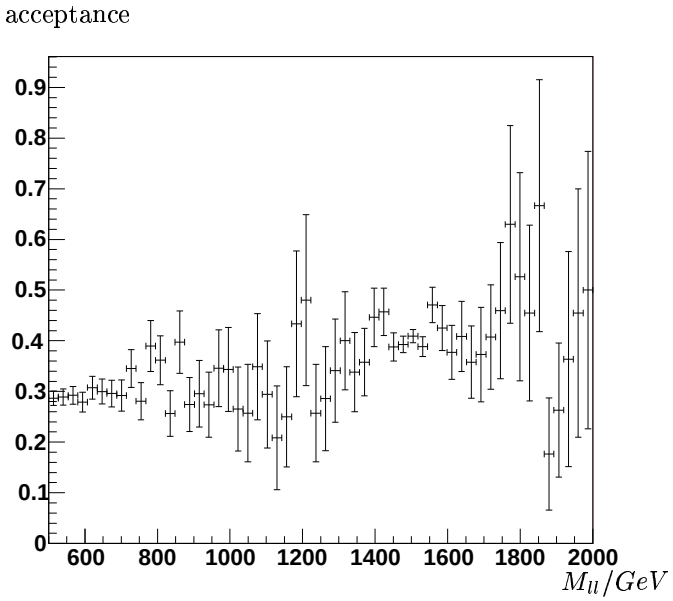

Figure 9.7.: *Acceptance in M*

The acceptance is varying in Y (the rapidity of the Z' boson) and in $\cos\theta^*$ (figure 9.8). For the study of the forward-backward asymmetry the acceptance in Y and in $\cos\theta^*$ is needed[4] (figure 9.9). The acceptance α is symmetric in both cases, one has $\alpha(Y) = \alpha(-Y) = \alpha(|Y|)$ and $\alpha(\cos\theta^*) = \alpha(-\cos\theta^*) = \alpha(|\cos\theta^*|)$. The decrease of acceptance in Y is important. All variables sensitive to Y ($A_{FB}(Y)$, study of the rapidity distribution,...) are therefore very sensitive to the knowledge and control of $\alpha(Y)$.
α is determined with the help of the "truth block" as the ratio of simulated to accepted events.

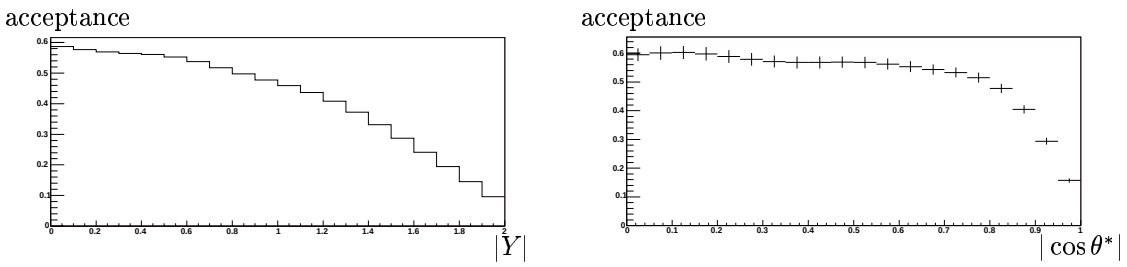

Figure 9.8.: *Acceptance in* $|Y|$ *and in* $|\cos\theta^*|$

[4] As well as for $\cos\theta^\diamond$ of course.

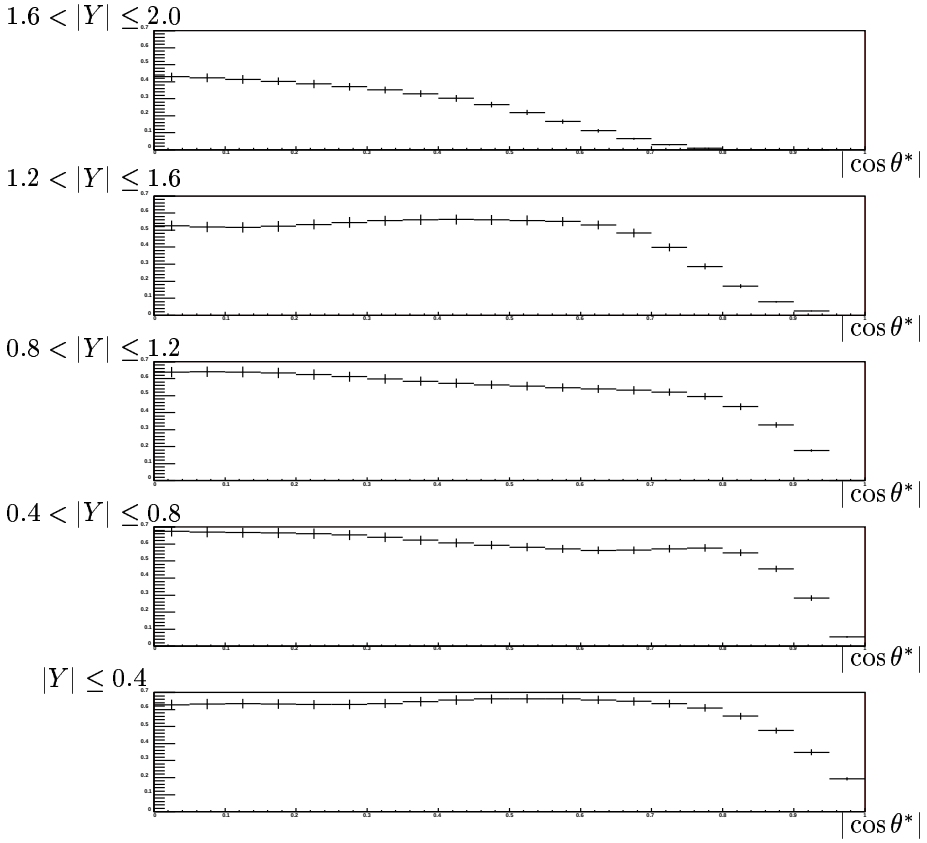

Figure 9.9.: *Acceptance in* $|\cos\theta^*|$ *for different bins in* $|Y|$

9.3.6. Misidentification of the charge of the leptons

The misidentification of the sign of the charge of the leptons leads to another error on the forward-backward asymmetry. If the electron and the positron are confused, the sign of $\cos\theta^*$ is wrong. However this case is rare, as two leptons with opposite charge are required, i.e. both leptons are assigned the wrong charge!
The sign of the charge is determined in the inner detector by the curvature of the track, i.e. it is given by the sign of the transverse momentum.
In the single electrons samples from DC1 at 200 GeV the sign of the charge was found to be wrong in 0.9% of the events, at 1 TeV in 5%. In the TDR 3.6% are predicted for electrons of 1 TeV. So there is a little degradation.
In the sample of the Z'_{SSM} at 1.5 TeV in 6.5% of the events the two leptons do not have opposite charge, i.e. one of them has not the right sign of the charge. This leads to $2p(1-p) = 0.065 \rightarrow p = 0.034$ for the probability p that one lepton has not the right sign of the charge. This is in agreement with the results of the single electrons samples and overall the probability that both leptons have not the right charge is negligible.

9.3.7. Total decay width Γ

The total decay width is now modelized by a convolution of the natural decay width and the detector resolution. The natural decay width is parametrized as above by

$$f(x) = \frac{a}{(x^2 - \breve{M})^2 + b} \cdot \exp^{-cx} + d\exp^{ex}$$

and as resolution function, the combination of 2 or 3 gaussians as proposed in paragraph 9.2.5 is used. The Drell-Yan distribution at low-mass is fitted by an exponential in order to get the initial parameters of this fit function, but it is not fixed anymore to this value.

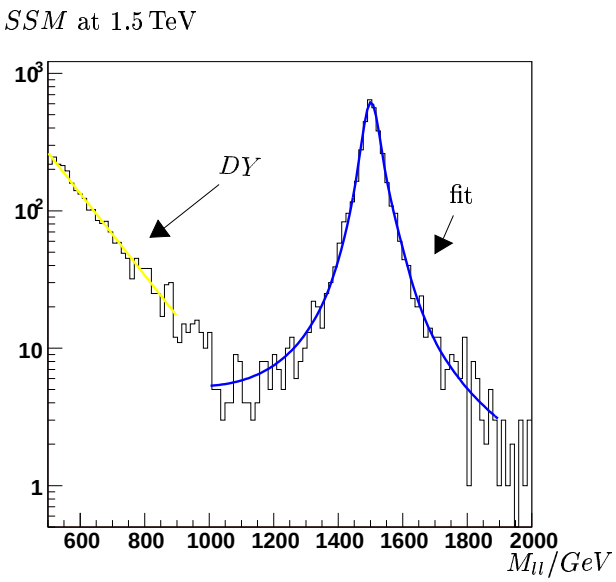

Figure 9.10.: *Fit for the decay width in full simulation*

The convolution is done numerically, $(BW \otimes \text{resolution})(x)$ is calculated by:

```
xlow = x - sc
xupp = x + sc
step = (xupp-xlow)/np

for(i=1; i<= np/2; i++){

        xx  =    xlow    + (i-0.5) · step
        sum =    sum     + BW(xx) · resolution(x[0]-xx)
        xx  =    xupp    - (i-0.5) · step
        sum =    sum     + BW(xx) · resolution(x[0]-xx)

}
return (step · sum)
```

where `np` is the number of convolution steps and where the convolution extends to `M` $\pm$ `sc`. `BW(x)` is the function for the natural decay width, `resolution(x)` is the normalized resolution function.
For the case of the Z'_{SSM}, the result of the fit is shown in figure 9.10.
The results for the two different resolution functions are given in table 9.4 and compared to the theoretical predictions. The decay width is very sensitive to the resolution function. The results of the triple-gaussian function are much better than the double-gaussian function. Once the electron calibration is finalized the resolution function has to be well understood and studied. As on generation level, the systematic error is more important for the narrow Z' models.

	$\Gamma_{theo.}$(GeV)	Γ(GeV) G+G	Γ(GeV) G+G+G
SSM	44.7	53.8 $\pm$ 1.3	46.5$\pm$ 2.5
Z'_{ψ}	8.0	11.8$\pm$ 0.2	8.9$\pm$ 0.6
Z'_{η}	9.5	13.$\pm$ 0.2	9.8$\pm$ 0.6
Z'_{χ}	17.6	20.8$\pm$ 0.4	16.5$\pm$ 0.8
LR	30.6	34.3 $\pm$ 1.2	28.4$\pm$ 1.2

Table 9.4.: *Decay width in full simulation*

9.3.8. Cross-section

The cross-section is determined in the same way as above. The results are given in table 9.5 and compared to the values of PYTHIA. The $\sigma \cdot \Gamma$ product is given as well.
First, events in $M \pm 4\Gamma$ are taken into account. The cross-sections are slightly under-estimated. In a second step events in $M \pm (4\Gamma + 30\,\mathrm{GeV})$ are taken into account in order to roughly correct for the resolution. This way, there is a good agreement with the predictions of PYTHIA.
The acceptance was corrected with the mean acceptance in the region in mass around the peak. The acceptance in mass is not flat enough to use the global average acceptance of all events.

	$M \pm 4\Gamma$		$M \pm (4\Gamma + 30\,\mathrm{GeV})$		
	σ(fb)	$\Gamma \cdot \sigma$(fb·GeV)	σ(fb)	$\Gamma \cdot \sigma$(fb·GeV)	σ(fb) theory
SSM	77.1.4 ± 2.5	3586.8 ± 227.09	78.3 ± 3.0	3642.5 ± 240.9	78.8
Z'_ψ	21.8 ± 0.4	195.9 ±12.9	23.3± 0.5	207.1 ± 13.8	23.5
Z'_χ	44.9±1.0	738.4 ± 40.3	47.6 ± 1.1	782.6 ± 42.5	47.9
Z'_η	24.1 ± 0.5	235.2 ± 14.3	26.7 ± 0.5	260.2 ± 15.8	26.3
LR	49.5 ±1.1	1406.8± 68.9	50.7 ± 1.1	1440.6 ± 70.5	50.0

Table 9.5.: *Results on σ and $\sigma \cdot \Gamma$*

9.3.9. $A_{FB}(M)$

Also the events with one or two electrons in the end-cap are used as a precise calibration is less important here.
The asymmetry as a function of M is determined in three ways, as usual:

- A_{FB}^{obs} is determined by fitting,
- A_{FB}^{obs} is determined by counting,
- A_{FB}^{corr} is determined by a two dimensional fit including the dilution factor.

No cut in $|Y|$ is applied as the acceptance decreases too much in $|Y|$. Fitting has the advantage that no corrections for acceptance are needed[5].
The values for A_{FB}^{obs} by fitting and counting (corrected by acceptance) are in agreement and presented in table 9.6. In the case of counting the systematic error from the correction of acceptance is included.
In table 9.6 the result of the two dimensional fit A_{FB}^{corr} is also shown, as well as A_{FB}^{true} determined by fitting with the help of the "truth". The two dimensional fit gives an A_{FB}^{corr} which is closer to A_{FB}^{true} than A_{FB}^{obs}, but does not recover A_{FB}^{true} entirely. Especially at the edges where are only few events the result of the two dimensional fit is not very reliable.
Later on, the bins in mass have to be adapted to the decay width and to the resolution. The asymmetry depends on mass and too small bins could falsify the asymmetry as several events are not in the correct bin of mass. Additionally the $\epsilon(Y)$ function that is used for the dilution factor depends also on the mass.

	A_{true}	A_{obs} $\angle(e^-, Z')$		A_{corr}
	$\angle(e^-, q)$	fit 1D	counting	fit 2D
SSM	0.08 ± 0.01	0.04 ± 0.02	0.04 ± 0.02	0.06 ± 0.06
Z'_ψ	0.01± 0.01	-0.01 ± 0.02	-0.00 ± 0.02	-0.01± 0.06
Z'_χ	-0.35± 0.01	-0.14 ± 0.02	-0.13 ± 0.02	-0.31±0.06
Z'_η	-0.08± 0.01	-0.04 ± 0.02	-0.03± 0.02	-0.08±0.06
LR	0.19± 0.01	0.12 ± 0.02	0.12 ± 0.02	0.20±0.06

Table 9.6.: *On-peak values for the different models for the different methods*

9.3.10. $A_{FB}(Y)$

As $A_{FB}(Y)$ is determined by counting, acceptance has to be corrected in each bin of $|Y|$. The results for the slope are shown in table 9.7 and are in a good agreement with the results at generation level.

[5] Only in the case of a symmetric acceptance, what is admitted here.

	full simulation	generation
SSM	0.08 ± 0.03	0.07 ± 0.01
Z'_ψ	0.01 ± 0.03	0.01 ± 0.01
Z'_χ	-0.25 ± 0.01	-0.22±0.03
Z'_η	-0.07 ± 0.03	-0.04±0.01
LR	0.14 ± 0.04	0.16± 0.03

Table 9.7.: *Slope of* $A_{FB}(Y)$

9.3.11. A quick look at $M = 4$ TeV

I had only a quick look at $M = 4\,\text{TeV}$ as it was not possible anymore to do much simulation in the framework of DC1 as DC2, the next common ATLAS simulation, was already starting. We did not want to switch to DC2 in order to compare the two points in mass in exactly the same conditions.
So it was chosen to simulate only the SSM, the "reference model", and the Z'_{KK} as it was not studied in full simulation before. In the SSM case a high number of events (10 000) was chosen to compare with the results at $M = 1.5\,\text{TeV}$, even if this corresponds to a non-realistic integrated luminosity (30 000 fb^{-1}). In the KK case about $500 fb^{-1}$, i.e. 5 years at high luminosity, were chosen.

As electron identification and isolation criteria, exactly the same criteria as for $M = 1.5\,\text{TeV}$ have been used as I had not enough statistics to do a more deepened study. In the next step, when we move to DC2, these are important points to check.
In the same way the resolution on the mass and the acceptance functions are taken from $M = 1.5\,\text{TeV}$. It was shown that they are at least compatible for $M = 4\,\text{TeV}$, but could and should be improved.
With these electron selection criteria, a comparable acceptance is achieved, around 45% in the whole calorimeter, less than 40% in the barrel.
Calibration is working quite satisfactorily. I get $\frac{\sigma(E)}{E} = 0.6\%$, the prediction for 2 TeV electrons is around 0.5%, see figure 9.11.

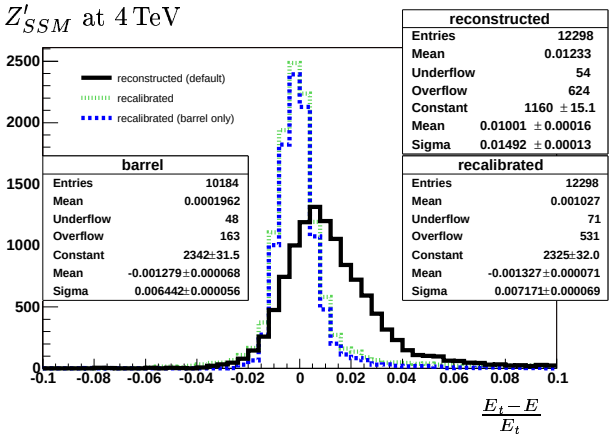

Figure 9.11.: *Electrons from a SSM Z' at 4 TeV*

The probability of charge misidentification increases up to about 10%, i.e. as I am looking for events with two leptons with opposite charge: in 1% of the events the electron is misidentified as positron and vice-versa. This induces a further error on the asymetry that is neglected at this mass but would have to be taken into account at higher masses, especially as this probability is growing fast with energy.

Decay width and leptonic cross section

As before the total decay width (see table 9.8) is overestimated, in this case up to 20%. As mentioned before, this is due to the uncertainties of the resolution function, the Drell-Yan and lepton parton luminosity parametrization.
The results on the leptonic cross section (table 9.9), where events in $M \pm (4\Gamma + 30\,\text{GeV})$ are taken, are fine.

	theory	generation level	full simulation
SSM	119.2 GeV	(121.9 ± 0.8) GeV	(142.0 ± 4.3) GeV
KK		(180.0 ± 1.2) GeV	(194.5 ± 16) GeV

Table 9.8.: *Total decay width at 4 TeV*

	σ(fb)	σ(fb) pythia	$\sigma \cdot \Gamma$ (fb·GeV)
SSM	0.24 ± 0.01	0.26	34.38 ± 1.28
KK	2.2 ± 0.1	2.3	419.4 ± 41.6

Table 9.9.: *Cross-section in full simulation at 4 TeV*

$A_{FB}(M)$

The *true asymmetry*, *observed asymmetry* and *corrected asymmetry* are shown on figure 9.12 and in table 9.10. The result is satisfactory, except in the edges where low statistics are available. A better knowledge of $\epsilon(Y)$ is needed and the bins in M maybe have to be better adapted to the decay width, detector resolution and the number of events in a bin. In a first step, non-equidistant bins could be chosen.

	A_{true}	A_{obs}	A_{corr}
SSM	0.06 ± 0.01	0.03 ± 0.02	0.05 ± 0.07
KK	0.46 ± 0.03	0.19 ± 0.03	0.41 ± 0.14

Table 9.10.: *On-peak values for $A_{FB}(M)$ in full simulation at 4 TeV*

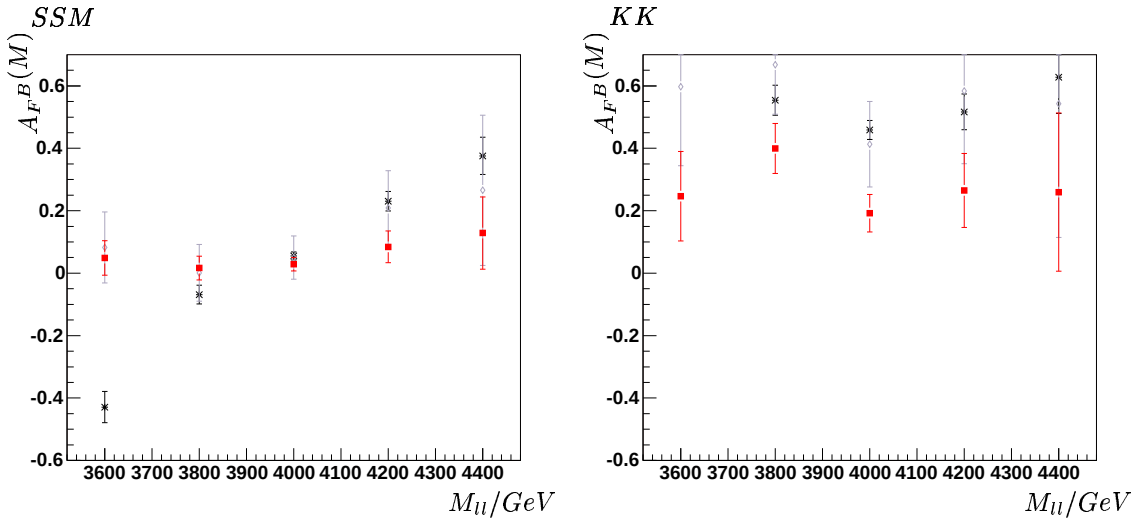

Figure 9.12.: $A_{FB}(M)$ *at 4 TeV in full simulation.*
In black (∗) the true asymmetry, in red (■) the observed asymmetry and in gray (◊) the corrected asymmetry (result of the 2 dimensional fit).

$A_{FB}(Y)$

Some asymmetry (see figure 9.13 and table 9.11) is lost. This is due to the wrong parametrization[6] of the acceptance that is needed both as a function of $|Y|$ and of $|\cos\theta^\star|$. The acceptance in $|Y|$ is compared for the two masses in figure 9.14, $\alpha(|Y|)$ depends on the mass of the Z' boson as the Y distribution depends on it. $A_{FB}(Y)$ is very sensitive to this acceptance function.

[6]The acceptance was determined for $M = 1.5$ TeV.

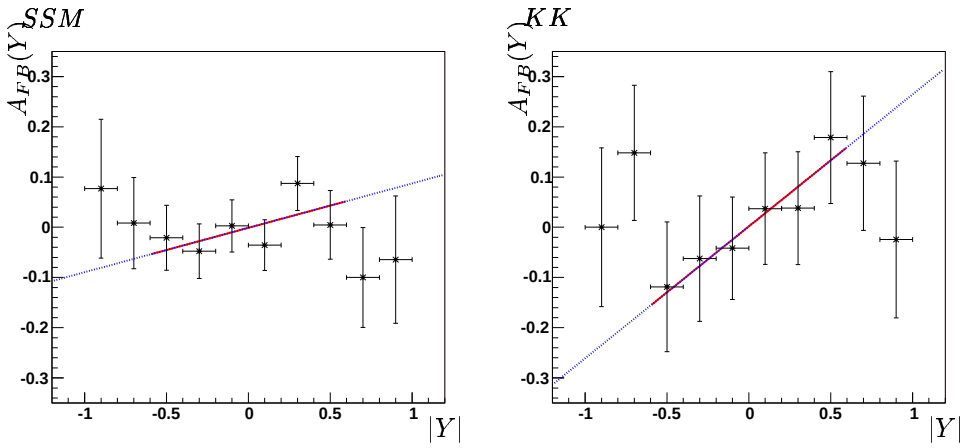

Figure 9.13.: $A_{FB}(Y)$ *in full simulation at 4 TeV*

	full simulation	generation
SSM	0.09 ± 0.07	0.15 ±0.03
KK	0.26 ± 0.15	0.85 ± 0.01

Table 9.11.: *Slope of* $A_{FB}(Y)$

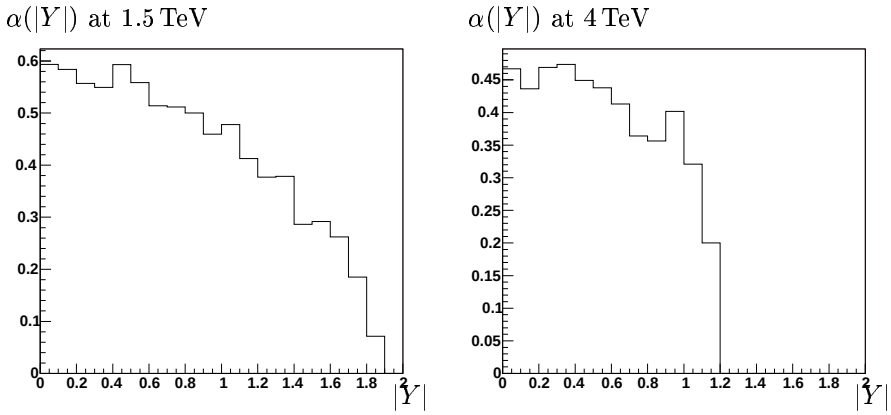

Figure 9.14.: *Acceptance in* $|Y|$ *at 1.5 TeV and 4 TeV (SSM events)*

9.3.12. Conclusions

The different discriminating variables have been studied in full simulation. The total decay width is very sensitive to the resolution function. The understanding of the DY, the interference, the parton luminosity and above all the resolution function has to be improved. The decay width is systematically overestimated (sometimes up to 20%). Cross-sections are in a good agreement with the predictions. The results for the asymmetries are in a good agreement with the results at generation level for A_{obs}. A_{corr} recovers A_{true} with the help of the two dimensional fit for the on-peak values, at the edges the results are less satisfactory. A better understanding of $\epsilon(Y)$ and better a binning in M is needed. $A_{FB}(Y)$ is very sensitive to the acceptance.
Electron identification and calibration as well as the acceptance have to be studied in more details at higher masses, the little statistics available at $M = 4\,\text{TeV}$ did not allow this.
At 4 TeV the SSM and the KK model have been studied with a rather different number of events, the Z'_{KK} with a realistic number of events. Comparison shows a validation of the tools both with respect to the change of energy scale, but also with respect to a realistic scenario of available statistics.

10. ... towards discrimination

In the present work the measurement of the main discriminating variables is designed in full simulation. In addition to the statistical errors, the following systematical errors will have to be taken into account (see also [17]):

- ⋆ for σ: as already mentioned it is always difficult to determine an absolute cross-section as it is not easy to measure precisely the luminosity and the absolute acceptance. Either an appropriate process to normalize the cross section would be found or there would be a systematic error from the luminosity measurement.
  Of course, there are systematic uncertainties from the modelisation of the DY and the parton luminosity as well.
  In addition there are systematic errors from higher order QCD and electro-weak corrections[1].
- ⋆ for Γ: there are essentially the same systematic errors as for σ; in addition, there is a systematic error from the knowledge of the energy scale, i.e. from the calibration.
- ⋆ for A_{FB}: if the asymmetry is determined by a 2D fit, we have a systematic error from the parametrization of the $\epsilon(Y)$ function. In all cases, there is a systematic error from the correction of the acceptance and from assuming that it is symmetric in Y and $\cos\theta^\star$. In pp collisions the assumption of a symmetric acceptance is already fine, but there could be other effects that lead to a non symmetric acceptance, e.g. a different acceptance for electrons and positrons leads to $\alpha(\cos\theta^\star) \neq \alpha(-\cos\theta^\star)$.

For sure, each variable separately will not be sufficient, the different variables have to be combined.
As an example in figure 10.1 the variation of the decay width Γ is shown as a function of the model parameters κ for the LR models and $\cos\beta$ for the E_6 models: $\Gamma(\kappa)$ and $\Gamma(\cos\beta)$. Already in these figures it is obvious that there are some ambiguous zones (e.g. $\Gamma(\cos\beta)$ is nearly "symmetric" at 0) and zones where Γ is varying only very slowly (e.g. in the region around $\kappa = 0.75$). There discrimination would never be possible using only the decay width.
The different branching ratios $Br(i) = Br(Z' \to i\bar{i}), i = u, d, e, \nu$ are shown in the same figure.

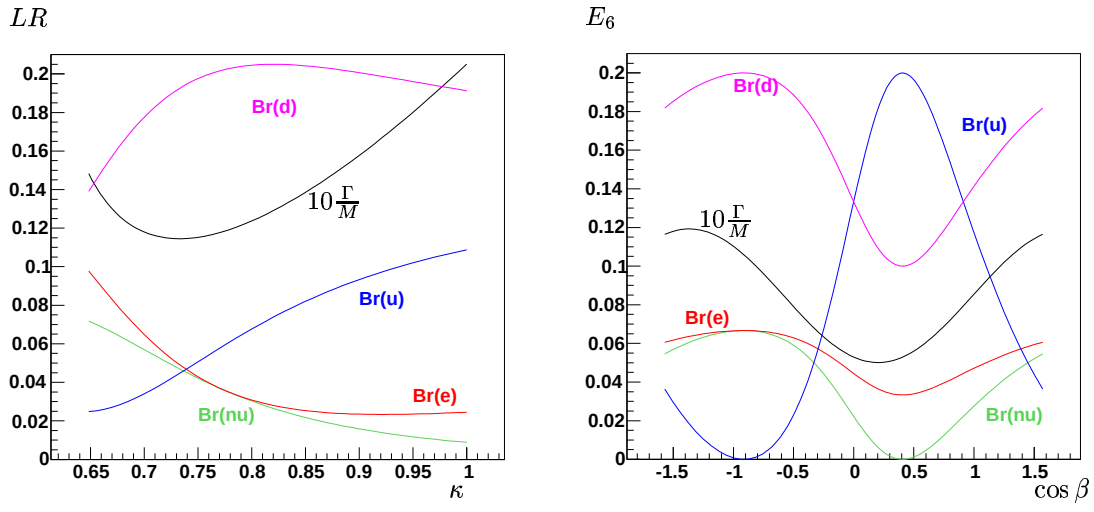

Figure 10.1.: *The different branching ratios Br(i) ($Br(i) = Br(Z' \to i\bar{i}), i = u, d, e, \nu$) and the total decay width (normalized on M) is shown as a function of κ respectively $\cos\beta$.*

[1] We took the approximation $k = 1$ for $\sigma_{tot} = k\sigma_{LO}$.

In figure 10.2 the ratio $\frac{\Gamma_1}{\Gamma_2} = \frac{\Gamma(\kappa_1)}{\Gamma(\kappa_2}$ is shown covering the total parameter space in $\kappa_1 \times \kappa_2$ (respectively for $\frac{\Gamma(\cos\beta_1)}{\Gamma(\cos\beta_2)}$ and $\frac{\Gamma(\kappa_1)}{\Gamma(\cos\beta_2)}$). In zones with $\frac{\Gamma_1}{\Gamma_2}$ close to 1 no discrimination with Γ is possible, in zones with $\frac{\Gamma_1}{\Gamma_2}$ far of 1 the decay width has a good discrimination power.

To discriminate between the different models one may include in the analysis other proposed discriminating variables, as for example:

- ⋆ the Z' rapidity distribution [3] in the e^+e^- channel;
- ⋆ the ratio of cross-section in different rapidity bins [39] in the e^+e^- channel;
- ⋆ informations from other decay channels as $\tau^+\tau^-$, jet-jet or four-fermion final states [18];
- ⋆ the off-peak asymmetry or other deviations from pure DY [17].

There are also additional informations from other particles or decay channels: in the models with a Z' there is usually also a W' boson [57] predicted; a graviton [9] could not only decay in two leptons but also in two photons. In addition the angular distribution of a graviton would be a spin 2 and not a spin 1 distribution.

There are already different discrimination strategies proposed, that should be studied now knowing better the predicted experimental uncertainties.

- ⋆ There is the idea of a "global fit" including all proposed discriminating variables.
- ⋆ In [18], four "normalized couplings" are defined that could be extracted examining the discriminating variables. It seems that at least for three of them the error bars are sufficiently small to distinguish between models. In [58] the extended gauge structure is reconstructed knowing these "normalized couplings".
- ⋆ In [20], the emphasize is put on differentiating the Z'_{KK} from GUT Z's. Among different strategies it is proposed to vary all of the couplings of a GUT Z' to quarks and leptons independently in order to obtain the best χ^2/df fit to the dilepton mass distribution and obtain the relevant probability/confidence level(CL) using statistical errors only. However, this strategy needs extremely high luminosity, likely more than ever available at LHC. Therefore let us postpone this discrimination to the generation of accelerators after LHC, the LC, which anyway needs as input the mass of a Z' discovered at LHC.

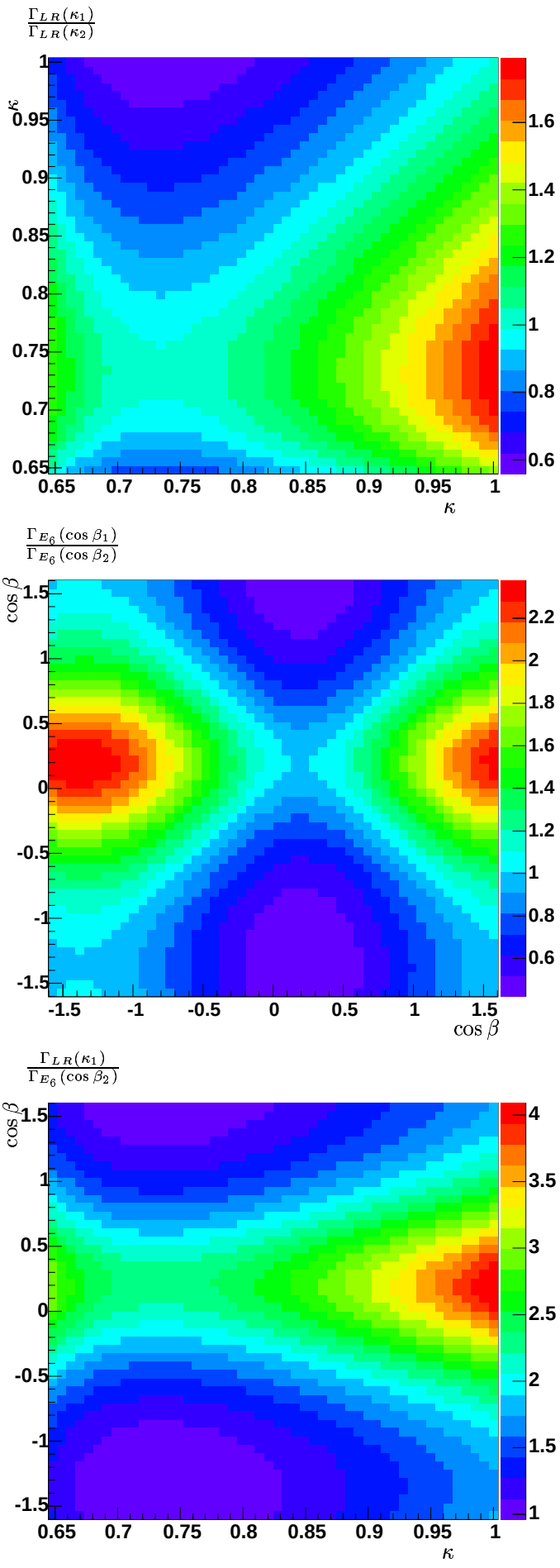

Figure 10.2.: *Ratio* $\frac{\Gamma_1}{\Gamma_2}$ *for the parameter spaces* $\kappa \times \kappa$, $\cos\beta \times \cos\beta$ *and* $\kappa \times \cos\beta$.

11. Conclusions and Outlook

The $Z' \rightarrow e^+e^-$ channel was chosen as it is the most promising for observation and discrimination among the leptonic decay channels. Two different Z' mass were studied: 1.5 TeV and 4 TeV.
The Sequential Standard Model, several E_6 models, a left-right symmetric model and one extra dimension model (Kaluza Klein resonances of the Z boson) have been scrutinized.
It was shown that, even with $M \sim 4$ TeV, the signal could easily be observed in all studied models.
The main variables, which are expected to discriminate between various Z' models beyond the Standard Model, have been studied in detail: the total decay width, the leptonic cross-section and the forward-backward asymmetries.

A study at generation level has been done to validate the tools to extract these discriminating variables. The results are satisfactorily close to theory. In a second step it was shown that it is possible to measure these observables in full simulation.
The cross-section is in a good agreement with the predictions. The decay width is slightly overestimated. It is very sensitive to the parametrization of the resolution function. At least for decay widths of the order or bigger than the detector resolution, a satisfactory result was achieved. At high masses this is the case for all studied models.
The forward-backward asymmetries have been studied as a function of the mass and the rapidity of the Z' boson. With the help of a dilution factor the *true asymmetry* was recovered in the on-peak region; however in regions with low statistics, the method is not yet totally satisfactory.
Methods have been established and well tested tools have been produced, which can now be easily and quickly used on other simulations or other models.

In a next step, the study in full simulation has to be redone in an even more realistic simulation. In the framework of DC2, pile-up at high luminosity will be available and its effect as well as the effect of the electronic noise have to be studied. In DC2, an official electron calibration will be available. Therefore the resolution on the mass can be studied and parametrized in a less preliminary way. A public standard isolated electron identification is also foreseen.
The variation of the acceptance with mass should be studied in more details as well as the effect of charge misidentification. Possibly this effect has to be corrected at higher masses.
Apart from switching to DC2, a better knowledge of the DY at high energy will be necessary as well as a better parametrization of the parton luminosity to improve the results on the decay width and on the cross section. The 2D fit for the asymmetry could be improved by a better modelisation of the $\epsilon(Y)$ function. The binning in M for the study of $A_{FB}(M)$ has to be adapted to the decay width and the detector resolution. The characterization of $A_{FB}(Y)$ by the slope of a straight line has to be reconsidered with respect to discrimination.
Finally other discriminating variables, e.g. the rapidity distribution, have to be considered and physical background has to be included in full simulation to better optimize the selection cuts.

A discrimination strategy can now be developed, knowing how to extract the discriminating variables and their expected precision.

A. KK modes in a 5 dimensional Abelian Models [59]

One considers the Lagrangian of 5-dimensional Quantum Electrodynamics given by

$$\mathcal{L} = -\frac{1}{4} F_{MN}(x,y) F^{MN}(x,y) + \mathcal{L}_{GF},$$

where

$$F_{MN}(x,y) = \partial_M A_N(x,y) - \partial_N A_M(x,y),$$

denotes the 5-dimensional field strength tensor and $\mathcal{L}_{GF}$ the gauge-fixing term. The notation for the Lorentz indices and space-time coordinates is $M,N = 0,\ldots,4$, $\mu,\nu = 0,\ldots,3$, $x = (x^0, \boldsymbol{x})$ and $y = x^5$ denotes the additional dimension.
The structure of the conventional QED Lagrangian is simply carried over to the five-dimensional case, the Lagrangian is invariant under a $U(1)$ gauge transformation:

$$A_M(x,y) \to A_M(x,y) + \partial_M \Theta(x,y).$$

So far, all spatial dimension are treated in the same way, this is certainly an assumption in contradiction not only to experimental evidence, but also to our daily experience. There has to be a mechanism to hide the 5th dimension at low energies. The simplest way to do this is compactification; a simple one dimensional compact manifold is a circle, denoted by S^1, with radius R. Asking for an additional reflection symmetry Z_2 with respect to $y = 0$ leads to S^1/Z_2[1]. Thus y is considered to run from 0 to $2\pi R$, where these two points are identified. Moreover, according to the Z_2 symmetry, y and $-y = 2\pi R - y$ can be identified, knowing the field content for the segment $[0,\pi] \ni y$ implies the knowledge of the whole system. For that reason, the two fix points ($y = 0$ and $y = \pi R$) are called boundaries of the orbifold.
The compactification on S^1/Z_2 reflects in certain restrictions for the fields. In order not to spoil the above property of the gauge symmetry, one demands the field to satisfy the following equalities:

$$\begin{aligned} A_M(x,y) &= A_M(x, y + 2\pi R) \\ A_M(x,y) &= A_M(x,-y) \\ A_5(x,y) &= -A_5(x,-y) \\ \Theta(x,y) &= \Theta(x, y + 2\pi R) \\ \Theta(x,y) &= \Theta(x,-y) \end{aligned}$$

The field $A_\mu(x,y)$ is taken to be even under Z_2, to embed conventional QED with a massless photon into the 5D-QED. The reflection properties follow automatically if the theory should remain gauge invariant after compactification.
Making the periodicity and reflection properties of A_μ and Θ explicit, we can expand this quantities in Fourier series

$$\begin{aligned} A^\mu(x,y) &= \frac{1}{\sqrt{2\pi R}} A^\mu_{(0)}(x) + \sum_{n=1}^{\infty} \frac{1}{\sqrt{\pi R}} A^\mu_{(n)}(x) \cos\frac{ny}{R}, \\ \Theta(x,y) &= \frac{1}{\sqrt{2\pi R}} \Theta_{(0)}(x) + \sum_{n=1}^{\infty} \frac{1}{\sqrt{\pi R}} \Theta_{(n)}(x) \cos\frac{ny}{R}. \end{aligned}$$

The Fourier coefficients $A^\mu_{(n)}$ are the so-called Kaluza-Klein modes. The extra component of the gauge field is odd under the reflection symmetry, its expansion is given by

$$A^5(x,y) = \sum_{n=1}^{\infty} \frac{1}{\sqrt{\pi R}} A^5_{(n)}(x) \sin\frac{ny}{R}.$$

[1] This additional symmetry leads to fermion chirality [60].

There is no zero mode.
At this point, the theory is again formulated entirely in terms of four-dimensional fields, the KK modes. All the dependency of the Lagrangian density on the extra coordinate y is parametrized with simple Fourier functions. As physics is dictated by the Lagrangian anyway, one can completely remove the explicit y dependence by integrating out the extra dimension. From now on, the quantity of interest will be

$$\mathcal{L}(x) = \int_0^{2\pi R} dy \mathcal{L}(x,y).$$

All the higher dimension physics is reflected by the infinite tower of KK modes for each field component. Calculation yields

$$\mathcal{L}(x) = -\frac{1}{4}F_{(0)\mu\nu}F^{\mu\nu}_{(0)} + \sum_{n=1}^{\infty}\left[-\frac{1}{4}F_{(n)\mu\nu}F^{\mu\nu}_{(n)} + \frac{1}{2}\left(\frac{n}{R}A_{(n)\mu} + \partial_\mu A_{(n)5}\right)\left(\frac{n}{R}A^{\mu}_{(n)} + \partial^\mu A_{(n)5}\right)\right] + \mathcal{L}'_{GF}(x).$$

The first term represents the conventional QED involving the massless field $A^\mu_{(0)}$. Note that all the other vector excitations $A^\mu_{(n)}$ from the infinite tower of KK modes come with mass terms, their mass being an integer multiple of $\frac{1}{R}$. Note also that it is the absence of $A^5_{(0)}$ due to the odd Z_2 symmetry of $A^5(x,y)$ which allows us to recover conventional QED in the low energy limit. For $n > 0$, the KK tower for the additional component of the five dimensional vector field mixes with the vector modes. The modes $A^5_{(n)}$, being scalars with respect to the four dimensional Lorentz group, play the role of the would-be Goldstone modes in a non-linear realization of an Abelian Higgs model. Thus, one is tempted to view the mass generation for the heavy KK modes by compactification as a kind of geometric Higgs mechanism.
Fermions are now introduced in the same spirit, but fixed on the orbifold point $y = 0$ what will be formalized by introducing a δ-function:

$$\mathcal{L}_F(x,y) = \delta(y)\bar{\Psi}(x)(i\gamma^\mu D_\mu - m_f)\Psi(x),$$

where the covariant derivative

$$D_\mu = \partial_\mu + ie_5 A_\mu(x,y)$$

contains the bulk gauge field and e_5 denotes the coupling constant of 5D-QED.
Again integrating out the fifth dimension, we are left with an effective four dimensional interaction Lagrangian

$$\mathcal{L}_{int}(x) = -e\bar{\Psi}\gamma^\mu\Psi\left(A_{(0)\mu} + \sqrt{2}\sum_{n=1}^{\infty}A_{(n)\mu}\right),$$

coupling all the KK modes to the fermion field on the brane. The coupling constant $e = \frac{e_5}{\sqrt{2\pi R}}$ is the QED coupling constant as measured by experiment. The factor $\sqrt{2}$ is a typical enhancement factor for the coupling of the brane fields to heavy KK modes. Note that the scalar modes $A^5_{(n)}$ do not couple at all to brane fermions because their wave functions vanish at $y = 0$.
Even though nature is not described by QED only, the generic signatures of extra dimensions are quite similar to those in more realistic theories. So a simple extension to the SM with massive gauge bosons leads for all gauge bosons A_μ to

$$\mathcal{L}_{int}(x) = g\bar{\Psi}\gamma^\mu(g_V + g_A\gamma^5)\Psi\left(A_{(0)\mu} + \sqrt{2}\sum_{n=1}^{\infty}A_{(n)\mu}\right),$$

and $M^2_{(n)} = \left(\frac{n}{R}\right)^2 + M_0^2$.

Bibliography

[1] M.Y.Han, Quarks and Gluons: A century of Particle Charges, World Scientific (1999)

[2] M.Carena, A.Delao et al., Z' Gauge Bosons at Tevatron, FERMILAB-Pub-04/129-T, hep-ph/0408098 (2004)

[3] M.Dittmar, A.Nicollerat, A.Djouadi, Z' studies at the LHC: an update, Phys.Lett. B583 (2004) 111-120

[4] PDG, Particle Physics Booklet (2002)

[5] H.Perkins, Introduction to High Energy Physics (1987), Addition Wesley

[6] V.D. Barger, Collider Physics (1987), Addition Wesley

[7] C.S.Wu, Phys.Rev. D105 (1957) 1423

[8] F.del Aguila, M.Quiros, F.Zwirner, Detecting E_6 neutral gauge bosons through lepton pairs at hadron colliders, Nucl.Phys. B287 (1987) 419-456

[9] C.Collard, M.C.Lemaire, P.Tracyk, G.Wrochna, Prospects for Study of Randall-Sundrum Gravitons in the CMS Experiment, CMS-NOTE-2002-050 (2002)

[10] F.del Aguila, The Physics of the Z' bosons (Lectures delivered at the XVII International School of Theoretical Physics) (1993), Acta Phys. Polon. B35:1317-1336 (1994), hep-ph/9404323v1

[11] V.Barger, N.G.Deshpande, J.L.Rosner, K.Whisnant, Production, decays, and forward-backward asymmetries of extra gauge bosons in E_6, Phys.Rev.D 35 (1987) 2893

[12] M.Cvetič, P.Langacker, Determination of g_R/g_L in Left-Right Symmetric Models at Hadron Colliders, Phys.Rev.Lett. 68 (1992) 2871

[13] P.Langacker, R.W.Robinett, J.L.Rosner, New heavy gauge bosons in pp and $p\bar{p}$ collisions, Phys.Rev. D30 (1984) 1470

[14] O.Aharony et al., Large N field theories, String theory and gravity, Phys.Rept.323:183-386 (2000), Y. Oz, Superstrings, black holes and gauge theories, CERN Courrier 39N3:13-16 (1999)

[15] K.Hagiwara et al. (Particle Data Group), Phys.Rev. D 66, 010001 (2002) (URL: http://pdg.lbl.gov) and references therein, especially:
N.Arkani-Hamed, S.Dimopoulos, G.R.Dvali, Phys.Lett. B429, 263 (1998)
L.Randall, R.Sundrum, Phys.Rev.Lett. 83, 3370 (1999)

[16] T.Kaluza, Preuss.Akdad.Wiss, Berlin, Math. Phys. K1, 966 (1921)
O.Klein, Z. Phys. 37 895, Nature 118, 516 (1926)

[17] G.Azuelos, G.Polesello, Prospects of the detection of Kaluza-Klein excitations of gauge bosons in the ATLAS detector at the LHC, SN-ATLAS-2003-023 (2003)

[18] M.Cvetič, S.Godfrey, Discovery and identification of extra gauge bosons, hep-ph/9504216v1 (1995)

[19] V.Barger, T.G.Rizzo, Some phenomenological aspects of the $SU(2)_q \times SU(2)_l \times U(1)_Y$ model, Phys.Rev. D41 (1990) 946

[20] T.G.Rizzo, Kaluza-Klein/Z' Differentiation at the LHC and the Linear collider, JHEP 0306:021, hep-ph/0305077 (2003)

[21] R.Casalbuoni et al., Signals of the degenerate BESS model at the LHC, Eur.Phys.J C18 (2000) 65-71

[22] T.Han et al., Phenomenology of the Little Higgs Model, hep-ph/0301040 (2003)

[23] J.L.Hewett, B.Lillie, T.G.Rizzo, Monte Carlo Exploration of Warped Higgsless Models, hep-ph/0407059v1 (2004)

[24] A.J.Burr, Studies of supersymmetric models for the ATLAS experiment at the Large Hadron Collider, dissertation submitted to the University of Cambridge (2002)

[25] ATLAS Letter of Intent, CERN/LHCC/92-4, LHCC/I2 (1992)

[26] ATLAS Technical Proposal, CERN/LHCC/94-43, LHCC/P2 (1994)

[27] V.Barger, K.Whisnant, Heavy-Z-boson decays to two bosons in E_6 superstring models, Phys.Rev. D36 (1987) 3429

[28] M.Cvetič, P.Langacker, Rare decays as diagnostics for Z' gauge couplings at hadron colliders, Phys.Rev. D46 (1992) R14

[29] J.Shank et al., Studies of A^0, Z' and W' Production and Detection with The ATLAS Muon Detector, ATLAS Internal Note MUON-NO-161 (1997)

[30] J.D.Anderson, M.H.Austern, R.N.Cahn, Measurements of Z' couplings at future hadron colliders through decays to τ leptons, Phys.Rev. D46 (1992) 290

[31] M.H.Austern, Z' Phenomenology, Ph.D. Thesis (1994)

[32] F.Halzen, A.Martin, Quarks & Leptons: An Introductory Course in Modern Particle Physics (1984), John Wiley and Sons

[33] M.Dittmar et al., Towards a precise parton luminosity determination at the CERN LHC, Phys.Rev. D56 (1997) 7284

[34] L.Hewett, T.G.Rizzo, Low-energy phenomenology of superstring-inspired E_6 models, Phys.Rep. 183: 193 (1989)

[35] M.Böhm, W.Hollik, Forward-Backward Asymmetries, CERN yellow report 89-08 (09/1989)

[36] Combination procedure for the precise determination of Z boson parameters from results of the LEP experiments, CERN-EP/2000-153 (2000)

[37] M.Dittmar, Neutral current interference in the TeV region: The experimental sensitivity at the CERN LHC, Phys.Rev. D55 (1997) 161

[38] J.L.Rosner, Off-peak lepton asymmetries from new Z' s, Phys.Rev. D35 (1987) 2244

[39] F.del Aguila, M.Cvetič, P.Langacker, Determination of Z' gauge couplings to quarks and leptons at future hadron colliders, Phys.Rev. D48 R696 (1993)

[40] S.Eidelman et al. (Particle Data Group), Phys.Lett. B592, 1 (2004) (URL: http://pdg.lbl.gov)

[41] J.L.Rosner, Prominent Decay Modes of a Leptophobic Z', hep-ph/9607207 (1996)

[42] L.S.Durkin, P.Langacker, Neutral current constraints on heavy Z bosons, Phys.Lett. B166 (1986) 436

[43] K.Hagiwara et al., Review of particle physics, Phys. Rev. D66 (2002) 010001

[44] The LEP Collaborations ALEPH, DELPHI, L3, OPAL, the LEP Electroweak Working Group, the SLD Electroweak and Heavy Flavour Groups, A Combination of Preliminary Electroweak Measurements and Constraints on the Standard Model, hep-ex/0312023 (2003)

[45] T.G.Rizzo, Electroweak Precision Measurements and Collider Probes of the Standard Model with Large Extra Dimensions, Phys.Rev.D61:016007 (2000)

[46] T.G.Rizzo, Phenomenology of higgsless electroweak symmetry breaking, hep-ph/0405094, SLAC-PUB-10431 (2004)

[47] M.E.Peskin, How Can a Heavy Higgs Boson be Consistent with the Precision Electroweak Measurments?, SCLAC-PUB-8763, hep-ph/0101342 (2002)

[48] ATLAS Detector and Physics Performance Technical Design Report, Volume II, CERN/LHCC/99-15 (1999)

[49] PYTHIA, T.Sjöstrand et al., Comp.Phys.Comm. 135 (2001) 238

[50] ATHENA, http://www.wlap.org/atlas/computing/tutorials/athena/2002/

[51] ROOT, René Brun and Fons Rademakers, ROOT - An Object Oriented Data Analysis Framework, Proceedings AIHENP'96 Workshop, Lausanne, Sep. 1996, Nucl. Inst. & Meth. in Phys. Res. A389 (1997) 81-86, http://rootcern.ch/

[52] Olivier Gaumer, PhD thesis LAPP Annecy, in preparation

[53] ATLAS DC1 Project Report (2001)

[54] Géant - R.Brun, F.Carminati, GEANT Detector Description and Simulation Tool, W5013, CERN Programm Library, CERN, Geneva, Switzerland, A Simulation Toolkit, Nuclear Instruments and Methods A506 (2003) 250-303

[55] Electronidentification http://atlas.web.cern.ch/Atlas/GROUPS/LIQARGSOFF/Electron_Photon/eid.html

[56] B.Mellado, S.Paganis, W.Quayle, Sau Lan Wu, ATLAS Electromagnetic Calorimeter calibration and shower isolation studies with an application to the $H \to ZZ^{(\star)} \to 4e$ analysis, ATLAS internal note, ATL-PHYS-2004-005 (2004)

[57] M.C.Cousinou, Search for a W' in the $l\nu$ channel, ATL-Phys-94-059 (1994)

[58] F.del Aguila, M.Cvetič, P.Langacker, Reconstruction of the Extended Gauge Structure from Z' Observables at Future Colliders, hep-ph/9501390v1 (1995)

[59] A.Mück, A.Pilftsis, R.Rückl, An Introduction to 5-Dimensional Extensions of the Standard Model, Lectures given by R.Rückl at the International School "Heavy Quark Physics", May 27-June 5, 2002, JINR, Dubna, Russia, hep-ph/0209371v2 (2002)

[60] H.Georgi, A.K.Grant, G.Hailu, Chiral fermions, orbifolds, scalars and fat branes, Phys.Rev. D63 (2001) 064027